CZECH TECHNICAL UNIVERSITY IN PRAGUE

Faculty of Civil Engineering

Department of Mechanics

Numerical Modelling of Moisture Transport in Concrete under High Temperatures

Implementation of a Multiphase Model, Calibration on X-Ray CT Data and Quantification of Uncertainty

DOCTORAL THESIS

Dipl.-Ing. Christoph Pohl

Doctoral study programme: Civil Engineering

Branch of study: Physical and Material Engineering

Doctoral thesis tutor: Doc. Ing. Vít Šmilauer, Ph.D., DSc.
Doctoral thesis co-tutor: Dr.-Ing. Jörg F. Unger

Prague, 2022

Declaration

Ph.D. student's name: Dipl.-Ing. Christoph Pohl

Title of the doctoral thesis: Numerical Modelling of Moisture Transport in Concrete under High Temperatures

I hereby declare that this doctoral thesis is my own work and effort written under the guidance of the tutor Doc. Ing. Vít Šmilauer, Ph.D., DSc. and co-tutor Dr.-Ing. Jörg F. Unger. All sources and other materials used have been quoted in the list of references.

In Prague on _____ _____
signature

https://doi.org/10.14311/dis.fsv.2022.002

Abstrakt

Transport vlhkosti uvnitř betonu při zvýšených teplotách je klíčovým faktorem pro pochopení rizika odstřelování betonu (spalling). Třífázový model (pevná fáze, suchý vzduch, voda) řeší bilanční rovnice pro pevnou fázi, suchý vzduch, vodní páru, kapalnou vodu a entalpii pomocí metody konečných prvků. Model byl napsán v prostředí FEniCS a řeší dříve opomíjenou bilanci hmotnosti skeletu zavedením pórovitosti jako další nezávislé proměnné. Kromě splnění hmotnostní bilance to umožňuje řešit o jednu konstitutivní rovnici méně a snadnější validaci.

Model byl experimentálně ověřen daty z 3D rentgenové počítačové tomografie (CT). Byla provedena kvantifikace nejistoty pro informovanější rozhodnutí o věrohodnosti modelu. Byly identifikovány odchylky ve vstupních parametrech, prostor parametrů byl nasamplován pomocí metody LHS a určeny výsledné variace na výstupu.

Numerický vícefázový model umožňuje predikci obsahu vody a tlaků uvnitř pórů. Řešení bilance hmotnosti skeletu vede k realističtějším hodnotám než vykazovaly předchozí modely. Model ukázal, že popis dehydratace založené pouze na termogravimetrické analýze nemůže vysvětlit pozorovanou změnu vlhkosti v datech CT. Kvantifikace nejistoty ukazuje variační součinitel mezi 12 % a 16 % pro maximální tlak plynu a jeho pozici, jako důležité indikátory pro vznik odstřelování betonu. Maximální tlak plynu dosahuje přibližně 7,5 MPa a vyskytuje se 50 mm až 100 mm od exponovaného povrchu. Takové zjištění je v souladu s experimenty odstřelování betonu.

Abstract

Understanding the moisture transport inside concrete at elevated temperatures is key to understanding spalling risks. The three-phase finite element model (solid mass, dry air, water) solves the balance equations for solid phase, dry air, water vapour, liquid water and enthalpy. The model was written in FEniCS and solves the previously neglected skeleton mass balance by introducing the porosity as an additional independent variable. In addition to fulfilling the mass balance, this allows for one fewer constitutive equation, so that existing data can be used for validation.

The model was experimentally validated with volumetric X-ray computer tomography data. An uncertainty quantification was performed for more informed decisions on the trust placed in the model. Variation in the input parameters were identified, the parameter space was sampled using Latin hypercube sampling and the resulting variation in the output variables determined.

A numerical multiphase model allows the prediction of water content and pressures inside the pores. Solving the skeleton mass balance results in more realistic values for the skeleton mass density than previous models have exhibited. The model has shown that dehydration descriptions based on thermogravimetric analysis can not explain the moisture change seen in the CT data. The uncertainty quantification reveals a coefficient of variation of about 12 % to 16 % for the maximum gas pressure and its location, chosen as indicators for when and where spalling may occur. The maximum gas pressure attains approximately 7.5 MPa and occurs 50 mm to 100 mm from the exposed surface. Such finding is consistent with spalling experiments.

To Ajax

Acknowledgements

First and foremost, I would like to thank my supervisors for their support and their patience throughout this journey: Vít Šmilauer for sharing his wealth of knowledge and unbridled enthusiasm for anything concrete, as well as the tremendous help he has provided countless times. Jörg F. Unger for his continued guidance through the scientific landscape, his seemingly inexhaustible supply of new ideas and most importantly, his personal support.

I would also like to thank all my colleagues at BAM over the years, for the fruitful discussions (scientific or otherwise), office companionship and plain fun at trips and conferences. Furthermore, I would like to thank Dr. Weise and Ludwig Stelzner from department 7.1. for access to their experimental results. To everyone at the Department of Mechanics at CTU Prague, thank you for the kindness and curiosity you have shown, thereby making my stays in Prague memorable and enjoyable.

Life outside of my research has been a vital source of strength and motivation. For me, a big part of that is basketball, where I would like to thank everyone at DBC Berlin for all the good times and joyful games. Even more important though are all my friends, including, but not limited to, Andreas, Axel, Felix, Jenny, Jonas, Kai, Marcus, Martin, Nehle, Nina, Sandy, Theo, Thimo and Thomas. Thank you for all the conversations, parties, trips and overall fun I had, as well as the occasional shoulder to cry on. I can't express how much this means to me. Thank you, truly.

Last but certainly not least I would like to thank my grandparents and my sister for all the love and support, not just throughout this doctorate, but for as long as I can remember. Most importantly I want to thank my mum for always being there for me, no matter what. I would not be where I am, and who I am, without you. Thank you so much. I love you.

Contents

List of Figures

List of Tables

1. Introduction

Concrete is the most widely used building material in the world. The production of cement, a key ingredient in concrete, accounts for about 8 % of the global amount of CO_2 released into the atmosphere [SCL+15]. Efficient construction and a long service life of the resulting concrete structures is therefore a growing concern. The safety and longevity of a structure is determined by mechanical loads and environmental influences like freeze and thaw cycles, humidity and temperature fluctuations, or aggressive chemicals.

The Great Belt Tunnel fire in 1994, the Channel Tunnel fires in 1996 and 2008, and in particular the disaster in Kaprun in November 2000, have emphasized the need for fire resistant structures. Damage from such incidents cause, in addition to injury and the loss of human live, very costly repairs and service outages. Assessment of the remaining service life after such fires is difficult [KNK21].

Concrete under high temperatures is susceptible to spalling, the explosive breaking off of an outer layer of the structure. This leads to a reduced load-bearing capacity, especially if the reinforcement becomes exposed [YJA17], as both Young's modulus and tensile strength of reinforcing steel at 1200 K are only about five to eight percent of their values at room temperature [CEN04]. High-performance concretes are especially vulnerable to this phenomenon. Understanding and predicting the onset of spalling will increase service-life, help mitigate the consequences and inform repairs on the affected structures.

In a 2015 paper, Gales *et al.* give an overview over the research needs with regards to the fire performance of concrete, and indicate spalling to be the most striking gap in our understanding [GPCG15]:

> The most obvious knowledge gap concerns heat induced concrete spalling. The spalling of concrete cover can expose vital structural reinforcement. […] Even in conventional concrete it is not fully understood. […] In the immediate future, a suitable assessment technique should be developed and used to assess all concrete mixes […] for this risk.

In a literature review, Malhotra identified several hypotheses being offered as the cause for spalling by seven different research groups [Mal84]. The hypotheses can be divided into two main groups, with several modifications proposed for each. The first group are the thermo-mechanical causes: a compressive load due to the restrained thermal expansion and thermal stresses due to the different expansion coefficients of matrix and aggregates combine to induce damage in the material. The second group are the thermo-hygro-mechanical causes, where the presence of pore water causes peaks in pore pressure, in turn leading to tensile stresses. The development of a *moisture clog* is assumed to hinder water transport and therefore to compound the problem.

Numerous numerical models have been proposed that reproduce the thermal and hygral transport processes and try to predict the moisture clog. In the seventies, work by Bažant

Figure 1.1.: Spalling damage to a concrete block after fire exposure. Image from experiments performed at the Federal Institute for Materials Research and Testing in Berlin.

et al. modeled the moisture transport as a single-phase [BN72; BT78]. These early models would form the basis for many later developments, such as the model by Ichikawa and England who extended it to include the mechanical effects of the arising pore pressure on the solid matrix [IE04]. Such single-phase models have been mostly abandoned, as they are unable to distinguish the state of the pore water and do not explicitly consider phase changes (vaporization/condensation).

Multi-phase models emerge in the nineties with the renewed interest in spalling due to the aforementioned fires. A particularly notable group around Gawin, Pesavento and Schrefler has published many papers on the subject [BMS95; GBS96; LS98; GMS99; GPS02; GPS03; GPS04; LLS06; GPS06; GPS11a; GPS11b; GP11; PSS16]. Starting of with an already quite extensive model for the hygro-thermal behaviour of concrete [GBS96; GMS99], additional phenomena such as the critical point transition of water [GPS02], chemical degradation [GPS03; LLS06] and early age hydration [GPS06] were studied over the years. Together with their coworkers, they have also published multiple reviews [GPS11a; GPS11b; GP11; PSS16].

Another series of models is based on the work by Tenchev *et al.* and takes a simpler engineering approach to the problem [TLP01; TLPK01; TP05]. It was later extended by a group around Davie, Pearce and Bićanić, in particular to include the effects of capillary pressure and bound water diffusion [DPB06] and mechanical damage [DPB10; Kuk10; ZD13; DPB14].

One of the major shortcomings of all of the above mentioned models is that they are validated solely on pore pressure and temperature data. In this work, a new model will be validated on X-ray computer tomography data recorded during the heating of a cylindrical specimen to obtain volumetric information about the moisture distribution [PSO+18]. As a result, conventionally used dehydration descriptions were found to exhibit large discrepancies, a finding also observed by Dauti *et al.* [DDW+18; DTD+18].

A further aspect that has not been studied in depth is the solid mass balance, which has been neglected in previous models. The new model is extended to solve this additional balance equation, and the implications of this change are discussed in chapter 5. All the numerical work is done in a custom written code using the finite element framework FEniCS [ABH+15]. The formulation of the model and its main findings were published as a paper in the journal *Materials* [PŠU21].

Lastly, the increasing complexity of these models, the multitude of input parameters, the highly nonlinear behaviour of concrete at high temperatures and plain measurement errors demand a look at the confidence which we place in these models. To that end, an uncertainty quantification is undertaken in chapter 6.

There are still many aspects around the numerical simulation of spalling that will not be explored in this work. The most glaring omission is the coupling to a mechanical damage model. While the results from this model differ from previous results, in particular the moisture content inside the drying front, the differences in pore pressure inside the moisture clog is comparatively small. The principal mechanism for the hygral-mechanical coupling is therefore unaffected, and qualitative insights from models that include damage should apply analogously.

The numerical performance of the employed algorithms is not studied in detail. The choice of linear solver, algorithm for the nonlinear iteration, and time integration scheme were chosen by practical considerations, such as availability and ease of use. The numerical performance, in particular stability and convergence rates, for this coupled problem are discussed only briefly.

Just as the above mentioned models, the approach is purely macroscopic. Mesoscopic modelling might lead to further insight in the future, but currently lacks experimental data for proper validation. Simulation of the behaviour of water inside single pores will be briefly discussed in chapter 3, but a direct coupling of such molecular dynamics simulations to macroscopic FEM computations has not yet been realized.

The thesis is structured as follows: the second chapter will introduce the mechanisms of fluid transport inside the pore space of concrete and additional phenomena that occur at high temperatures. The experimental data that forms the basis for the constitutive laws of the model will be investigated. In chapter 3, the behaviour of water and air inside the pores will be briefly described, and the properties of the fluids enumerated. Chapter 4 will give an introduction to the underlying theory of the numerical model, present a review of the relevant literature and state all relevant balance and constitutive equations in detail. Practical considerations such as boundary conditions, choice of independent variables and numerical approximation of the weak forms will be discussed. Chapter 5 will present the results of the validation simulations, discuss the implications of a) the additional balance equation and b) the choice of dehydration description, as well as the application to a well-known benchmark problem. The uncertainty quantification is treated in chapter 6, where sampling algorithm, experimental variation of constitutive parameters and the resulting uncertainty are delineated. Lastly, the whole thesis is intended to be reproducible, that is all the necessary code and data are openly available, and the whole document can be automatically reproduced. Details can be found in chapter 7.

Objectives

The thesis aims to address the following objectives:

- formulate and implement a coupled thermo-hygral transport model for porous media,
- validate the model on X-ray computer tomography data,
- comparison to existing models, both in terms of performance and complexity,
- identify variability of concrete material parameters and compute sensitivity of the model to these parameters,
- quantify the uncertainty of output properties that are of interest for spalling predictions,
- allow automated replication of the simulations, plots and thesis document.

2. Fluid transport in heated concrete

The flow of liquid water and air through the pore space of concrete is a complex phenomenon. There are several coupled processes occurring, even more so at higher temperatures. This chapter will give an overview of these processes and their interactions. Experimental data is examined to inform on their relative magnitude, the variability between different concrete mixes, the influence of mix parameters such as w/c ratio on the behaviour of the material and the measurement uncertainty of the methods used to obtain the data.

2.1. Pore space of concrete

Before discussing the individual processes, a closer look at the space in which these occur is warranted. The pores in concrete are not of homogeneous size and shape. Table 2.1 shows a common classification of concrete pores, including their size, state of the water in such a pore and a corresponding relative humidity at which the pore became empty during desorption. When water enters the pores from a dry state, the smallest pores (and the walls of the larger pores) are filled first. In this way, a correspondence between the current relative humidity and the size of the pores that are just full of water is made. Additional information on the amount of water taken in as the relative humidity is increased are given by the sorption isotherms, discussed in section 2.4.

Table 2.1.: Pore sizes in concrete according to Thomas and Jennings [TJ08].

Type of pore		Size	Water	Corresp. RH
Capillary pores	large	50 nm–10 µm	evaporable; bulk water	—
	medium	10 nm to 50 nm	evaporable; moderate menisci	above 50 %
Gel pores	small	2.5 nm to 10 nm	evaporable; strong menisci	35 % to 50 %
	micropores	0.5 nm to 2.5 nm	non-evaporable; no menisci	11 % to 35 %
Interlayer spaces		< 0.5 nm	non-evaporable	below 11 %

Table 2.2.: Permeability k of different concretes at room temperature [MPCB13; SH89]

mix	k [10^{-16}m^2]	$k_{\min}, k_{\max}$ [10^{-16}m^2]
B25-2	35.0	[20, 50]
B25-4	100.0	[80, 120]
B25-6	110.0	[100, 120]
B35-1	5.0	[0.1, 10]
B35-3	20.0	[10, 30]
B35-5	15.0	[5, 30]
B35-7	0.5	[0.01, 5]
B40	5.5	
B40SC	3.0	
B40F2	2.5	
B60	1.7	
B60F2	1.6	

2.2. Advection

The advective flow is described by Darcy's law,

$$n(1 - S_w)\mathbf{v}_g = -\frac{kk_{\mathrm{rg}}}{\mu_g}\nabla p_g, \tag{2.1}$$

$$nS_w\mathbf{v}_w = -\frac{kk_{\mathrm{rw}}}{\mu_w}\nabla p_w, \tag{2.2}$$

where kk_{rg} and kk_{rw} are the gas and water permeability, respectively.

The gas permeability of concrete is commonly measured by the *Cembureau method* [Kol89], where a disk is placed into a sealed cell, pressurized gas is applied and the flow rate is measured. The permeability can than be computed from the flow rate and the difference in in- and outlet pressure.

Mindeguia *et al.* [MPCB13] have performed this test for five different concretes: an ordinary concrete B40, a compact variant B60, both with added fibres (B40F2 and B60F2), and the ordinary concrete with silico-calcareous aggregates B40SC. A study by Schneider and Herbst [SH89] compared seven different concretes: three mixes (B25-2, B25-4, B25-6) with high w/c ratios (0.7, 0.75 and 0.75, respectively) and four mixes (B35-1, B35-3, B35-5, B35-7) with low w/c ratios (0.5, 0.5, 0.5 and 0.45, respectively), with different aggregate types differentiating the mixes. In addition, the bounds of variation were given in [SH89]. The results can be found in table 2.2.

Two observations are clear: the denser concretes with lower w/c ratios also have lower permeabilities, and there is a significant variation even within one concrete mix, especially for concretes with low permeabilities.

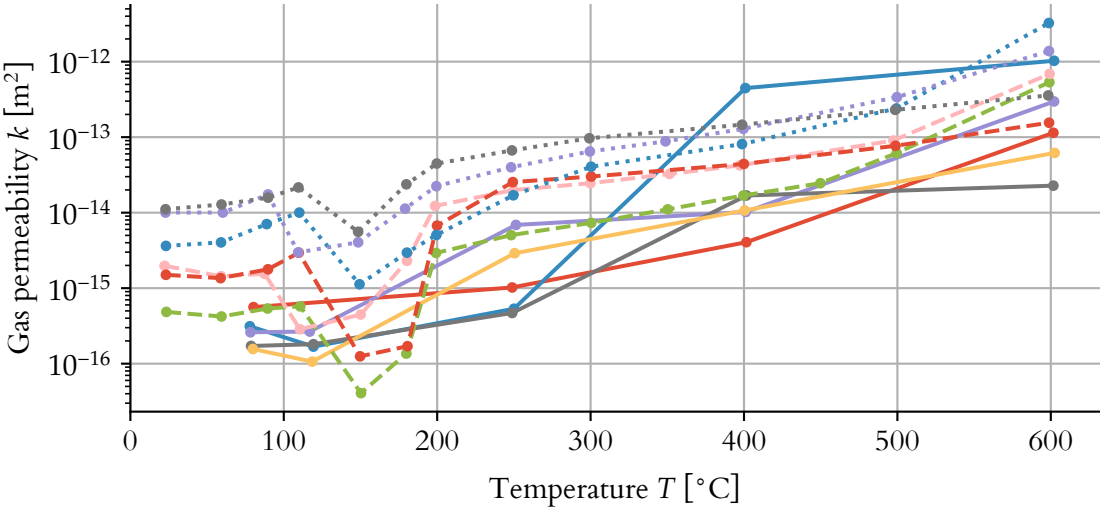

Figure 2.1.: Gas permeabilities of different concretes after being heated to different temperatures. The solid lines correspond to the data from [MPCB13] (fluid: dinitrogen), dashed lines to the high strength samples from [SH89] (fluid: compressed air), and dotted lines to the low strength samples from the same paper.

Unfortunately, this experiment can only be conducted at room temperature. To gain an understanding how the advective flow is effected by higher temperatures, the specimen are often heated to a certain temperature, allowed to cool down again and then measured again as an approximation to the high temperature behaviour.

The evolution of the concretes tested in [SH89; MPCB13] can be seen in fig. 2.1. Without going into details about the influence of w/c ratio, aggregate types and added fibres, a couple of things can be noted. There is a slight dip in permeability between 100 °C and 200 °C, where the evaporation of water hinders the air flow through the specimen. The difference in permeability between concretes can be orders of magnitude. Within the same concrete mix, the difference between initial permeability and permeability after being heated to high temperatures is also orders of magnitude.

Another way of looking at this evolution, rather than as a function of temperature, is using porosity measurements discussed in section 2.6 as the independent variable. The data from [SH89] is shown in fig. 4.3. This relation is physically more intuitive—an enlarged pore space allows for an increased fluid flow.

The relative permeabilities k_{rg} and k_{rw} express the change permeability for different saturations. For a saturation of zero, i.e. no free water, the water permeability goes to zero as well. Conversely, for a saturation of one, where the pores are completely filled with liquid water, the gas permeability goes to zero. Although several relationships between the saturation and the relative permeabilites are proposed, no experimental evidence was given for these models. They are discussed in section 4.4.1.

The permeability is supposed to be an intrinsic material parameter of the solid, independent of the fluid. Even when accounting for differences in density and viscosity as is done by

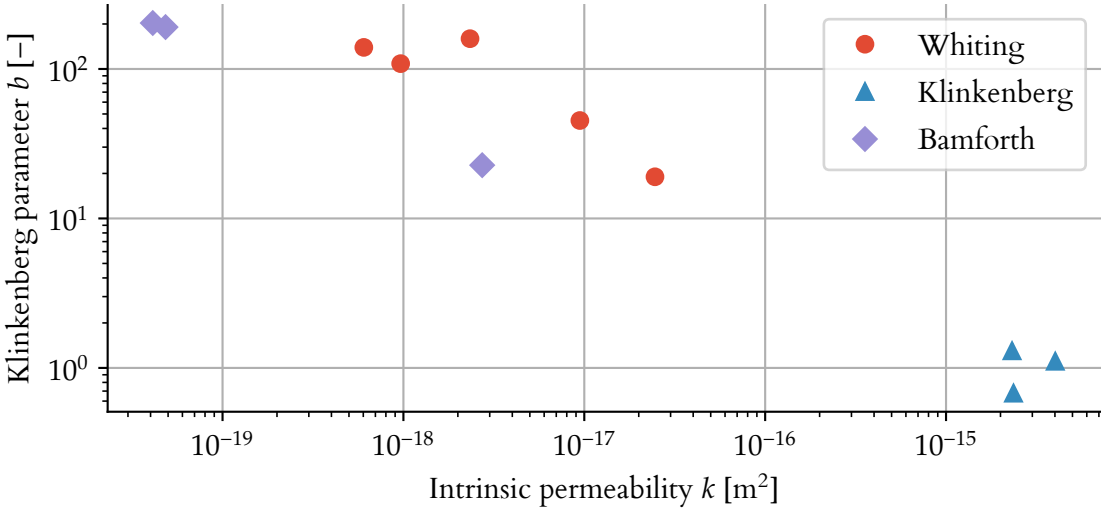

Figure 2.2.: Varation of the Klinkenberg constant b for different intrinsic permeabilities. Data from [Whi88; Kli41; Bam87]. Adapted from [CC05].

Darcy's law, the gas and liquid flow still differs significantly. Darcy's law is an approximation that works well for laminar liquid flow; for gas flow, however, the assumption of zero fluid velocity at the solid surface does not hold. This difference is particularly strong for low permeability, high surface area porous solids, where this slip effect leads to a higher flow rate than predicted. This is often called the *Klinkenberg effect*. To account for this, a slip modification factor

$$\kappa = 1 + b\frac{p_{\text{atm}}}{p_g}, \tag{2.3}$$

is introduced into Darcy's law

$$n(1 - S_w)\mathbf{v}_g = -\kappa\frac{k k_{\text{rg}}}{\mu_g}\nabla p_g. \tag{2.4}$$

The factor b is different for different concretes, with experimental values shown in fig. 2.2. As noted above, the difference becomes more pronounced for concretes with lower permeabilites, such as high performance concretes.

2.3. Diffusion

A diffusive flow is driven by concentration gradients, in this particular case by water vapour concentration in the pores. In addition to this gas flow, the physically bound water is also assumed to diffuse along the surface of the pores.

To obtain the diffusivity of concrete, a sample may be placed as a divider between two chambers, with one containing a water cup and the other containing silica gel. Measuring the change in mass of the water and silica gel after certain time intervals, together with the

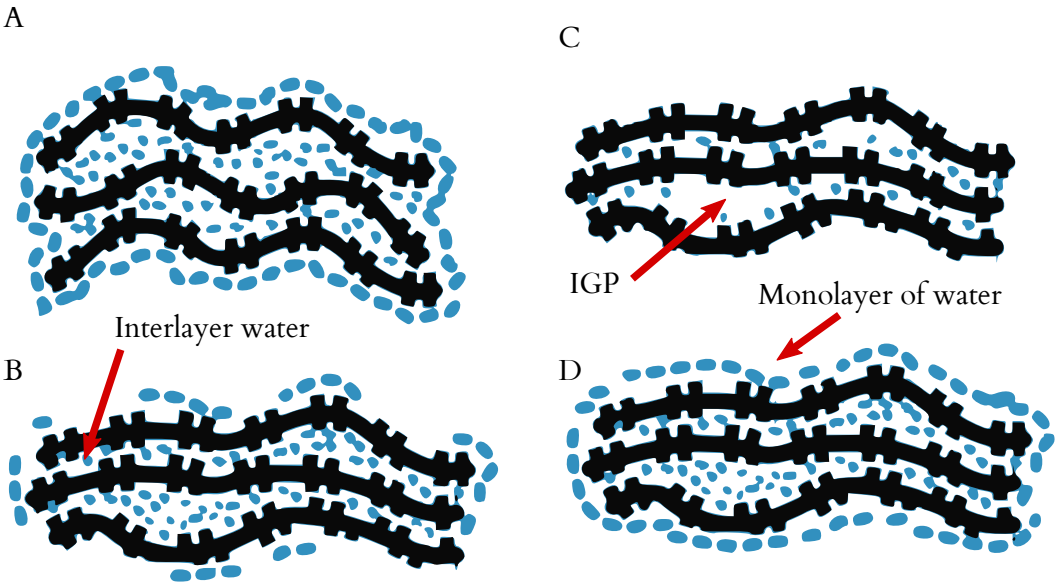

Figure 2.3.: CSH globule with water contents at different stages along the sorption isotherm. Image from [Jeno8].

ideal gas assumption, allows calculating the diffusivity. Vodák *et al.* [VČD+97] conducted this procedure for a high-performance concrete with a w/c ratio of 0.45, giving a value of $D = 4.98(26) \times 10^{-7}\,\mathrm{m^2\,s^{-1}}$.

An additional phenomenon is the diffusion of adsorbed water along the pore walls.

2.4. Sorption

One of the central relations for porous media is the link between the saturation of the wetting phase and the capillary pressure, $S_w = f(p^c)$. Such a function f can be found from the sorption isotherms, that is the relation between relative humidity and water mass content m_w in the pores. The saturation can be determined from the water mass content from

$$S_w = \frac{m_w}{n\rho^w}. \tag{2.5}$$

The capillary pressure corresponding to a relative humidity can be found from the Kelvin equation (see section 3.4),

$$\ln \frac{p_v}{p_{vs}} = -\frac{p_c}{\rho_w}\frac{M_w}{RT}. \tag{2.6}$$

For concrete, or more specifically the C-S-H phase from cement hydration, Jennings used the sorption isotherms to create a model of the microstructure that explains the behaviour of C-S-H below 11 % relative humidity [Jeno8]. The stages (A) through (D) used in the following description can be seen as illustrations of the globule in fig. 2.3 and along the sorption isotherm in fig. 2.4. After the initial drying (A) down to 11 %, the globule is fully

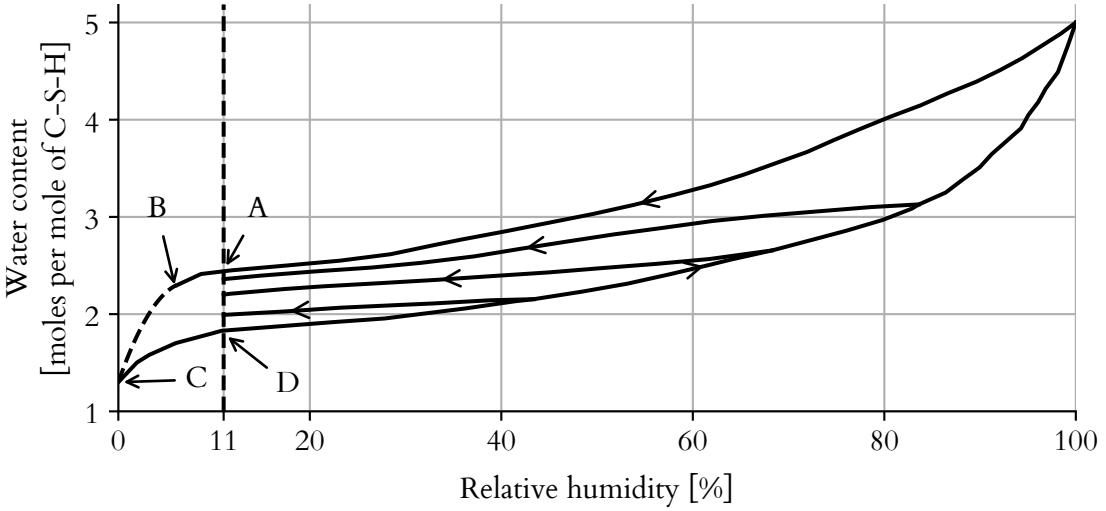

Figure 2.4.: Sorption isotherms for hardened cement paste, with a w/c ratio of 0.5. Based on [Jeno8].

saturated and a monolayer of water has formed on the surface. The interlayer spaces and interglobular pores (IGP) are filled with water. As the drying continues (B), the interlayer and monolayer water decreases. The volume of the globule decreases, resulting in a higher density than the saturated globule. At the completely dried stage (C), all evaporable water is removed. The IGP are empty, and the created voids reduce the density of the globule. During rewetting up to (D), the water returns to the IGP and a water monolayer forms.

The experimental setup for measuring the sorption isotherms is to put the specimen into sealed containers with fixed relative humidities. The humidity in a container is controlled by using different saturated salt solutions for which the relative humidity is known. The mass of the specimens is then determined by weighing.

A study by Baroghel-Bouny *et al.* [BMLC99] used discs of 90 mm diameter and 3 mm thickness. The dry reference state was determined at 3 % relative humidity rather than oven drying at uncontrolled humidity conditions. Four different materials were investigated—two hardened cement pastes, CO and CH, and two concretes, BO and BH. The mixes CO and BO are ordinary materials, while CH and BH correspond to high-performance materials. They have a lower w/c ratio and contain additional silica fumes and superplasticizer.

For hardened cement paste and concrete, considerable hysteresis occurs between sorption and desorption. A typical isotherm including hysteresis is shown for a hardened cement paste in fig. 2.5. Below about 37 %, the difference between the sorption and desorption branches is only a couple of percentage points. Above that, the cement paste can contain almost double the water content on desorption than on adsorption. Multiple causes for the hysteresis have been suggested. One is the forming of a stable meniscus (interface between water vapour and liquid water) during desorption that does not reform during adsorption. Another is the behaviour of interlayer water during adsorption as described in the CM-II model [Jeno8]. Water is prevented from entering the interlayer at low humidities by the structure of the

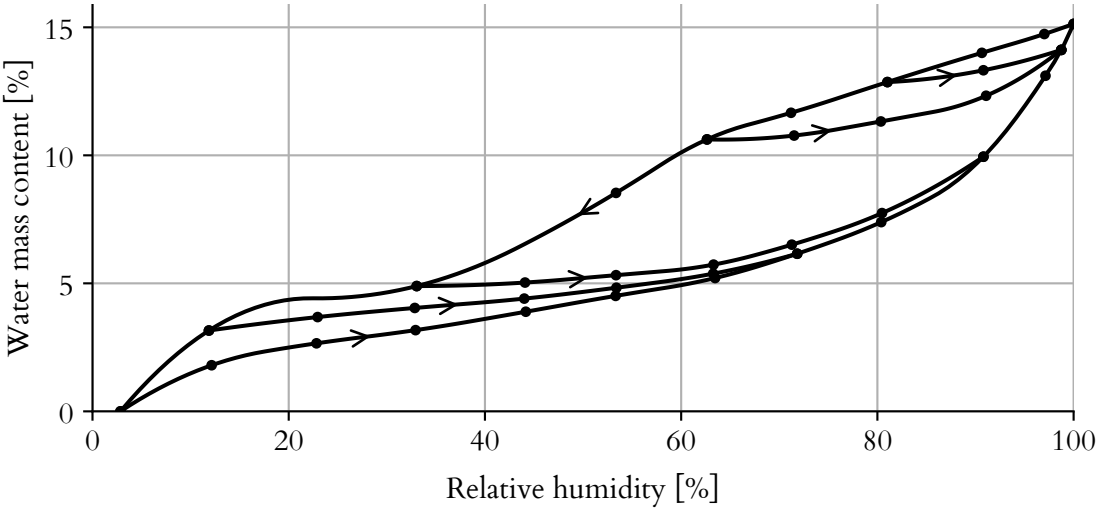

Figure 2.5.: Adsorption and desorption isotherms for a hardened cement paste [BMLC99].

C-S-H globules. After multiple layers of water molecules accumulate on the surface of the globule, the surface energy is reduced and allows the structure to relax. This enables the water to enter the interlayer spaces.

Isotherms for two concretes, one ordinary and one high-performance variant, are shown in fig. 2.6. Compared to the cement paste, the mass content is much lower, since the aggregates adsorb almost no water. Below about 60 %, the two materials exhibit similar behaviour. Above this point, however, the high-performance material shows a much lower water content than the ordinary concrete. This is caused by the very narrow pore network and lower porosity that results from the low w/c ratio and the silica fumes. The variation between sorption/desorption cycles in the range 50 % to 90 % is also much lower.

When looking at the ratio of water mass to the mass of the hardened paste in each mix, the water content below 44 % RH is not influenced by the mix (see fig. 2.7). This shows that the moisture equilibrium in this range takes place in a pore structure that is not influenced by the mix. According to the authors, this corresponds to pore radii of $r_p \leqslant 20$ Å.

2.5. Dehydration

During heating of concrete, chemical reactions change the composition of the hardened cement paste; typical aggregate types are much more chemically stable. These chemical reactions grouped under the term dehydration, since they release chemically bound water from the cement matrix into the pore system. The reactions also lead to an adsorption of latent heat, a change in porosity of the bulk material and a release of chemically bound water into the pore system. Typically they depend on the rate of heating, yet for practical purposes this is often neglected [ZW73]. Describing the evolution only as a function of temperature obtained by experiments performed at typical heating rates means that for very slow or very

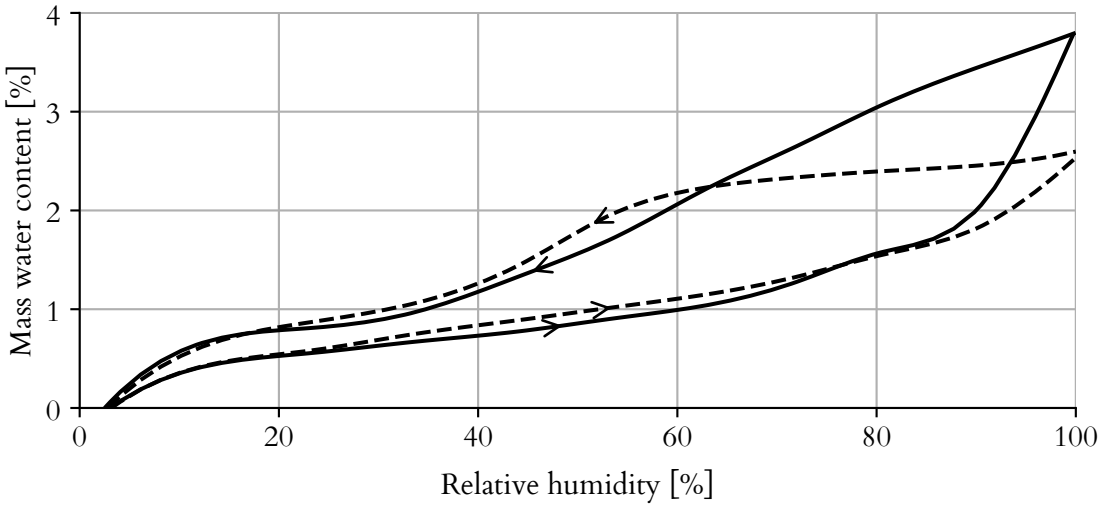

Figure 2.6.: Sorption isotherms for ordinary (solid line) and high-performance concrete (dashed line) [BMLC99]. Only adsorption from the completely dry state, and desorption from the fully wet state are shown.

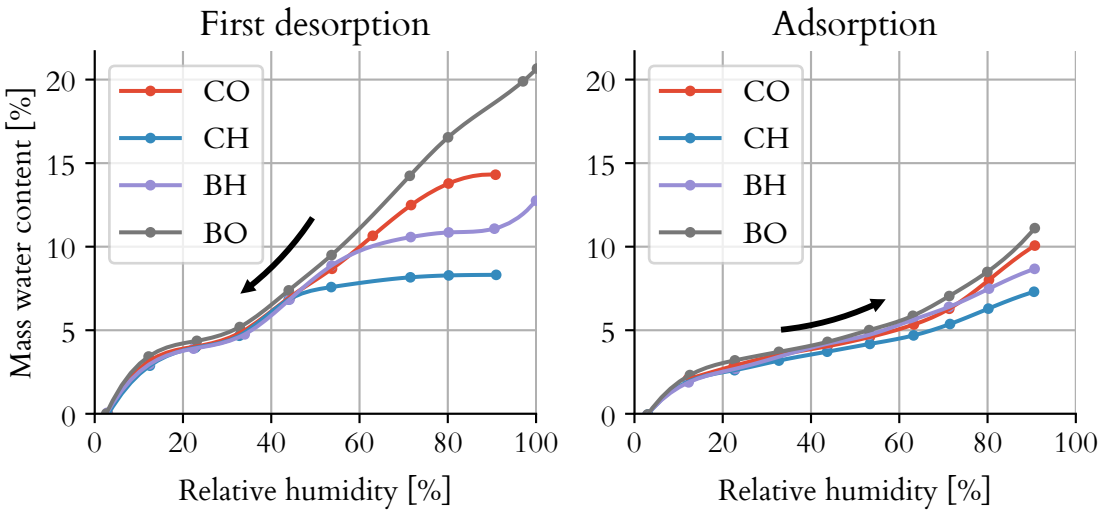

Figure 2.7.: Desorption and adsorption isotherms, with water content relative to mass of hardened cement paste in the mix [BMLC99].

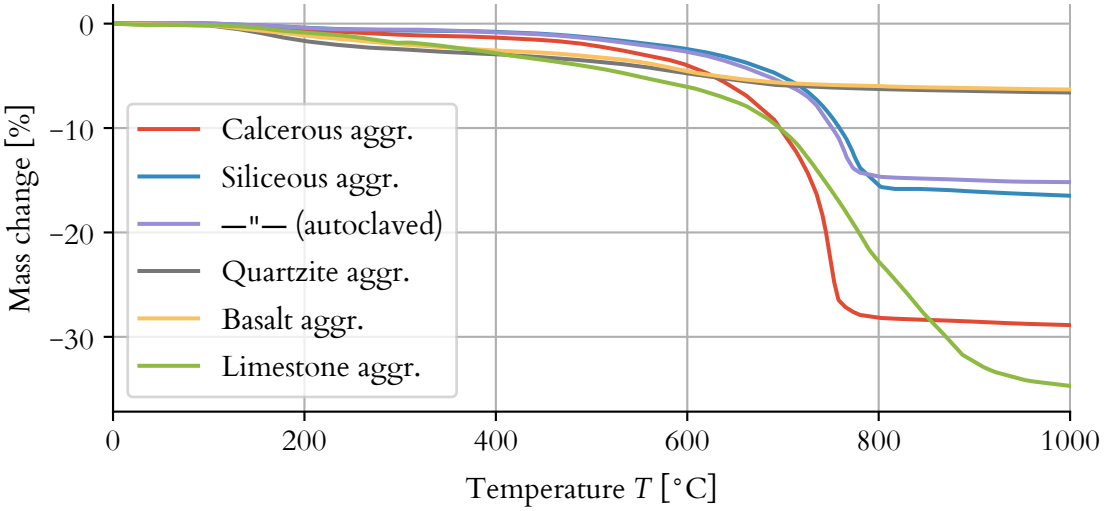

Figure 2.8.: Mass loss during thermogravimetry for different concretes. Data from [ZW73; BK96].

fast heating, considerable errors are possible. The presence of dehydration lowers the spalling risk, since the reaction adsorbs heat resulting in lower temperatures and the reaction causes a rise in porosity and permeability.

The evolution of the water content with rising temperature is commonly measured using thermogravimetric analysis (TGA). Performing the measurement on dry specimen gives the dehydrated water content. Results for different concretes are shown in fig. 2.8. The specimen have been oven-dried at 105 °C before the experiment, resulting in no mass loss during the TGA below that temperature. Up to about 400 °C, the mass change is below 3 % and quite close for all measured concretes. Beyond that, up to about 800 °C, a drastic mass loss can be observed, with maximum values of 28 % for the concrete with calcareous aggregates, about 15 % for the siliceous aggregate based concrete, and about 6.5 % for concretes using basalt and quartzite. Above this temperature the behaviour stabilizes, except for the concrete with limestone aggregates. Autoclaving after presetting results in a small reduction in mass loss.

The dehydration degree can be defined as the ratio of current to maximally possible mass change

$$\Gamma_{\text{dehydr}} = \frac{m(T_0) - m(T)}{m(T_0) - m(T_\infty)}. \tag{2.7}$$

The dehydration degree is a function of the highest temperature reached in the materials history, $\Gamma_{\text{dehydr}}(t) = \Gamma_{\text{dehydr}}(T_{\max}(t))$, and therefore $\dot{\Gamma}_{\text{dehydr}} = 0$ for $T(t) < T_{\max}(t)$. The evolution $\Gamma_{\text{dehydr}}(t)$ can be obtained from the thermogravimetric curves.

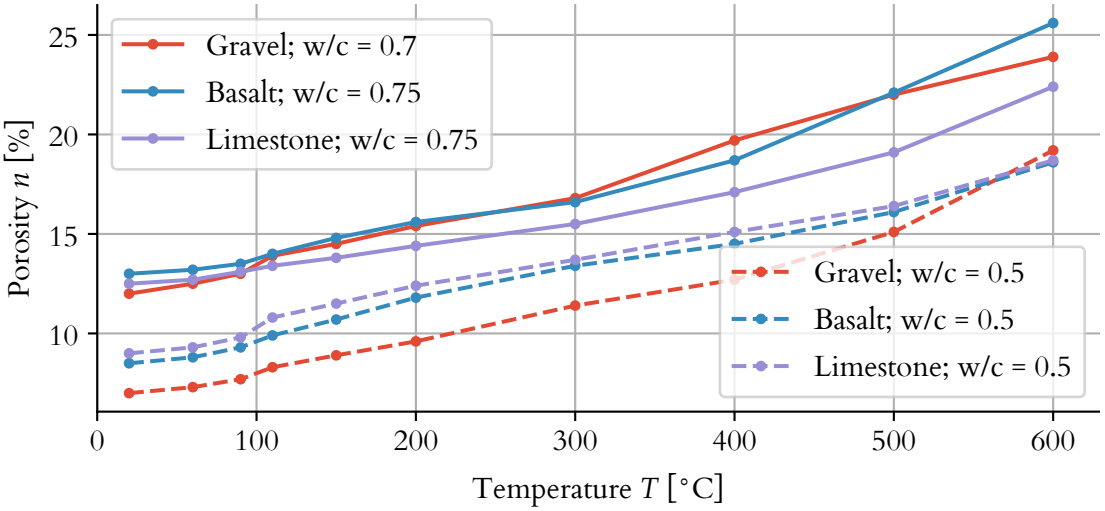

Figure 2.9.: Change in porosity of six different concretes (three different aggregate types at two w/c ratios) with rising temperatures. Solid lines denote mixes with a higher w/c ratio. Data from [SH89].

2.6. Porosity evolution

The porosity is measured using mercury intrusion porosimetry, where mercury is being forced under pressure into the pore space and the achievable volume of mercury in the pores at a given pressure is measured. The ratio of pore volume to total volume gives the porosity. Mercury is assumed to be incompressible in these tests. Intrusion porosimetry can not be performed at high temperatures. Therefore, all temperature dependent values in this sections have been measured at room temperature after heating the specimen to the specified temperature and letting it cool down again.

The results of such measurements for six different concretes, three ordinary and three mixes with a lower w/c ratio, are shown in fig. 2.9. The increase in porosity is almost linear with temperature. Aggregate type has only a minor influence of the porosity evolution. The fact that lower w/c ratios lead to denser cement pastes and lower porosities is clearly visible.

If one makes a further assumption on the shape of the pores as being cylindrical, the Washburn equation describes the relation between pressure and pore radius,

$$r = \frac{2\sigma \cos \vartheta}{p} \tag{2.8}$$

where r is the pore radius, σ is the surface tension (0.48 N m^{-1} for mercury at 20 °C), ϑ is the contact angle (142.3° for hardened cement paste – mercury pairing) and p is the applied pressure. This allows determining the pore size distribution as well.

The evolution of the pore size distribution can be seen in fig. 2.10. At room temperature, the concrete shown here exhibits a distinct peak between 20 nm and 50 nm. Other concretes in the same paper exhibit a similar, albeit wider peak. After heating to 90 °C, the peak is

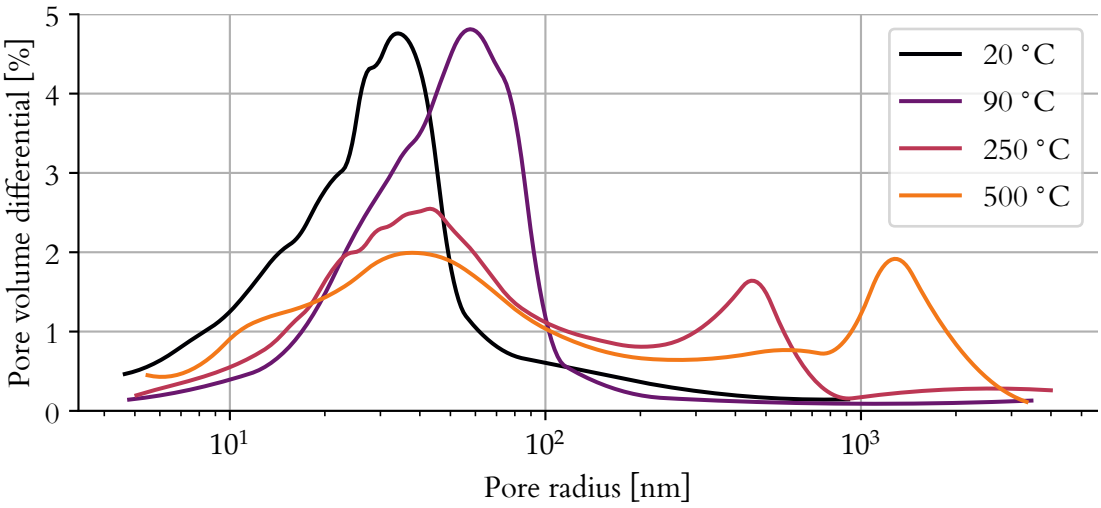

Figure 2.10.: Pore size distribution for a B-35 basalt concrete after heating to four different temperatures. Data from [SH89].

shifted to a range of 40 nm to 90 nm. This is likely due to the drying of the pore system. When increasing the temperature further to 250 °C, a second peak between 380 nm and 420 nm develops. It is believed that this relates to the creation of additional pore space in the form of microcracks, most likely at the matrix-aggregate interfaces. Further heating to 500 °C reinforces this trend, with the second maximum shifting to larger poresizes and the value of the first maximum decreasing. Use of the pore size distribution for the calculation of the diffusivity coefficient was discussed in the previous section.

3. Behaviour of water and air

3.1. Water properties

Water is a widely studied substance, with accurate descriptions of its properties over a wide range of temperatures. These descriptions are published by the International Association for the Properties of Water and Steam (IAPWS).

The representation given here is based on their publication [WP93]. It uses the following parameters at the critical point: pressure $p_{\text{crit}} = 22.064\,\text{MPa}$, density $\rho_{\text{crit}} = 322\,\text{kg}\,\text{m}^{-3}$ and temperature $T_{\text{crit}} = 647.096\,\text{K}$. An auxiliary variable τ is defined, denoting a relative distance to the critical temperature, $\tau = 1 - \frac{T}{T_{\text{crit}}}$.

3.1.1. Density

The liquid phase is assumed to be incompressible (no change in density due to changes in pressure), but the density decreases with temperature according to

$$\frac{\rho_w}{\rho_{\text{crit}}} = 1 + b_1\tau^{\frac{1}{3}} + b_2\tau^{\frac{2}{3}} + b_3\tau^{\frac{5}{3}} + b_4\tau^{\frac{16}{3}} + b_5\tau^{\frac{43}{3}} + b_6\tau^{\frac{110}{3}}, \tag{3.1}$$

with

$$\begin{aligned} b_1 &= 1.992\,740\,64 & b_4 &= -1.755\,493\,479 \\ b_2 &= 1.099\,653\,42 & b_5 &= -45.517\,035\,2 \\ b_3 &= -0.510\,839\,303 & b_6 &= -6.746\,944\,50 \times 10^5. \end{aligned}$$

Another, slightly simpler description is given by Furbish [Fur96] as a polynomial of the temperature in degrees Celsius, T_c,

$$\rho_w = b_0 + b_1 T_c + b_2 T_c^2 + b_3 T_c^3 + b_4 T_c^4 + b_5 T_c^5, \tag{3.2}$$

with

$$\begin{aligned} b_0 &= 1.0213 \times 10^3 & b_3 &= -9.2188 \times 10^{-5} \\ b_1 &= -7.7377 \times 10^{-1} & b_4 &= 3.3534 \times 10^{-7} \\ b_2 &= 8.7696 \times 10^{-3} & b_5 &= -4.4034 \times 10^{-10}. \end{aligned}$$

Both descriptions can be seen in fig. 3.1.

For the vapour state, the density at saturation pressure is given as

$$\ln\left(\frac{\rho_v}{\rho_c}\right) = c_1\tau^{\frac{1}{3}} + c_2\tau^{\frac{2}{3}} + c_3\tau^{\frac{4}{3}} + c_4\tau^3 + c_5\tau^{\frac{37}{6}} + c_6\tau^{\frac{71}{6}} \tag{3.3}$$

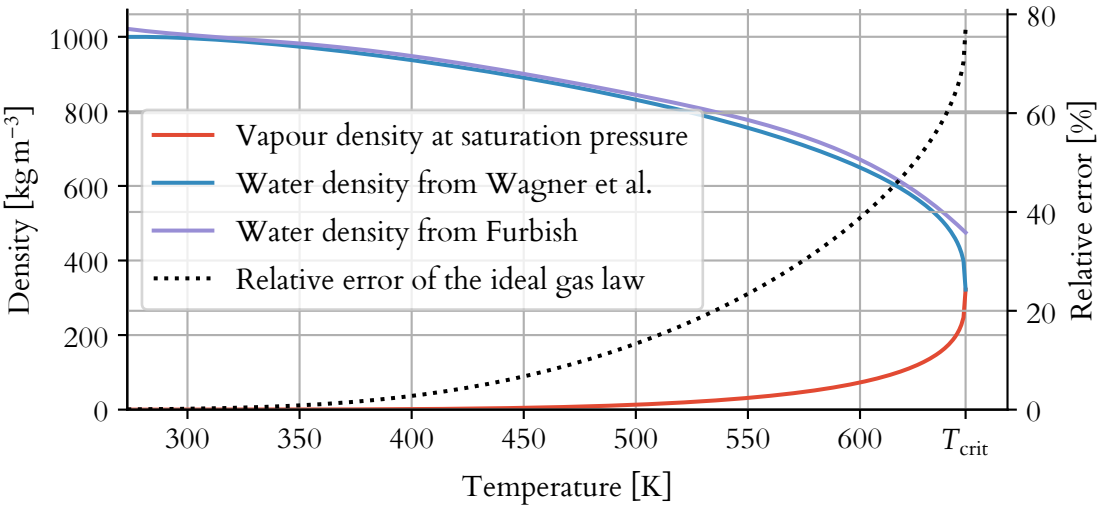

Figure 3.1.: Comparison of the density of liquid water (blue) and saturated vapour (red). Additionally, the relative error of the ideal gas equation at saturation pressure is shown.

with

$$c_1 = -2.031\,502\,40 \qquad c_2 = -2.683\,029\,40$$
$$c_3 = -5.386\,264\,92 \qquad c_4 = -17.299\,160\,5$$
$$c_5 = -44.758\,658\,1 \qquad c_6 = -63.920\,106\,3$$

Below the saturation pressure, vapour density can be computed using the ideal gas equation,

$$\rho_v = p_v \frac{M_w}{RT}. \tag{3.4}$$

The ideal gas equation is only an approximation, and underestimates the density. The closer to the saturation pressure and critical temperature, the larger the approximation error. The change in density at saturation pressure as well as the error of the ideal gas equation are shown in fig. 3.1. Note that the error may be much less severe for pressures below the saturation pressure.

3.1.2. Specific heat capacity

The values for specific heat capacity of both liquid water and water vapour have been tabulated in [Ceno6]. For use in numerical simulation, Davie *et al.* [DPBo6] have proposed the following approximations for the liquid

$$C_p^w = \begin{cases} 3368\,\mathrm{J\,kg^{-1}\,K^{-1}} + 2.4768\,\mathrm{J\,kg^{-1}\,K^{-2}} \cdot T + 1\,\mathrm{J\,kg^{-1}\,K^{-1}} \cdot \left(\frac{aT}{513.15\,\mathrm{K}}\right)^b & \text{for } T \leqslant T_{crit}, \\ 24\,515.0\,\mathrm{J\,kg^{-1}\,K^{-1}} & \text{for } T > T_{crit}, \end{cases} \tag{3.5}$$

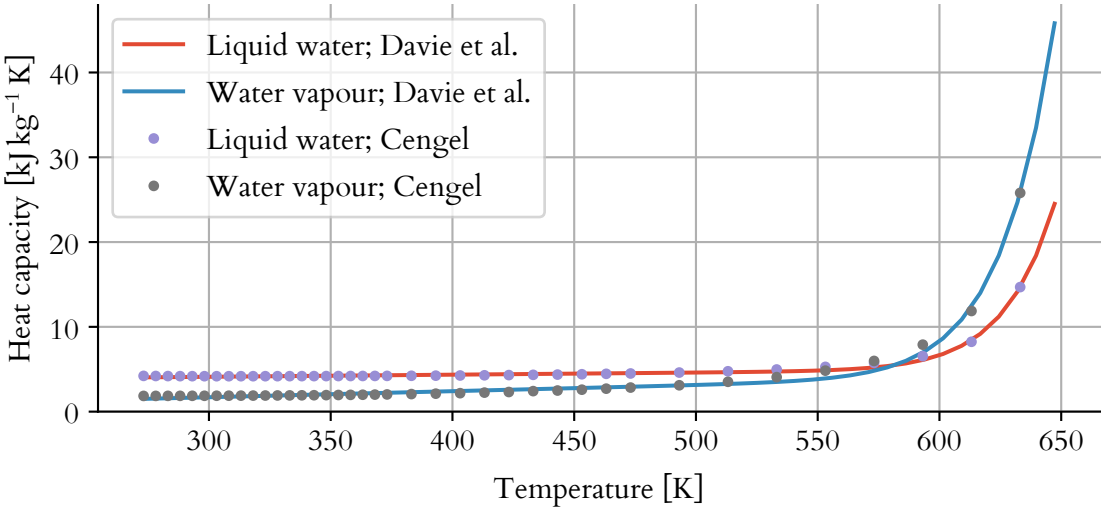

Figure 3.2.: Heat capacity of liquid water and water vapour. The experimental values are taken from [Ceno6], while the continuous approximations are from [DPBo6].

where $a = 1.085\,426\,319\,886\,38$ and $b = 31.444\,765\,761\,663\,6$, and the vapour state

$$C_p^v = \begin{cases} -443.0\,\mathrm{J\,kg^{-1}\,K^{-1}} + 7.1399\,\mathrm{J\,kg^{-1}\,K^{-2}} \cdot T + 1\,\mathrm{J\,kg^{-1}\,K^{-1}} \cdot \left(\frac{aT}{513.15\,\mathrm{K}}\right)^b & \text{for } T \leqslant T_{\mathrm{crit}}, \\ 45\,821.04\,\mathrm{J\,kg^{-1}\,K^{-1}} & \text{for } T > T_{\mathrm{crit}}, \end{cases} \tag{3.6}$$

where $a = 1.137\,715\,022\,281\,62$ and $b = 29.443\,528\,752\,114\,3$. A comparison of the experimental data and the approximations can be seen in fig. 3.2.

3.1.3. Viscosity

The viscosity of water is strongly dependent on the temperature and state of water, and weakly dependent on the pressure. Experimental values are given in [SW86]. A commonly used approximation was given by Thomas and Sansom [TS95], which neglects the pressure influence

$$\mu_w = 0.6612\,\mathrm{Pa\,s} \cdot \left(\frac{T - 229\,\mathrm{K}}{1\,\mathrm{K}}\right)^{-1.562}. \tag{3.7}$$

A comparison of the experimental values and their approximation shows good agreement for temperatures below 100 °C at standard pressures, whereas the change in state is not captured by the approximation. Above 450 °C, the error is again below 5 %. See fig. 3.3.

The viscosity of water vapour is given in [GMS99] as

$$\mu_v = \mu_{\mathrm{vo}} + \alpha_v (T - T_{\mathrm{ref}}), \tag{3.8}$$

with $\mu_{\mathrm{vo}} = 8.85 \times 10^{-6}\,\mathrm{Pa\,s}$ and $\alpha_v = 3.53 \times 10^{-8}\,\mathrm{Pa\,s\,K^{-1}}$.

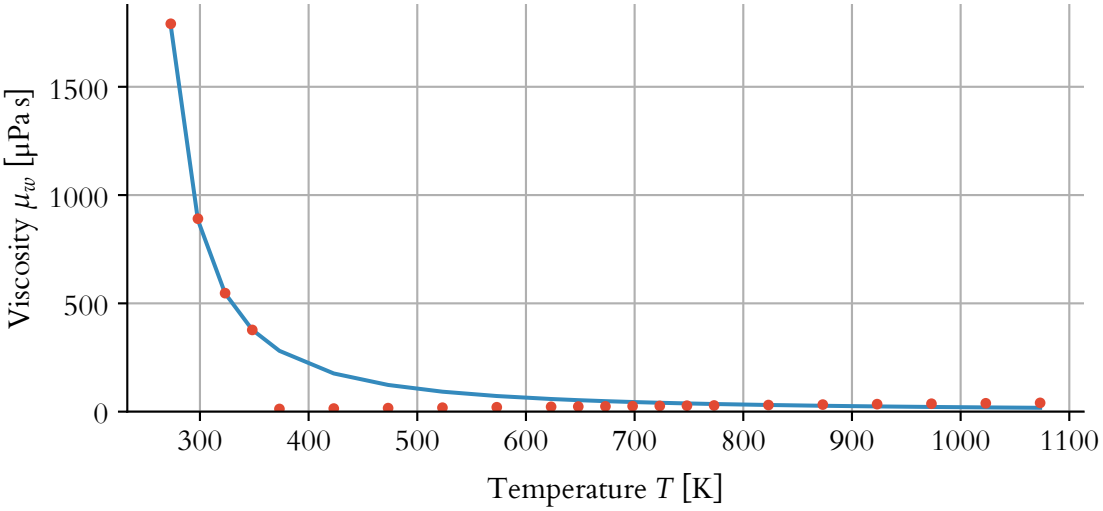

Figure 3.3.: Viscosity of water at standard pressure. The experimental values (dots) from [SW86] show a jump as the water changes from a liquid to a vapour during heating. This is not captured by the approximation (solid line) given in [TS95].

3.1.4. Evaporation enthalpy

The evaporation enthalpy is the amount of energy needed to transfer a substance from a liquid to a gaseous state. With rising temperatures, the evaporation enthalpy decreases and becomes zero at the critical point, for all substances, not only water. The most commonly used formulation is called the Watson formula [Wat43], specified here for water as

$$\Delta h_{\text{vap}} = 2.672 \times 10^5 \,\text{J}\,\text{kg}^{-1} \left(\frac{T_{\text{crit}} - T}{1\,\text{K}} \right)^{0.38}, \tag{3.9}$$

A comparison to the values given in [Ceno6] is shown in fig. 3.4.

3.2. Air properties

3.2.1. Density

The density of dry air can be approximated very well with the ideal gas equation,

$$\rho = p \frac{M_a}{RT}, \tag{3.10}$$

where $M_a = 28.971 \times 10^{-3}\,\text{kg}\,\text{mol}^{-1}$.

3.2.2. Heat capacity

The heat capacity was given in [DPB06] as

$$C_p^a = aT^3 + bT^2 + cT + d, \tag{3.11}$$

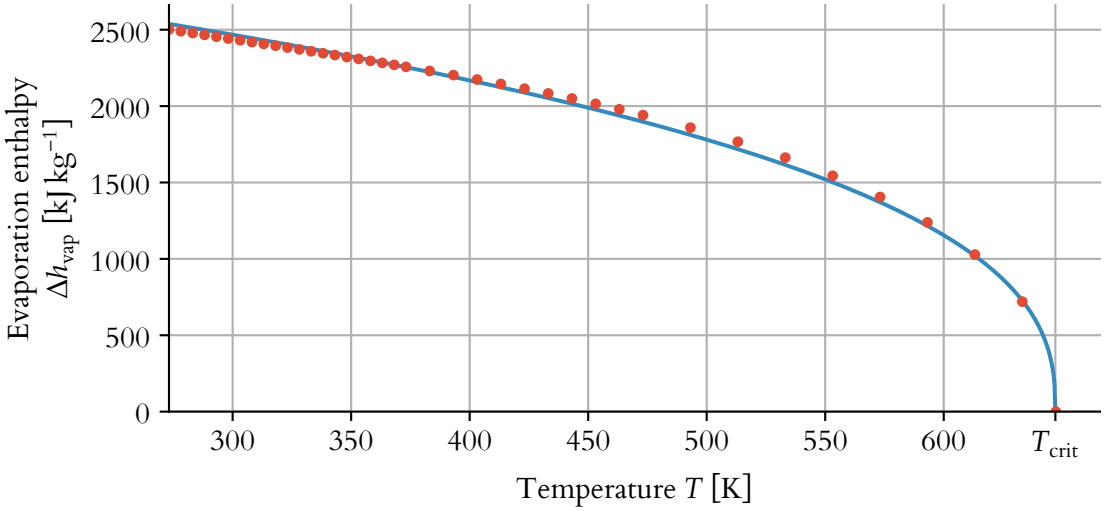

Figure 3.4.: Water evaporation enthalpy; experimental values (dots) and approximation by Watson formula (solid line).

where $a = -9.849\,367\,018\,147\,35 \times 10^{-8}\,\mathrm{J\,kg^{-1}\,K^{-4}}$, $b = 3.564\,362\,577\,698\,61 \times 10^{-4}\,\mathrm{J\,kg^{-1}\,K^{-3}}$, $c = -1.216\,179\,239\,877\,57 \times 10^{-1}\,\mathrm{J\,kg^{-1}\,K^{-2}}$ and $d = 1.012\,502\,552\,163\,24 \times 10^{3}\,\mathrm{J\,kg^{-1}\,K^{-1}}$. A comparison with experimental data from [Ceno6] can be seen in fig. 3.5.

3.2.3. Viscosity

The viscosity of dry air is given in [GMS99] as

$$\mu_a = \mu_a^0 + \alpha_a(T - T_0) - \beta_a(T - T_0)^2, \tag{3.12}$$

where $\mu_a^0 = 17.17\,\mu\mathrm{Pa\,s}$, $\alpha_a = 4.73 \times 10^{-2}\,\mu\mathrm{Pa\,s\,K^{-1}}$, $\beta_a = 2.22 \times 10^{-5}\,\mu\mathrm{Pa\,s\,K^{-2}}$ and $T_0 = 273.15\,\mathrm{K}$. A comparison with experimental data from [Ceno6] can be seen in fig. 3.6.

3.3. Water in nanoconfinement

Water molecules in very small spaces, where the number of molecules across a dimension may only be in the low double digits, can behave very differently from bulk water. Gel pores in concrete, which make up a significant portion of the pore space, are between 0.5 nm to 10 nm in size (see section 2.1). The mean van der Waals diameter of water is 2.8 Å, meaning that only between two and 35 layers of water molecules may fit into these pores. A brief overview of the behaviour of water in nanoconfinement seems expedient.

The two main concerns here are the distribution of water within the pore, which is related to adsorption (see section 2.4), and the change in diffusivity (see section 2.3). In a molecular dynamics study from Hartnig *et al.*, a pore of 40 Å inside a SiO_2 cell was filled with different numbers of water molecules, amounting to two different hydration levels [HWS+00]. As can

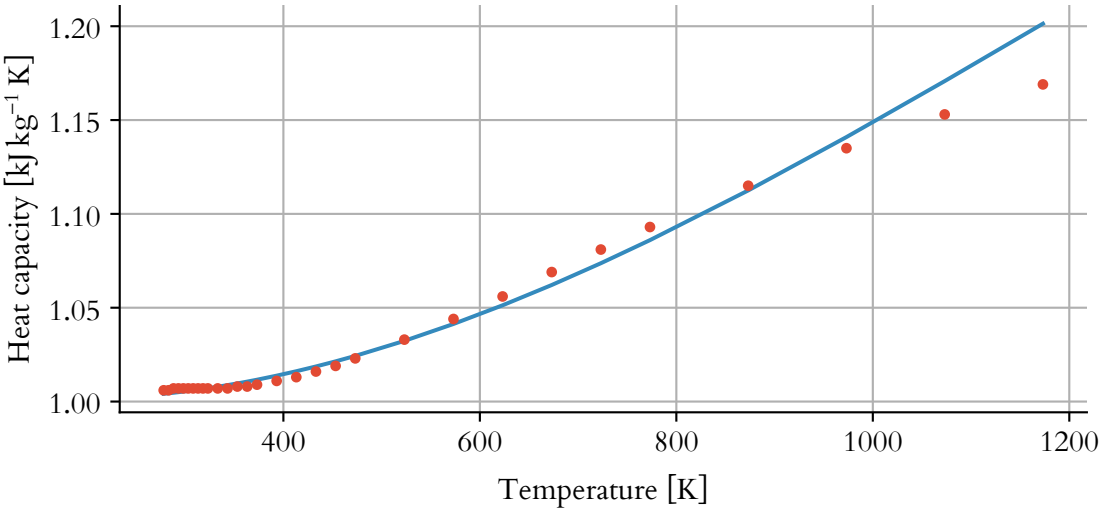

Figure 3.5.: Heat capacity of dry air; experimental values [Ceno6] (dots) and approximation by Davie *et al.* [DPBo6] (solid line).

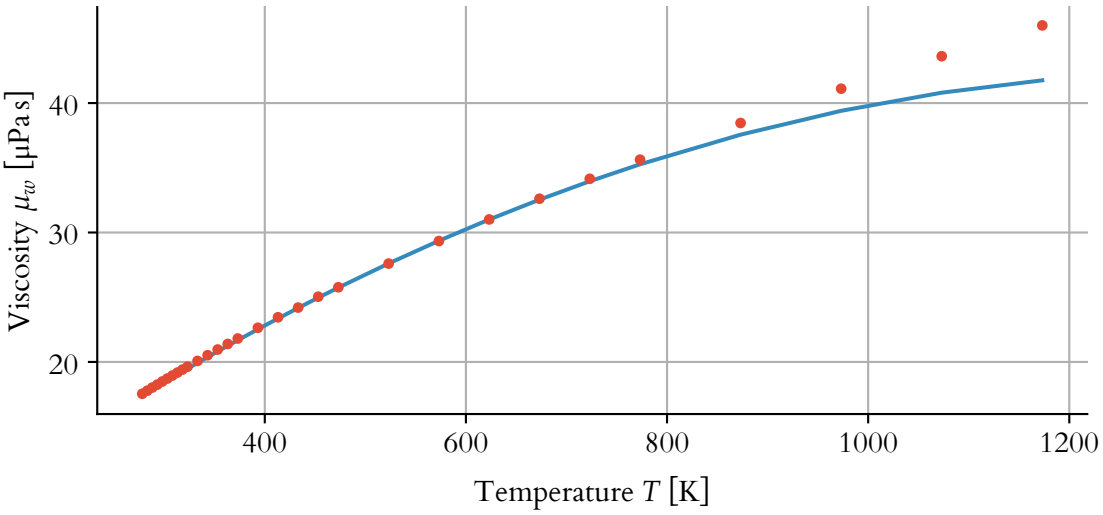

Figure 3.6.: Viscosity of dry air; experimental values (dots) and approximation by Gawin *et al.* [GMS99] (solid line).

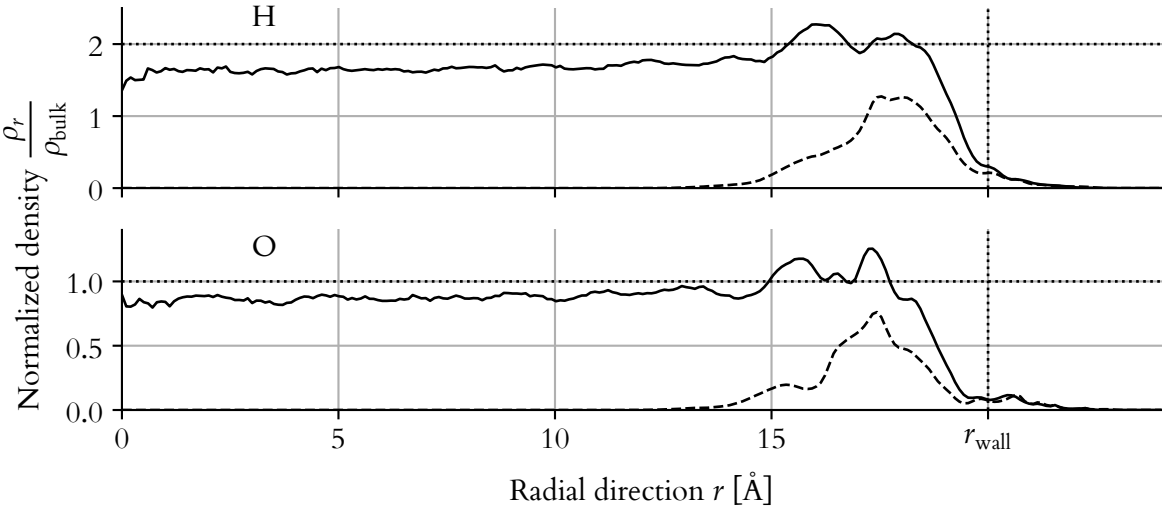

Figure 3.7.: Radial density distribution of hydrogen (top) and oxygen (bottom) atoms in a cylindrical pore. The solid lines represent hydration levels of 96 %, whereas the dashed lines are at 19 %. The density is normalized to the bulk density, indicated by the horizontal dotted line. The pore wall is shown as the vertical dotted line. This is a recreation of a figure from [HWS+00].

Table 3.1.: Relative diffusivity at a hydrophilic surface. The NMR data are from [HP86], while the MD results stem from [LR94].

	simulation (MD)	experimental (NMR)
radial D_{rad}/D_0	0.247	0.0003
lateral D_{lat}/D_0	0.378	0.1

be seen in fig. 3.7, there is a clear accumulation at the pore wall for lower hydration levels. Even for almost completely filled pores, the density in the first two water layers from the boundary is higher than for bulk water. Furthermore, up to 100 molecular layers from the SiO_2 surface may be more ordered than in bulk water [Ser80].

An NMR study from Halle and Piculell suggests an reduction in diffusivity by a factor of 200 to 500 at a colloid surface [HP86]. In contrast, a molecular dynamics simulation of water at hydrophilic surfaces shows a reduction in diffusivity by a factor of about three compared to bulk water [LR94]. The authors of the MD study speculate that this difference might be due to microporosity of the pore surface, which was not considered in their model. The reduction in diffusivity is stronger in radial than in lateral direction; see table 3.1.

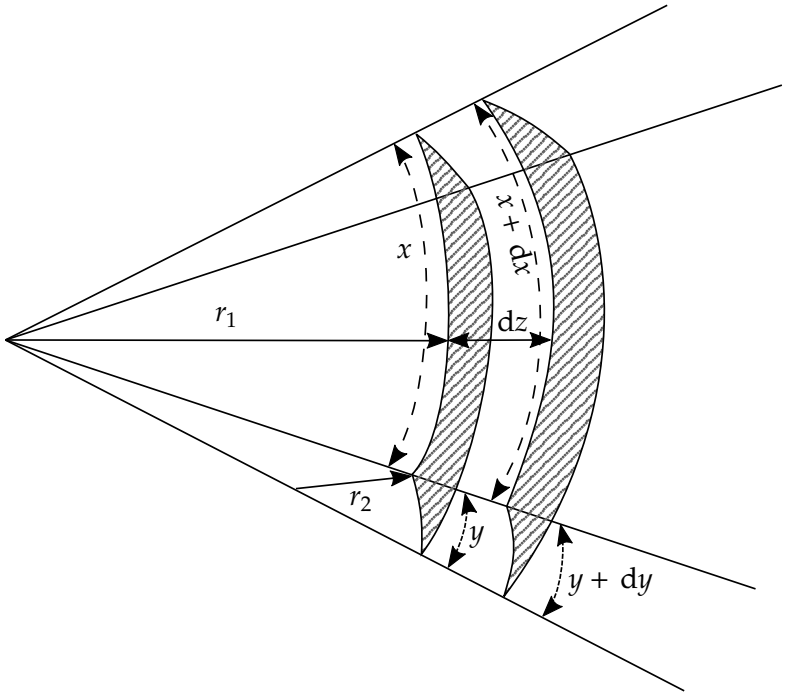

Figure 3.8.: Displacement dz of a surface segment of the capillary interface during expansion. Redrawn from [GS82].

3.4. Derivation of the Kelvin equation

The Kelvin equation is a central piece in the investigation of mesoporous media. It is used in virtually all methods connecting the adsorption isotherms to pore size distributions, and employed in numerical simulations to relate vapour and capillary pressure. As with any thermodynamic equation, it is subject to restrictions and tacit assumptions that limits its applicability. The aim of this derivation is to make them explicit.

First, the Young-Laplace equation will be derived. Consider a segment of the curved interface between a liquid and a vapour, as shown in fig. 3.8. When the system is in equilibrium, the work done to expand the surface is equal to the work of the volume expansion of the vapour under excess pressure. The first quantity is $\gamma\ \mathrm{d}A$, where γ is the surface tension and $\mathrm{d}A$ the change in surface area. The second quantity is $(p_v - p_l)\ \mathrm{d}V$, where p_v and p_l are the vapour and liquid pressure, respectively, and $\mathrm{d}V$ is the volume change. Since $\mathrm{d}A = x\ \mathrm{d}y + y\ \mathrm{d}x$ and $\mathrm{d}V = xy\ \mathrm{d}z$, the equation reads

$$\gamma(x\,\mathrm{d}y + y\,\mathrm{d}x) = (p_v - p_l)xy\,\mathrm{d}z. \tag{3.13}$$

For similar triangles in fig. 3.8, it follows that

$$\frac{x + \mathrm{d}x}{r_1 + \mathrm{d}z} = \frac{x}{r_1}, \qquad \frac{y + \mathrm{d}y}{r_2 + \mathrm{d}z} = \frac{y}{r_2}, \tag{3.14}$$

so that $\mathrm{d}x$ and $\mathrm{d}y$ can be rewritten in terms of $\mathrm{d}z$,

$$\mathrm{d}x = \frac{x}{r_1}\,\mathrm{d}z \qquad\qquad \mathrm{d}y = \frac{y}{r_2}\,\mathrm{d}z. \tag{3.15}$$

Substitution into the above results in the Young-Laplace equation,

$$p_v - p_l = \gamma\left(\frac{1}{r_1} + \frac{1}{r_2}\right). \tag{3.16}$$

The mean radius of curvature r_m is given by

$$\frac{2}{r_m} = \frac{1}{r_1} + \frac{1}{r_2}, \tag{3.17}$$

resulting in the alternative form

$$p_v - p_l = \frac{2\gamma}{r_m}. \tag{3.18}$$

Both phases are governed by the Gibbs-Duhem equation, which describes the relation between changes in chemical potentials

$$s_v\,\mathrm{d}T + V_v\,\mathrm{d}p_v + \mathrm{d}\mu_v = 0, \tag{3.19}$$
$$s_l\,\mathrm{d}T + V_l\,\mathrm{d}p_l + \mathrm{d}\mu_l = 0. \tag{3.20}$$

Here, s_α and μ_α are the specific entropies and chemical potentials, respectively. For an equilibrium displacement (no change in chemical potential) at constant temperature, a connection between the volume and pressure of the phases follows:

$$V_v\,\mathrm{d}p_v = V_l\,\mathrm{d}p_l. \tag{3.21}$$

With that, we can rewrite eq. (3.18)

$$\mathrm{d}\left(\frac{2\gamma}{r_m}\right) = \frac{V_l - V_v}{V_l}\,\mathrm{d}p_v. \tag{3.22}$$

Two additional assumptions are made: the molar volume of the liquid is very small compared to that of the vapour ($V_l \ll V_v$), and the vapour behaves like an ideal gas ($V_v = \frac{RT}{p_v}$). Then, the equation becomes

$$\mathrm{d}\left(\frac{2\gamma}{r_m}\right) = -\frac{RT}{V_l}\frac{\mathrm{d}p_v}{p_v}. \tag{3.23}$$

Integration between (r_m, p_v) and the saturation pressure p_{sat}, where the curvature is zero (the mean radius becomes infinite), leads to

$$\frac{2\gamma}{r_m} = \frac{RT}{V_l}\ln\left(\frac{p_{\mathrm{sat}}}{p_v}\right), \tag{3.24}$$

or equivalently

$$\ln\left(\frac{p_v}{p_{\text{sat}}}\right) = -\frac{2\gamma V_l}{RT}\frac{1}{r_m}. \tag{3.25}$$

During the integration, the liquid volume is assumed to be independent of pressure, i.e. the liquid is incompressible. Equation (3.25) is generally referred to as the Kelvin equation. This form of the Kelvin equation is used to relate the relative humidity p_v/p_{sat} to the radius of curvature, which in turn can be used to find the pore radius at which saturation occurs for a given relative humidity. It follows from the Kelvin equation that the vapour pressure over a concave meniscus is lower than the saturation vapour pressure p_{sat}.

4. Modeling multiphase flow in porous media

The amount of theoretical, experimental and numerical works on the mass and heat transport in concrete, and porous media in general, generated over the last century or so is enormous. Covering every model for flow in porous media is neither attainable nor desirable for this work. To this end, approaches that do not include a thermal model for high temperatures have not been considered, such as [BN72; Kün95; JN10]. Furthermore, single-phase models such as [BT78; IE04] have been excluded due to their known problems, namely being unable to distinguish components in the gas phase and explicitly taking phase changes (vaporization/condensation) into account.

4.1. Averaging theory

A physical description of the multiphase problem considers a heterogeneous medium of n separate phases. Each phase π occupies a different portion V_π of the total volume V. The subregions associated with each phase are separated by highly irregular interfaces. Continuity of thermodynamic quantities such as pressure holds within each phase, but over the whole space they are discontinuous. Balance laws in combination with interface and boundary conditions describe the state of the system. Solving the balance equations at the pore scale is not feasible; neither is the geometry of the phases and interfaces known, nor is the computational effort tractable for even small lab specimens, let alone real structures. Therefore, an averaging procedure is applied, whereby the equations are averaged over a representative volume. The goal is to find a set of equations where the phases and their associated quantities are continuous over the whole space.

On a microscopic level, the balance equation for a thermodynamic variable ψ within a phase π can be written as

$$\frac{\partial(\rho\psi)}{\partial t} + \operatorname{div}(\rho\psi\mathbf{v}) - \operatorname{div}\mathbf{i} = \rho f \quad \text{in } V_\pi, \tag{4.1}$$

where ρ is the mass density, $\mathbf{v}$ the velocity of the fluid, $\mathbf{i}$ is the flux associated with ψ and f is the sum of net production and external supply. To arrive at a macroscopic formulation, this equation has to be integrated over a suitable representative elementary volume (REV). The procedure was first described by Hassanizadeh and Gray [HG79] in 1979. A graphical representation of the averaging volume and the associated coordinate system can be seen in fig. 4.1.

In the macroscopic description, each point x in V is the center of an averaging volume v. Average quantities at that point are obtained by integrating over REV. An important consideration is the size of the averaging volume, which is subject to two conditions. Firstly, it has to be large enough so that changes in averaging volume no longer cause fluctuations

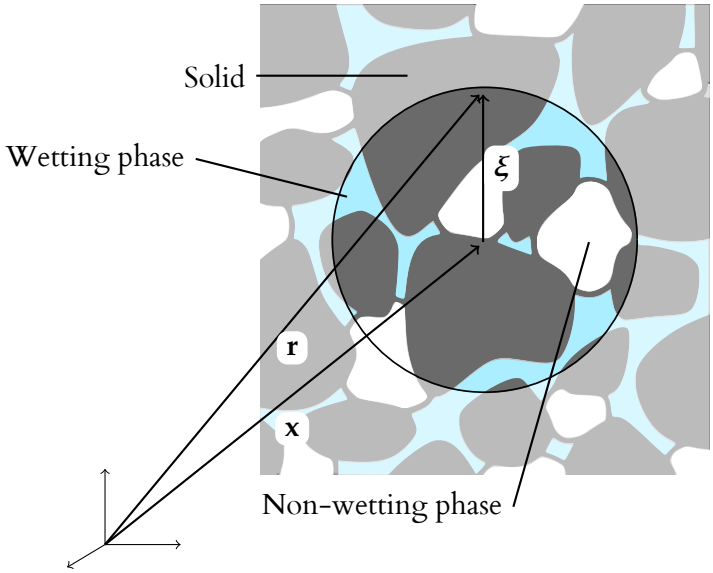

Figure 4.1.: A schematic representation of a REV for concrete. Based on a figure from [LS98].

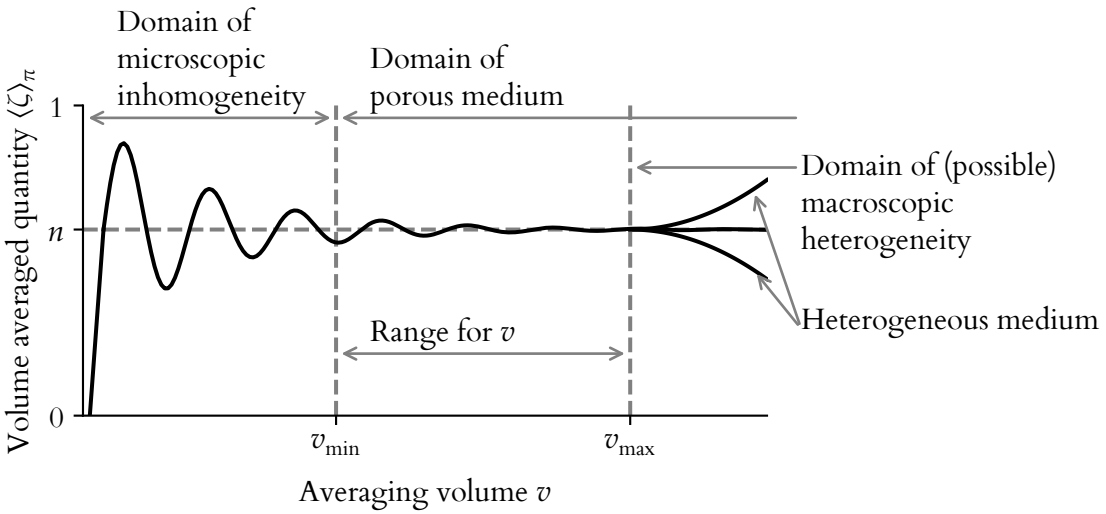

Figure 4.2.: Density varying with the integration volume. Based on a figure from [KGW12].

in the quantity to be averaged, that is the averaged quantity is independent of the REV size. Secondly, it has to be small enough to be considered infinitesimal for the derivatives in the governing macroscopic equations to be meaningful. For concrete, the averaging volume should also be small enough so that the heterogeneity due to the aggregates does not affect the averaging results. This combination of circumstances is depicted in fig. 4.2.

For a macroscopic description, a couple of averaging operators are necessary. For this, we first define a phase distribution function

$$\gamma_\pi(\mathbf{r}, t) = \begin{cases} 1 & \text{if } \mathbf{r} \in V_\pi, \\ 0 & \text{if } \mathbf{r} \notin V_\pi. \end{cases} \tag{4.2}$$

Now, we first define a volume average operator $\langle\cdot\rangle_\pi$,

$$\langle\zeta\rangle_\pi(\mathbf{x}, t) = \frac{1}{v} \int_v \zeta(\mathbf{r}, t)\, \gamma_\pi(\mathbf{r}, t)\ \mathrm{d}v \tag{4.3}$$

and then a mass average operator $\bar{\cdot}^\pi$,

$$\bar{\zeta}^\pi(\mathbf{x}, t) = \frac{1}{\langle\rho\rangle_\pi(\mathbf{x}, t)\, v} \int_v \rho(\mathbf{r}, t)\, \zeta(\mathbf{r}, t)\, \gamma_\pi(\mathbf{r}, t)\ \mathrm{d}v \tag{4.4}$$

For terms along the interfaces between phases, there are additional definitions necessary: $\mathbf{n}^{\pi\alpha}$ is the normal vector pointing from phase π to phase α, $\mathrm{d}a$ is a microscopic surface element, and $a^{\pi\alpha}$ is the surface between the phases π and α.

The macroscopic balance law is now derived by multiplying the microscopic balance law by γ_π, integrating over v and then integrating over the total volume V. The macroscopic quantities therein are given by the application of averaging operators applied to the microscopic quantities. Details on the derivation can be found in [HG79] or chapter 2 of [LS98].

The resulting balance equation for the macroscopic quantity $\bar{\psi}^\pi$ can be written as

$$\begin{aligned} \int_V \frac{\partial}{\partial t} \left(\langle\rho\rangle_\pi \bar{\psi}^\pi \right) \mathrm{d}V + \int_V \operatorname{div} \left(\langle\rho\rangle_\pi \bar{\psi}^p \bar{\mathbf{v}}^\pi \right) \mathrm{d}V \\ - \int_V \operatorname{div} \mathbf{i}^\pi\ \mathrm{d}V - \int_V \langle\rho\rangle_\pi \left(e^\pi(\rho\psi) + I^\pi \right) \mathrm{d}V \\ = \int_V \langle\rho\rangle_\pi \bar{f}^\pi\ \mathrm{d}V, \end{aligned} \tag{4.5}$$

where $\mathbf{i}^\pi$ is the averaged macroscopic flux associated with $\bar{\psi}^\pi$. The macroscopic equation contains two interaction terms. Exchange of $\bar{\psi}^\pi$ caused by mechanical interactions is described by

$$I^\pi = \frac{1}{\langle\rho\rangle_\pi v} \sum_{\alpha \neq \pi} \int_{a^{\pi\alpha}} \mathbf{n}^{\pi\alpha} \cdot \mathbf{i}\ \mathrm{d}a, \tag{4.6}$$

whereas phase changes and mass exchange are given by

$$e(\rho\psi) = \frac{1}{\langle\rho\rangle_\pi v} \sum_{\alpha \neq \pi} \int_{a^{\pi\alpha}} \rho\psi(\mathbf{w} - \dot{\mathbf{r}}) \cdot \mathbf{n}^{\pi\alpha}\ \mathrm{d}a, \tag{4.7}$$

where $\mathbf{w}$ is the velocity of the interface. The substitute continua fill the entire domain simultaneously.

Assuming certain smoothness conditions, the differential form of the macroscopic equation can be derived by localising eq. (4.5)

$$\begin{aligned} &\frac{\partial}{\partial t}\left(\langle\rho\rangle_\pi \bar{\psi}^\pi\right) + \operatorname{div}\left(\langle\rho\rangle_\pi \bar{\mathbf{v}}^\pi \bar{\psi}^\pi\right) - \operatorname{div}\mathbf{i}^\pi \\ &-\langle\rho\rangle_\pi\left(e(\rho\psi) + I^\pi\right) = \langle\rho\rangle_\pi \bar{f}^\pi \qquad \forall x \in V. \end{aligned} \tag{4.8}$$

4.2. Models under discussion

Two models in particular will be discussed in the following text. One is the model by Gawin *et al.*, which will be called GPS model going forward, and the other model was developed by Tenchev *et al.* and later modified by Davie *et al.* The latter will for simplicity be called the Tenchev model, even though he was neither the sole author of the first paper, nor a coauthor of later papers.

4.2.1. GPS model

The GPS model was developed and extended over a series of papers over the last two decades [GMS99; GPS02; GPS03; GPS04; GPS06]. This selection is a bit arbitrary, since it is of course based on theoretical work of others, e.g. [Whi77; BB86; HG79], as well preceded by other publications by the authors, e.g. [BMS95; GBS96; LS98]. The paper [GMS99] was chosen as a starting point to keep the scope manageable.

[GMS99] proposes a complete thermal-hygral-mechanical model for the behaviour of concrete at high temperatures, but restricted to a range below the critical point of water. All the major phenomena are considered, including capillary effects, dehydration and adsorbed water diffusion. As with all other high temperature models examined here, the hysteresis of the sorption isotherm is neglected. Particular emphasis has been placed on the interaction between the pore structure and diffusivity of the concrete (see section 4.4.2).

In [GPS02], the model is extended beyond the critical point by letting the capillary pressure (which has no meaning beyond the critical point) stand in for the product of water potential and water density. Numerically, a "switching procedure" is employed to separate the two different physical meanings of the same variable.

A thermo-chemical damage component has been introduced in [GPS03], and the behaviour of early age concrete including hydration has been added in [GPS06].

4.2.2. Tenchev model

The Tenchev model was first proposed in [TLP01], and then later modified and extended in [TP05; DPB06; DPB10]. Naturally, this work also did not appear in vacuum, and is based on the theoretical work of Luikov [Lui66].

In the initial paper [TLP01], a coupled thermo-hygral model is developed, yet coupling to mechanics is excluded. It is assumed that the capillary pressure is negligible. The influence of permeability, porosity and initial water content on the maximum pore pressure is investigated.

In 2005, Tenchev and Purnell published a model based on the previous paper, but now coupled to a mechanical damage model [TP05]. In this case, the damage model by Ortiz [Ort85] is employed, with a body force based on the gradient of the gas pressure field.

In [DPB06], model is modified to include the influence of capillary pressure. Additionally, the presence and potential flow of adsorbed water was considered in this work.

Davie *et al.* use an isotropic damage model in their subsequent paper [DPB10]. The total stress is modelled as the sum of the Bishop's stress and pore pressure. Additionally, a thermal damage parameter is used to describe the loss of stiffness due to increased temperatures. Lastly, a separate term for the load-induced thermal strains is added to the formulation.

4.3. Balance equations

The general form of the mass balance equations, namely of dry air, water vapour, liquid water and the solid matrix, is

$$\frac{\partial m_\pi}{\partial t} = r_\pi - \nabla \cdot J_\pi, \tag{4.9}$$

where m_π is the mass per unit volume, J_π is the mass flux and r_π is the mass source, each with respect to phase π ($\pi = a, v, w, s$).

4.3.1. Solid phase mass balance

The mass balance of the solid phase is typically not solved explicitly. It is given by

$$\frac{\partial m_s}{\partial t} = \dot{m}_{\text{dehyd}} - \nabla \cdot (m_s \mathbf{v}_s). \tag{4.10}$$

with the solid mass per unit volume $m_s = (1 - n)\rho_s$. This means that only two elements of the material parameter set $\{n, \rho_s, m_{\text{dehyd}}\}$ are independent.

Often the change in porosity is chosen as the dependent parameter to be computed. Rearranging eq. (4.10) gives

$$\frac{\partial n}{\partial t} = -\frac{\dot{m}_{\text{dehyd}}}{\rho_s} + \frac{1 - n}{\rho_s}\frac{\partial \rho_s}{\partial t} + \nabla \cdot ((1 - n)\mathbf{v}_s), \tag{4.11}$$

where the first term is the change due to dehydration water loss, the second due to intrinsic density changes and the last term due to deformations. The GPS model takes all of these factors into consideration, while the initial papers of the Tenchev model [TLP01; DPB06] did not take solve the mechanical problem, and therefore did not include the deformation term.

4.3.2. Dry air mass balance

The dry air mass conservation is described by

$$\frac{\partial m_a}{\partial t} = -\nabla \cdot J_a, \tag{4.12}$$

where m_a is the dry air mass per volume of porous medium and J_a is the dry air mass flux.

The mass per unit volume of dry air is given by

$$m_a = nS_g\rho^a = n(1 - S_w)\rho^a, \tag{4.13}$$

where n is the porosity, S_g and S_w the gas and liquid water saturation, respectively, and ρ_a is the density of dry air. Therefore, the time derivative can be expanded to

$$\frac{\partial m_a}{\partial t} = n(1 - S_w)\frac{\partial \rho_a}{\partial t} - \rho_a n\frac{\partial S_w}{\partial t} + \rho_a(1 - S_w)\frac{\partial n}{\partial t}. \tag{4.14}$$

The change air content due to change in saturation and air density, the first and second terms, is agreed upon among all models. The third term is only present for models that consider changes in porosity.

The mass flux is typically split into two contributions, an advective and a diffusive flux

$$J_a = n(1 - S_w)\rho_a\mathbf{v}_g + n(1 - S_w)\rho_g D\nabla\left(\frac{\rho_a}{\rho_g}\right). \tag{4.15}$$

4.3.3. Water mass balance

Free water is present in two different phases—as water vapour and as liquid water. This results in two mass balance equations,

$$\frac{\partial m_v}{\partial t} = \dot{m}_{\text{vap}} - \nabla \cdot J_v, \tag{4.16}$$

$$\frac{\partial m_w}{\partial t} = -\dot{m}_{\text{vap}} - \dot{m}_{\text{dehyd}} - \nabla \cdot J_w. \tag{4.17}$$

These are commonly summed up to get rid of the evaporation term, resulting in a balance of total water,

$$\frac{\partial (m_v + m_w)}{\partial t} = -\dot{m}_{\text{dehyd}} - \nabla \cdot (J_v + J_w). \tag{4.18}$$

The mass per unit volume of the water phases is given by

$$m_v = nS_g\rho^v = n(1 - S_w)\rho^v, \tag{4.19}$$

$$m_w = nS_w\rho^w. \tag{4.20}$$

The vapour flux also has an advective and a diffusion term,

$$J_v = n(1 - S_w)\rho_v\mathbf{v}_g + n(1 - S_w)\rho_g D\nabla\left(\frac{\rho_v}{\rho_g}\right). \tag{4.21}$$

The models do not agree on how to model the liquid water flux. In the original Tenchev model [TLP01], there is only an advective flow

$$J_w = nS_w\rho_w\mathbf{v}_w. \tag{4.22}$$

Both the modified model by Davie *et al.* [DPB06] and the GPS model consider adsorbed water diffusion in addition to advection, yet with different formulations. In [DPB06], the degree of saturation with bound water S_b

$$S_b = \begin{cases} S_w & \text{for } S_w \leqslant S_{\text{ssp}}, \\ S_{\text{ssp}} & \text{for } S_w > S_{\text{ssp}}, \end{cases} \tag{4.23}$$

is used to give the liquid water flux as a weighted sum of the advection and adsorbed water diffusion term,

$$J_w = \left(1 - \frac{S_b}{S_w}\right) nS_w\rho_w\mathbf{v}_w + \frac{S_b}{S_w} nS_w\rho_w\mathbf{v}_b, \tag{4.24}$$

whereas in [GMS99], it is described as a piecewise formulation

$$J_w = \begin{cases} nS_w\mathbf{v}_b & \text{for } S_w \leqslant S_{\text{ssp}} \\ nS_w\mathbf{v}_w & \text{for } S_w > S_{\text{ssp}}. \end{cases} \tag{4.25}$$

Practically, this only makes a difference in the capillary range ($S_w > S_{\text{ssp}}$), where the former formulation is multiplied by a factor of $1 - \frac{S_{\text{ssp}}}{S_w}$ compared to the latter.

4.3.4. Enthalpy balance

The enthalpy balance can be written as

$$\begin{aligned} (\rho C_p)_{\text{eff}} \frac{\partial T}{\partial t} + \left(\rho_w C_{\text{pw}}\mathbf{v}_w + \rho_g C_{\text{pg}}\mathbf{v}_g\right) \cdot \nabla T - \nabla \cdot (\lambda_{\text{eff}} \nabla T) = \\ -\dot{m}_{\text{vap}}\Delta H_{\text{vap}} - \dot{m}_{\text{dehyd}}\Delta H_{\text{dehyd}}. \end{aligned} \tag{4.26}$$

Most of this equation is shared by all models. In the earlier papers of the GPS model, namely [GMS99; GPS02], the vaporization enthalpy term was replaced by a piecewise formulation,

$$\Delta H_{\text{phase}} = \begin{cases} \Delta H_{\text{adsorp}} & \text{for } S \leqslant S_{\text{ssp}}, \\ \Delta H_{\text{vap}} & \text{for } S > S_{\text{ssp}}, \end{cases} \tag{4.27}$$

that differentiated between vaporization and adsorption enthalpy. In the later papers ([GPS03; GPS11a]), this was no longer applied. Furthermore, the sign of the dehydration term is not consistent over the different publications of the GPS model.

4.4. Constitutive relations

4.4.1. Advection

The advective component is described by Darcy's law, but there is disagreement between the formulations. For the gas advection, the following variants are given:

$$n(1 - S_w)\mathbf{v}_g = -\frac{k k_{\mathrm{rg}}}{\mu_g}\nabla p_g \qquad \text{[LS98; GPS11a]}, \tag{4.28}$$

$$\mathbf{v}_g = -\frac{k k_{\mathrm{rg}}}{\mu_g}\nabla p_g \qquad \text{[TLP01; DPB06]}, \tag{4.29}$$

$$\mathbf{v}_g = -\kappa\frac{k k_{\mathrm{rg}}}{\mu_g}\nabla p_g \qquad \text{[DPB10]}. \tag{4.30}$$

For the liquid water advection, they are

$$nS_w\mathbf{v}_w = -\frac{k k_{\mathrm{rw}}}{\mu_w}\nabla p_w \qquad \text{[LS98; GPS11a]}, \tag{4.31}$$

$$\mathbf{v}_w = -\frac{k k_{\mathrm{rw}}}{\mu_w}\nabla p_w \qquad \text{[TLP01; DPB06]}. \tag{4.32}$$

Intrinsic permeability

As seen in section 2.2, the permeability increases with rising temperatures. Several constitutive equations have been proposed to model this change in permeability.

In [GMS99], the intrinsic permeability depends on temperature and gas pressure,

$$k = k_0 10^{A_T(T - T_{\mathrm{ref}})}\left(\frac{p_g}{p_{\mathrm{go}}}\right)^{A_p}, \tag{4.33}$$

where A_T and A_p are material parameters. This relation is modified in [GPS03] to include the effect of damage,

$$k = k_0 10^{f(T)}\left(\frac{p_g}{p_{\mathrm{go}}}\right)^{A_p} 10^{A_d D}, \tag{4.34}$$

with

$$f(T) = A_T^2(T - T_{\mathrm{ref}})^2 + A_T^1(T - T_{\mathrm{ref}}), \tag{4.35}$$

where A_p, A_d, A_T^1 and A_T^2 are material parameters and D is the total damage. No indication on how one might identify the values of the parameters by experiment is provided. The exponential behaviour is a reasonable conclusion from looking at fig. 2.1, yet how the dependence on gas pressure arises remains unclear.

Here, a modified version of eq. (4.33) without damage and gas pressure dependence is used, given by

$$k = k_0 10^{A_k(T - T_{\mathrm{ref}})}, \tag{4.36}$$

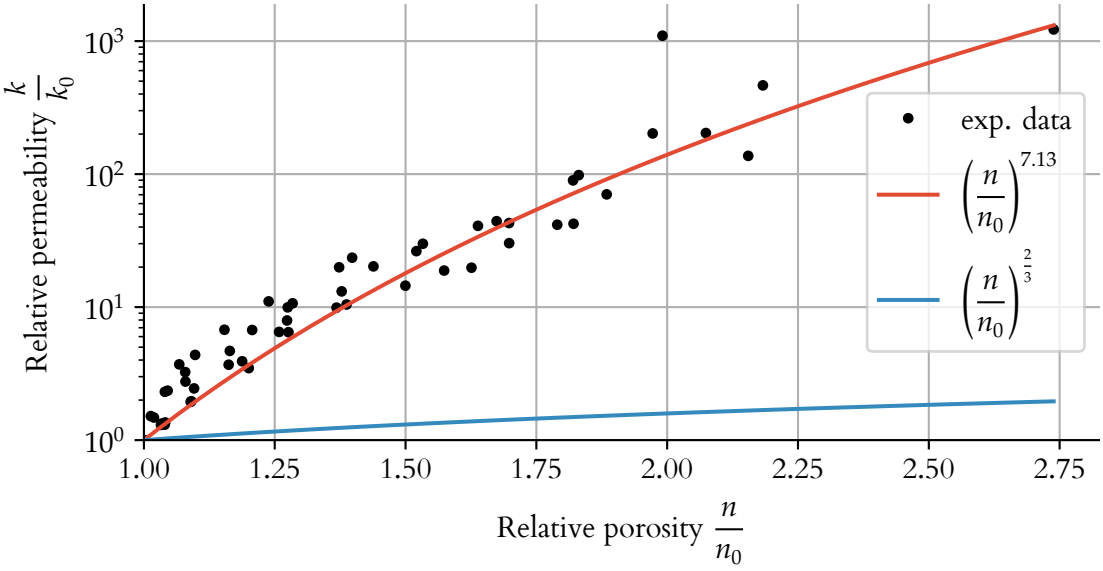

Figure 4.3.: Relationship between changes in porosity and permeability: experimental findings from [SH89] and model proposed in [DPB06].

where k_0 is the intrinsic permeability at the reference temperature T_{ref} and A_k is a material constant.

Davie *et al.* [DPB06] propose a constitutive relation to this effect

$$k = k_0 \left(\frac{n}{n_0}\right)^{2/3}, \tag{4.37}$$

where k_0 and n_0 are initial permeability and porosity, respectively. The exponent, however, is too small to fit the experimental data, as can be seen in fig. 4.3. The best least-squares fit for this particular dataset is achieved with an exponent of 7.13.

In their subsequent formulation including a mechanical coupling [DPB10], it is given by

$$k = k_0 10^{4(1-D)}, \tag{4.38}$$

where D is the multiplicative thermal-mechanical damage, $D = \omega + \chi - \omega\chi$.

Klinkenberg effect

In [DPB10], Darcy's law includes an additional factor κ, the gas-slip modification factor. It is given by

$$\kappa = 1 + b\frac{p_{\text{atm}}}{p_g}, \tag{4.39}$$

with

$$b = e^{-0.5818 \ln(k/1\,\text{m}^2) - 19.1213}, \tag{4.40}$$

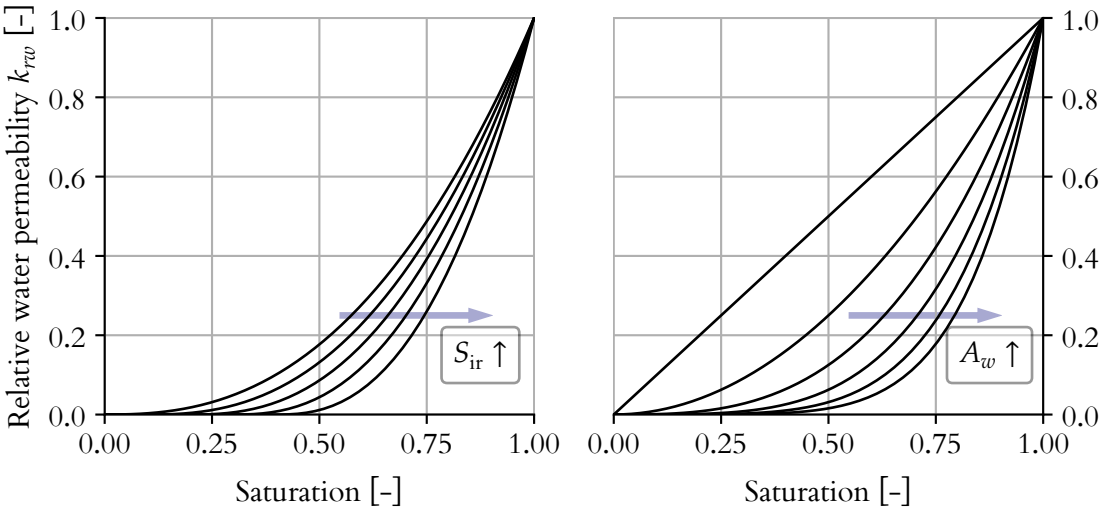

Figure 4.4.: Influence of S_{ir} (left, $A_w = 2.5$) and A_w (right, $S_{ir} = 0$) on the relative water permeability in [GMS99]

where p_{atm} is the atmospheric pressure and b is the Klinkenberg or slip-flow constant. This modification was originally proposed by Chung and Consolazio [CC05].

Relative permeabilities

The relative permeabilities are assumed to depend on the liquid water saturation of the pores, with higher saturation aiding liquid advection and inhibiting gas advection, and vice versa for lower saturation. Different formulations have been proposed and will be discussed below. It should be noted, however, that none of them have been justified by reference to experimental data.

The relative water permeability k_{rw} is described in [GMS99] as increasing with growing liquid water saturation,

$$k_{rw} = \begin{cases} \left(\frac{S - S_{ir}}{1 - S_{ir}}\right)^{A_w} & \text{for } S > S_{ir}, \\ 0 & \text{for } S \leqslant S_{ir}, \end{cases} \tag{4.41}$$

where S_{ir} is the irreducible saturation, often assumed to be zero, and A_w is a parameter between 1 and 6. An increase of A_w leads to a lower permeability at lower saturations, with a steeper climb as the fully saturated state is approached. Introducing an irreducible saturation different from zero retards the onset of advective flow until higher saturations are reached. This dependence on these parameters can be seen in fig. 4.4.

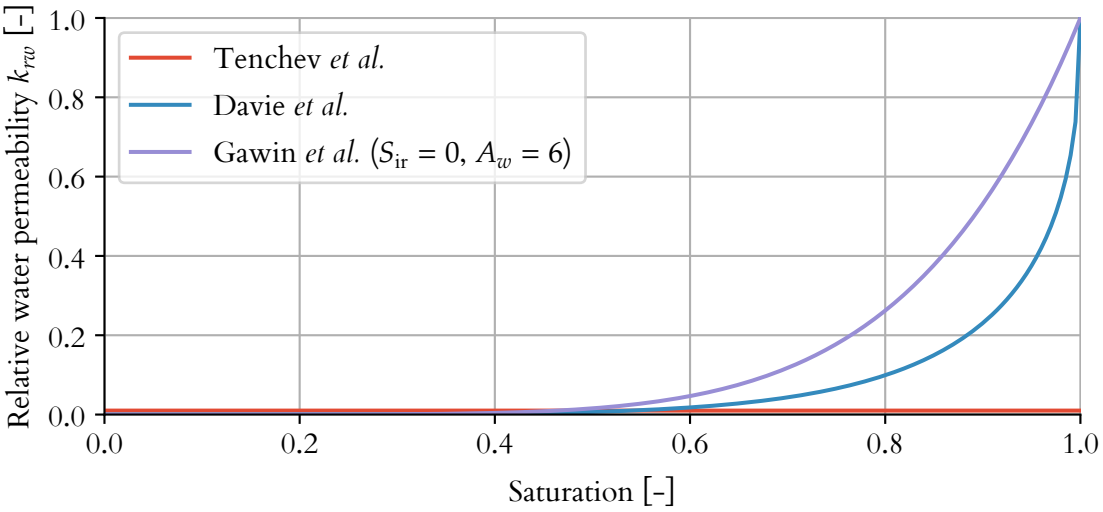

Figure 4.5.: Comparison of relative water permeability formulations

An alternative, described in the same paper, uses the both the saturation and the relative humidity as variables,

$$k_{\mathrm{rw}} = \left[1 + \left(\frac{1 - rh}{0.25}\right)^{B_w}\right]^{-1} S_w^{A_w}. \tag{4.42}$$

Later descriptions of the GPS model use the former formulation, with S_{ir} set to zero.

In the initial Tenchev model [TLP01], the authors note an reduction of the water pressure by a factor of 100 compared to the gas pressure, caused by capillary effects. As a way of including these effects indirectly, they set the relative water permeability to 0.01.

The modified model by Davie *et al.* uses the description from [BMLC99]

$$k_{\mathrm{rw}} = \sqrt{S_w}\left[1 - (1 - S_w^{1/m})^m\right]^2, \tag{4.43}$$

where the parameter m is given as 1/2.2748. A comparison of the equations put forward is seen in fig. 4.5.

The relative gas permeability is given in the initial Tenchev model as a simple linear relation,

$$k_{\mathrm{rg}} = 1 - S_w. \tag{4.44}$$

As with k_{rw}, the modified model uses the equation from Baroghel-Bouny *et al.*,

$$k_{\mathrm{rg}} = \sqrt{1 - S_w}\left(1 - S_w^{1/m}\right)^{2m}, \tag{4.45}$$

where m is the same as above.

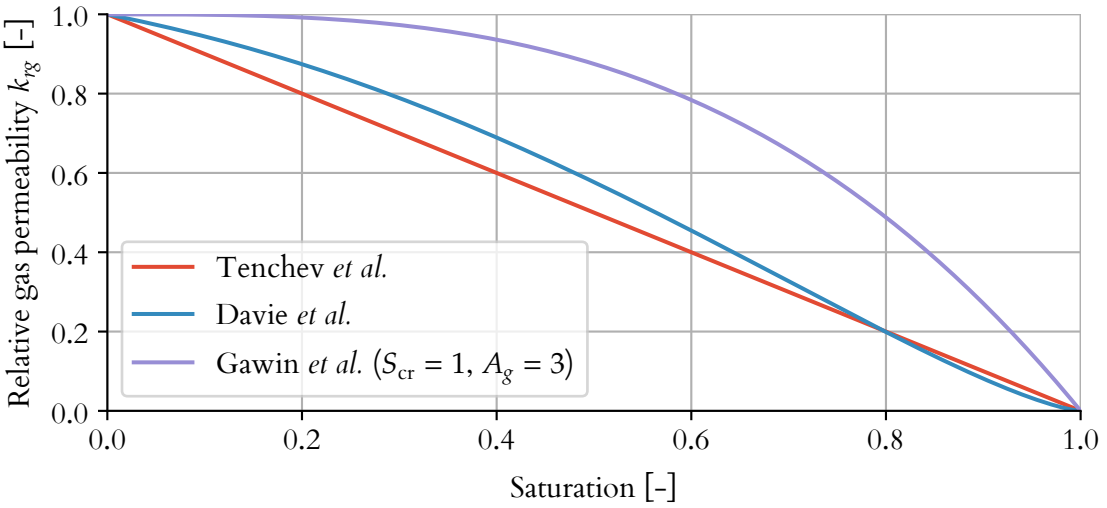

Figure 4.6.: Comparison of relative gas permeability formulations

In [GMS99], a piecewise formulation is used in this case as well

$$k_{\mathrm{rg}} = \begin{cases} 1 - \left(\frac{S_w}{S_{\mathrm{cr}}}\right)^{A_g} & \text{for } S < S_{\mathrm{cr}}, \\ 0 & \text{for } S \geqslant S_{\mathrm{cr}}, \end{cases} \tag{4.46}$$

where the S_{cr} is the critical saturation, above which no gas flow occurs. The parameter A_g takes values between 1 and 3; no values for S_{cr} are given. Decreasing the critical saturation shifts the curves to lower saturations; increasing A_w leads to higher flow in low and medium saturation conditions, with a faster diminishing as the critical saturation is approached. Later papers of the GPS model set the critical saturation to one.

A comparison of the formulations can be seen in fig. 4.6. For $A_g = 1$, $S_{\mathrm{cr}} = 1$, the graphs for the GPS model and the initial Tenchev model coincide.

4.4.2. Diffusion

Several different constitutive models are given here. Unfortunately, as already mentioned in section 2.3, the experimental evidence for these is quite weak.

Two different descriptions for the diffusion coefficient are given in [GMS99]. The simpler one is

$$D = n(1 - S_w)\tau D_{va}(T, p_g), \tag{4.47}$$

where τ is the tortuosity factor, with a typical value between 0.4 and 0.6 for concrete. The diffusion coefficient for water vapour in air, D_{va}, depends on the temperature and gas pressure,

$$D_{va} = D_{v0}\left(\frac{T}{T_0}\right)^{B_v} \frac{p_0}{p_g}, \tag{4.48}$$

where the value of the parameter B_v is typically given as 1.667.

The second formulation introduces a parameter to the saturation dependency, A_v, and replaces the tortuosity factor τ with a "structure factor" f_s,

$$D = n(1 - S_w)^{A_v} f_s D_{va}(T, p_g). \tag{4.49}$$

Values for A_v are typically in the range $[1, 3]$. The evaluation of the structure factor is more involved.

The basic approach is to integrate over a pore size distribution obtained from mercury porosimetry. Two different formulas were examined in [GMS99], where the diffusion coefficient can be calculated for a particular value of S_w. The first was proposed by Daian [Dai88],

$$D(S_w(r_k)) = \tau D_{va}(T, p_g) \int_{r_k}^{\infty} \left(\frac{r - t_a}{r}\right)^2 \frac{1}{1 + l_m/(2(r - t_a))} \, \mathrm{d}\eta(r), \tag{4.50}$$

where r_k is the radius of pores filled up by the saturation S_w, l_m is the mean free path of water molecules in air, t_a is the thickness of the adsorbed water layer and $\mathrm{d}\eta(r)$ is the volume fraction of pores with radii between r and $r + \mathrm{d}r$. The second one was proposed by Chaube *et al.* [CSM93] using percolation theory,

$$D(S_w(r_k)) = D_{va}(T, p_g) \frac{r_m V(r_m)}{r_c} \int_{r_k}^{\infty} \frac{1}{1 + l_m/(2(r - t_a))} \, \mathrm{d}\eta(r), \tag{4.51}$$

where $V(r)$ is the fraction of pores with radius larger than r and $r_m = \operatorname{argmax}(rV(r))$.

This procedure is demonstrated for a B-35 basalt concrete based on the pore size distribution measured by Schneider and Herbst [SH89], which can be seen in fig. 4.7. The results differ greatly between the two formulas (see fig. 4.8), with a reduction from 50% to complete arrest of diffusion. According to [GMS99], the formula by Chaube *et al.* is more realistic. Later papers of the GPS model do not explicitly describe the diffusion formulation in use, but instead reference the initial paper [GMS99].

In the Tenchev model, a much simpler approach has been chosen

$$D = \frac{\delta}{\tau^2} D_{va}. \tag{4.52}$$

where δ and τ are the constrictivity and tortuosity, with typical values of 0.5 and 3, respectively. The formulation of the vapour diffusion in air also differs, with

$$D_{va} = D_{\mathrm{vo}} \left(\frac{T}{1\,\mathrm{K}}\right)^{2.072} \frac{1\,\mathrm{Pa}}{p_g}. \tag{4.53}$$

with $D_{\mathrm{vo}} = 1.89 \times 10^{-5}\,\mathrm{m^2\,s^{-1}}$. Note that the definitions of the tortuosity seem to differ, with higher values resulting in a lower diffusivity in the Tenchev model, while higher values lead to a higher diffusivity in the GPS model.

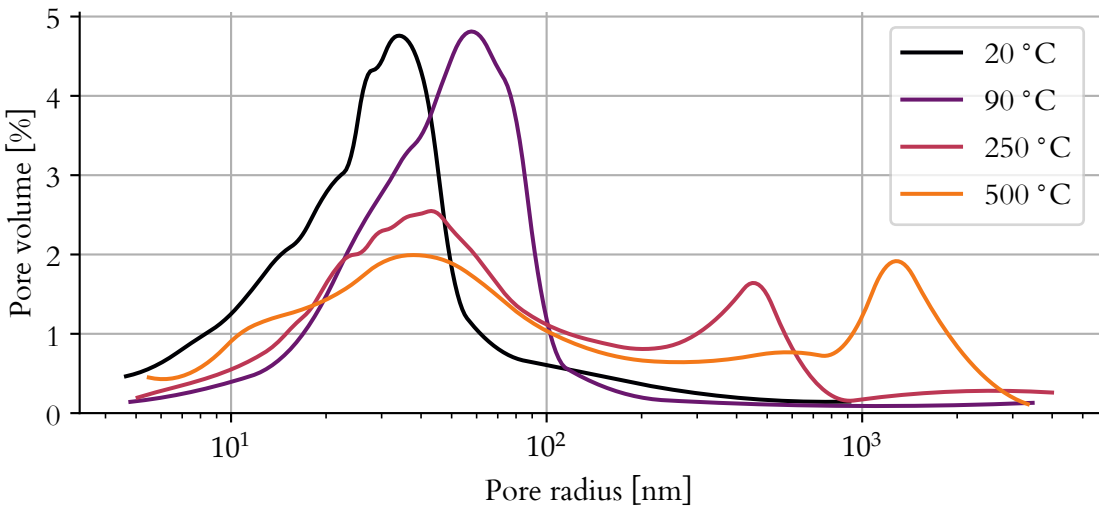

Figure 4.7.: Pore size distribution for a B-35 basalt concrete after heating to four different temperatures.

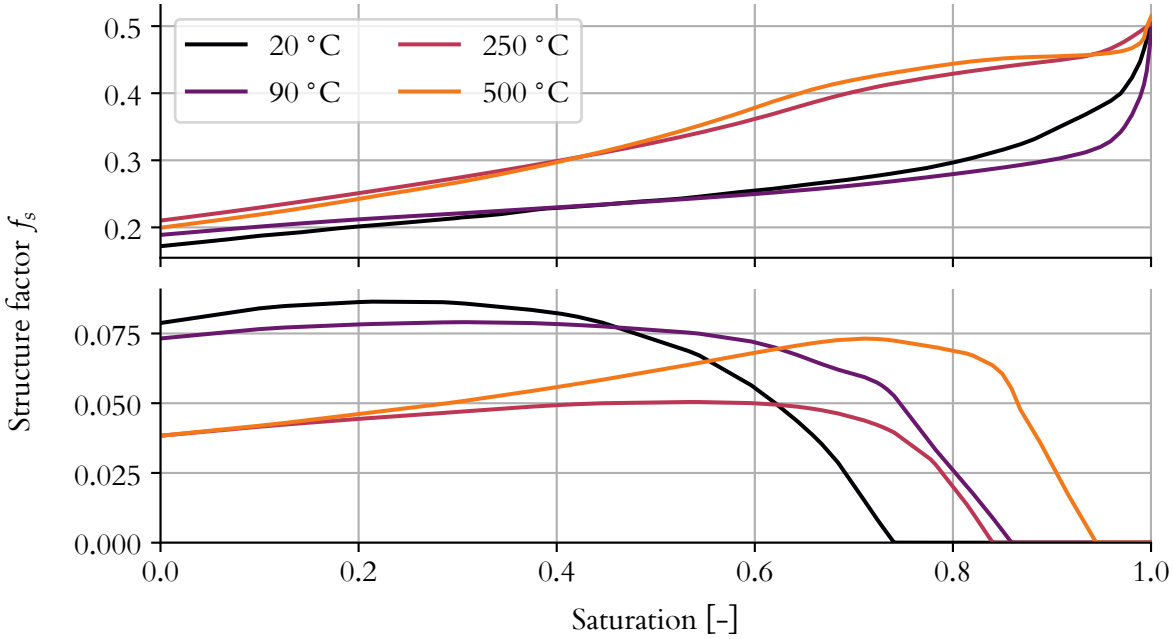

Figure 4.8.: Structure coefficient according to formula from Daian (top) and according to Chaube *et al.* (bottom).

4.4.3. Adsorbed water diffusion

Another diffusion phenomenon is the flow of adsorbed water. There is no consensus on whether the bound water is fixed on the surface [Dai88], its diffusion is so small that it can be neglected [TLP01], or that it should be explicitly considered [GPS11a].

In the papers that do consider adsorbed water diffusion, the formulation is the same,

$$\mathbf{v}_b = -\mathbf{D}_b \nabla S_b, \tag{4.54}$$

where $\mathbf{D}_b$ is the bound water diffusion tensor, and S_b the saturation with adsorbed water,

$$S_b = \begin{cases} S & \text{for } S \leqslant S_{\text{ssp}}, \\ S_{\text{ssp}} & \text{for } S > S_{\text{ssp}}. \end{cases} \tag{4.55}$$

S_{ssp} is the solid saturation point, that is the amount of water in the pores where no further water can be bound to the surface. The diffusivity is then assumed to be isotropic ($D_b\mathbf{I} = \mathbf{D}_b$, where $\mathbf{I}$ is the identity tensor), and given as a decreasing exponential function of both temperature and saturation

$$D_b = D_{b0} \exp\left(-2.08 \frac{S}{S_{\text{ssp}}} \frac{T}{T_{\text{ref}}}\right). \tag{4.56}$$

D_{b0} equal to $1.57 \times 10^{-11}\,\text{m}^2\,\text{s}^{-1}$ is used in [GMS99] and [DPB06], regardless of concrete mix. In [DPB06], a numerical value of 0.55 is given for the solid saturation point; in the GPS model description, no value is given. In [DPB06], this model was used, and the authors concluded that the adsorbed water flow was indeed negligible.

4.4.4. Sorption

A common choice for the capillary curves is the model proposed by Baroghel-Bouny *et al.* [BMLC99]. Based on fitting experimental data for four different concrete mixes, the following formulation is obtained

$$p_c(S_w) = a(S_w^{-b} - 1)^{1-1/b}, \tag{4.57}$$

where a and b are material parameters. Solving for the saturation gives

$$S_w = \left(\left(\frac{p_c}{a}\right)^{\frac{b}{b-1}} + 1 \right)^{\frac{-1}{b}}. \tag{4.58}$$

The capillary pressure p_c can be calculated from the Kelvin equation (see section 3.4)

$$p_c = \rho_w \frac{RT}{M_w} \ln\left(\frac{p_v}{p_{\text{vs}}}\right), \tag{4.59}$$

where p_{vs} is the saturation vapour pressure.

For higher temperatures, this has been modified in [GPS11a] to read

$$p_c(S_w) = \frac{a}{E}(S_w^{-b} - 1)^{1-1/b}, \tag{4.60}$$

where b is still a constant, yet a and the newly introduced E vary with temperature,

$$a = \begin{cases} \text{constant} & \text{for } T \leqslant 100\,^\circ\text{C} \\ (Q_3 - Q_2)\left[2\left(\frac{T-T_b}{T_{crit}-T_b}\right)^3 - 3\left(\frac{T-T_b}{T_{crit}-T_b}\right)^2 + 1\right] + Q_2 & \text{otherwise} \end{cases} \tag{4.61}$$

$$E = \begin{cases} \left(\frac{T_{crit}-T_0}{T_{crit}-T}\right)^N & \text{for } T < T_{crit} \\ \frac{N}{z}E_0 T + \left[E_0 - \frac{N}{z}E_0(T_{crit} - z)\right] & \text{for } T \geqslant T_{crit}. \end{cases} \tag{4.62}$$

Neither of the models considers the hysteresis between the sorption and desorption branches that appear in experiments.

4.4.5. Dehydration, porosity and skeleton density

As indicated in section 4.3.1, the three descriptions for dehydration, porosity and skeleton density are not independent; they have to fulfill the solid mass balance. Because of this, they will be discussed together.

Dehydration is the chemical process whereby chemically-bound water from the hardened cement paste is released into the pore space as temperatures increase. Heating above 105 °C releases non-evaporable water (hydration water) which occupies part of the gel pores or is chemically bound in chemical phases. Most models in the literature are calibrated using data from thermogravimetric or differential thermal analysis. More information on the experimental side can be found in section 2.5.

Several formulations have been proposed for the dehydration in numerical models. For better comparison, all models have been brought to the same form,

$$m_{dehyd}(T) = c\nu\Gamma(T), \tag{4.63}$$

where c is the cement content ($\mathrm{kg\,m^{-3}}$), ν is the mass ratio of maximally released water to cement content, and Γ is the dehydration degree ($\Gamma \in [0,1]$). A common assumption is that water loss below 105 °C is water evaporation, with dehydration remaining zero; the constant $T_d = 378.15\,\mathrm{K}$ will be used in these cases. The dehydration degree is a function of the highest temperature reached in the materials history, $\Gamma(t) = \Gamma(T_{max}(t))$, and therefore $\dot{\Gamma} = 0$ for $T(t) < T_{max}(t)$.

In the initial paper for the GPS model [GMS99], an extremely simplified linear model,

$$\Gamma = \frac{T - T_0}{T_{max} - T_0}, \tag{4.64}$$

is used. In [GPS03], only the dehydration mass rate as a function of the rate of the dehydration degree is given as

$$\dot{m}_{\text{dehyd}} = \rho_s a_h \frac{\mathrm{d}\Gamma}{\mathrm{d}t}, \tag{4.65}$$

but the function for the dehydration degree Γ was not specified. In the formulation proposed by Pesavento, $\nu = f_s m$, where f_s is the stoichiometric factor and m is the ageing degree [Pes00]. The dehydration degree is given as a function of temperature

$$\Gamma = \begin{cases} 0 & \text{for } T \leqslant T_d, \\ \frac{1}{2}\left(1 + \sin\left(\frac{1}{2}\pi - \pi \mathrm{e}^{k(T-T_d)}\right)\right) & \text{for } T > T_d. \end{cases} \tag{4.66}$$

In [GPS11a] this approach was also used, but with a cubic polynomial for the dehydration degree

$$\Gamma = \begin{cases} 0 & \text{for } T \leqslant T_d, \\ a_3(T - T_d)^3 + a_2(T - T_d)^2 + a_1(T - T_d) & \text{for } T > T_d, \end{cases} \tag{4.67}$$

with the material parameters $a_1 = 1.7151 \times 10^{-3}\,\mathrm{K}^{-1}$, $a_2 = -4.0006 \times 10^{-7}\,\mathrm{K}^{-2}$ and $a_3 = -2.9507 \times 10^{-10}\,\mathrm{K}^{-3}$. There is no explanation as to how they arrived at this function, and the reference given ([GPS04]) does not contain the information the authors claimed.

The formulation by Tenchev *et al.* prescribes $\nu = 0.09$ and a step-wise linear dehydration degree

$$\Gamma = \begin{cases} 0 & \text{for } T \leqslant 200\,^\circ\mathrm{C}, \\ 7.78 \times 10^{-3}(T - 200\,^\circ\mathrm{C}) & \text{for } 200\,^\circ\mathrm{C} < T \leqslant 300\,^\circ\mathrm{C}, \\ 4.44 \times 10^{-4}(T - 300\,^\circ\mathrm{C}) + 0.78 & \text{for } 300\,^\circ\mathrm{C} < T \leqslant 800\,^\circ\mathrm{C}, \\ 1 & \text{for } T > 800\,^\circ\mathrm{C}. \end{cases} \tag{4.68}$$

Dwaikat and Kodur use a very similar expression [DK09], with $\nu = 0.24$ and

$$\Gamma = \begin{cases} 0 & \text{for } T \leqslant 100\,^\circ\mathrm{C}, \\ 0.167\frac{T - 100\,^\circ\mathrm{C}}{100\,^\circ\mathrm{C}} & \text{for } 100\,^\circ\mathrm{C} < T \leqslant 700\,^\circ\mathrm{C}, \\ 1 & \text{for } T > 700\,^\circ\mathrm{C}. \end{cases} \tag{4.69}$$

The description by Pont and Ehrlacher is one of the few approaches that takes the kinetics of the dehydration process into account [PE04]. The dehydration evolution is described by the differential equation

$$\dot{m}_{\text{dehyd}} = -\frac{1}{\tau}\left(m_{\text{dehyd}} - m^{\text{eq}}_{\text{dehyd}}(T)\right), \tag{4.70}$$

where τ is the characteristic time of mass loss and $m^{\text{eq}}_{\text{dehyd}}$ is the amount of water created at equilibrium, using the notation of this section,

$$m^{\text{eq}}_{\text{dehyd}} = c\nu\Gamma(T). \tag{4.71}$$

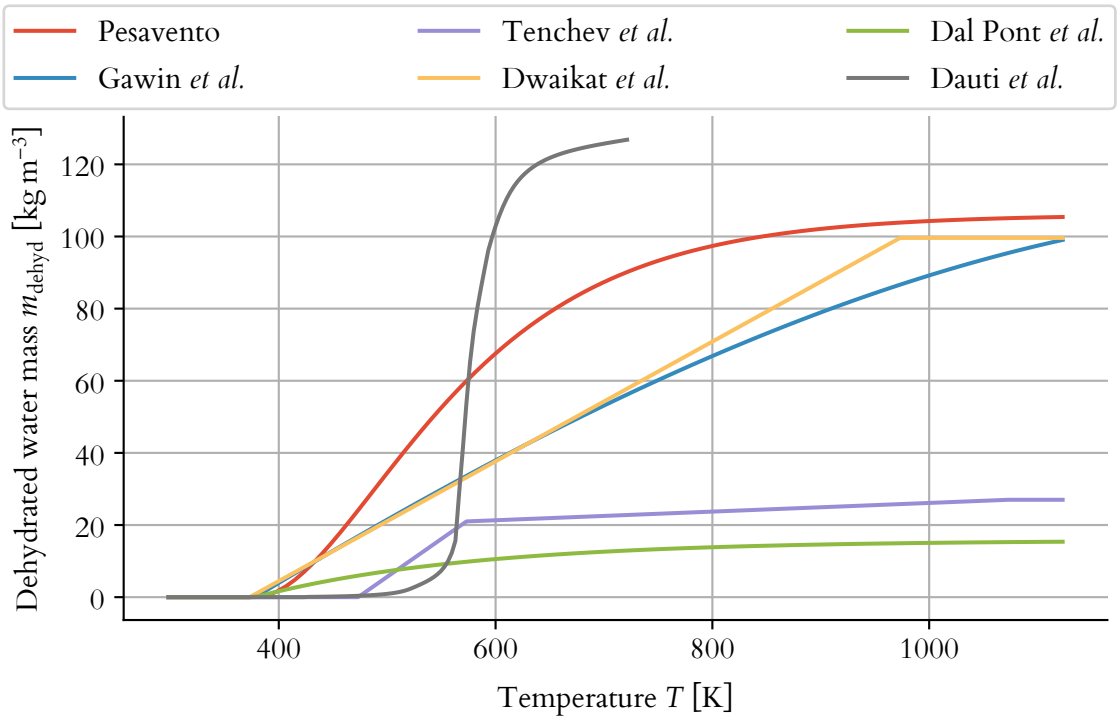

Figure 4.9.: Comparison of dehydration descriptions. For the description by Pont and Ehrlacher, the equilibrium dehydration mass is plotted.

The value of ν is given as 0.075 and the dehydration degree is

$$\Gamma = \begin{cases} 0 & \text{for } T \leqslant T_d, \\ 1 - \exp\left(-\frac{T - T_d}{200\,\text{K}}\right) & \text{for } T > T_d. \end{cases} \tag{4.72}$$

The value for the characteristic time is given in [PE04] as three hours.

All of the previous approaches are based on thermogravimetric analysis curves. TGA data are highly influenced by sample size, heating rate and vapour pressure [LSS16]. The data used in these approaches were obtained on very small samples, low heating rates and in dry conditions. Furthermore, the results of TGA also include the CO_2 released from carbonates.

These conditions do not necessarily apply to specimens tested for water migration and spalling risk under high temperatures. As a way of correcting for these discrepancies while keeping the function-of-temperature approach, Dauti *et al.* perform an inverse analysis on measured neutron radiography data [DDW+18]. The result is a much steeper curve (see fig. 4.9). This result, however, cannot be directly used in other simulations, since it reflects the sample size, heating rate and pore vapour state of their experiments. The given graph also does not extend beyond 450 °C.

Since the authors Dauti *et al.* have not provided an analytic description of their dehydration model, a logistic function was fitted to the given graph to obtain a mathematical expression

as,

$$\Gamma(T) = \frac{a}{1 + \mathrm{e}^{-k(T-T_0)}}. \tag{4.73}$$

For the curve presented in their paper, the best fit is obtained with $a = 0.8219$, $k = 0.0876\,\mathrm{K}^{-1}$ and $T_0 = 578.1\,\mathrm{K}$.

A graphical comparison of the discussed dehydration formulations can be seen in fig. 4.9.

The porosity evolution is described in [TLP01] as an empirical function,

$$n = f_n(T) + n_0, \tag{4.74}$$

noting that factors such as dehydration, chemical decomposition of aggregates, thermal strains and microcracking contribute to its increase. The authors also note that if only dehydration were considered, this would reduce to

$$n = \frac{m_{\mathrm{dehydr}}}{\rho_w} + n_0. \tag{4.75}$$

The actual description assumes the porosity to stay constant below $100\,^\circ\mathrm{C}$, three times the initial porosity above $800\,^\circ\mathrm{C}$ and a cubic polynomial in the range $T \in [100\,^\circ\mathrm{C}, 800\,^\circ\mathrm{C}]$:

$$n = n_0 \cdot \begin{cases} 1 & \text{for } T < 100\,^\circ\mathrm{C}, \\ aT^3 + bT^2 + cT + d & \text{for } 100\,^\circ\mathrm{C} \leqslant T \leqslant 800\,^\circ\mathrm{C}, \\ 3 & \text{for } T > 800\,^\circ\mathrm{C}. \end{cases} \tag{4.76}$$

The coefficients of the polynomial are chosen such that the porosity is C^1 continuous.

In the GPS model, the porosity is described as a simple linear function,

$$n = n_0 + A_n(T - T_0), \tag{4.77}$$

with initial porosities given between 0.06 and 0.087, and the constant A_n in the range $1.63 \times 10^{-4}\,\mathrm{K}^{-1}$ to $1.95 \times 10^{-4}\,\mathrm{K}^{-1}$. A much larger range of initial porosities (between 0.0512 and 0.13) are reported in later papers [GPS02; GPS11b]. They also note that dehydration is only one factor driving the change in porosity, preferring the above empiric relation to a direct, dehydration-only description.

The skeleton density is assumed to be constant in the Tenchev model, which is in conflict with the simultaneous prescription of both the dehydration water mass (eq. (4.68)) and the porosity (eq. (4.76)) while still maintaining the solid mass balance (see section 4.3.1).

In the initial paper [GMS99] of the GPS model, an analytical formula for the skeleton density is obtained by inserting eq. (4.77) and eq. (4.64) into the solid mass balance. In subsequent papers with a more involved dehydration formulation, only numerical evaluation of the solid mass balance is available to compute the skeleton density.

4.4.6. Thermal properties

The effective heat capacity is taken as a weighted sum of the specific heat capacities of the individual components,

$$(\rho C_p)_{\text{eff}} = m_s C_p^s + m_w C_p^w + m_v C_p^v + m_a C_p^a. \tag{4.78}$$

In the Tenchev model, the specific heat capacity of the skeleton is a polynomial in temperature,

$$C_p^s = C_{p0}^s + 80\,\text{J kg}^{-1}\,\text{K}^{-1}\left(\frac{T - T_{\text{ref}}}{120\,\text{K}}\right) - 4\,\text{J kg}^{-1}\,\text{K}^{-1}\left(\frac{T - T_{\text{ref}}}{120\,\text{K}}\right)^2, \tag{4.79}$$

with a value $900\,\text{J kg}^{-1}\,\text{K}^{-1}$ for C_{p0}. The GPS model uses a linear relation,

$$C_p^s = C_{p0}^s(1 + A_c(T - T_{\text{ref}})), \tag{4.80}$$

with a value of $C_{p0}^s = 940\,\text{J kg}^{-1}\,\text{K}^{-1}$ given for an example concrete. Unfortunately, no value for A_c is given.

The effective thermal conductivity is given in the GPS model as

$$\lambda_{\text{eff}} = \lambda_d(T)\left(1 + \frac{4\rho_w S_w}{(1-n)\rho_s}\right), \tag{4.81}$$

where λ_d is the conductivity of dry concrete. It is given as a linear function of temperature,

$$\lambda_d = \lambda_{d0}\left(1 + A_\lambda(T - T_{\text{ref}})\right). \tag{4.82}$$

In [GMS99], values of $\lambda_{\text{do}} = 1.67\,\text{W m}^{-1}\,\text{K}^{-1}$ and $A_\lambda = 5 \times 10^{-5}\,\text{K}^{-1}$ are given.

The conductivity is also given as a quadratic function in the Tenchev model,

$$\lambda_{\text{eff}} = 2.0\,\text{W m}^{-1}\,\text{K}^{-1} - 0.24\,\text{W m}^{-1}\,\text{K}^{-1}\left(\frac{T - T_{\text{ref}}}{120\,\text{K}}\right) + 0.012\,\text{W m}^{-1}\,\text{K}^{-1}\left(\frac{T - T_{\text{ref}}}{120\,\text{K}}\right)^2. \tag{4.83}$$

This formulation lacks any dependence on the pore water saturation, which is in conflict with the GPS model (where concrete in fully saturated condition has a conductivity 2.5 times higher than dry concrete) and experimental data [BK96].

4.5. Boundary conditions

The boundary conditions for the problem can be of the usual types. The Dirichlet conditions depend on the choice of independent variable. For the set $\{p_a, p_v, T\}$, they may be written as

$$p_a = p_{\text{a},\infty} \quad \text{on } \Gamma_D^a, \tag{4.84}$$

$$p_v = p_{\text{v},\infty} \quad \text{on } \Gamma_D^w, \tag{4.85}$$

$$T = T_\infty \quad \text{on } \Gamma_D^T, \tag{4.86}$$

where the subscript $_\infty$ indicates ambient values of these variables.

The Neumann boundary conditions for the air and water mass balance, as well as the enthalpy balance, relate the value of the normal derivative to a prescribed flux,

$$-(\rho_a \mathbf{v}_g - \rho_g \mathbf{v}_v^d) \cdot \mathbf{n} = q_a \quad \text{on } \Gamma_N^a, \tag{4.87}$$

$$-(\rho_v \mathbf{v}_g + \rho_w \mathbf{v}_w + \rho_g \mathbf{v}_v^d) \cdot \mathbf{n} = q_v + q_w \quad \text{on } \Gamma_N^w, \tag{4.88}$$

$$-(\rho_w \mathbf{v}_w \Delta H_{\text{phase}} - \lambda_{\text{eff}} \nabla T) \cdot \mathbf{n} = q_T \quad \text{on } \Gamma_N^T, \tag{4.89}$$

where q_a, q_v, q_w, q_T are the normals of the dry air flux, vapour flux, liquid water flux and heat flux, respectively.

The last type of boundary condition is the Robin boundary condition. Here, a weighted average of the unknown and the normal derivative are prescribed. For our problem, they are

$$(\rho_v \mathbf{v}_g + \rho_w \mathbf{v}_w + \rho_g \mathbf{v}_v^d) \cdot \mathbf{n} = \beta_c(\rho_v - \rho_{\text{v},\infty}) \quad \text{on } \Gamma_R^w, \tag{4.90}$$

$$(\rho_w \mathbf{v}_w \Delta H_{\text{phase}} - \lambda_{\text{eff}} \nabla T) \cdot \mathbf{n} = \alpha_c(T - T_\infty) + e\sigma_0(T^4 - T_\infty^4) \quad \text{on } \Gamma_R^T, \tag{4.91}$$

for the water mass balance and enthalpy balance, respectively. The parameters are the water transfer coefficent β_c, the convective heat transfer coefficient α_c, the surface emissivity e and the Stefan-Boltzmann constant σ.

4.6. Choice of independent variables

The selection of appropriate independent variables can aide or hinder the modeling and numerical solution of the equations discussed above. Several criteria for this choice are available. Ideally, the physical variable should be easy to measure to ease validation. Together, the chosen set should provide a unique description of the thermodynamic state of the system for the entire range of possible states. This includes temperatures above and below the critical point of water, as well as low and high liquid water saturation of the pores. Numerically, a good performance of the resulting code is desirable. Additionally, the prescription of boundary and initial conditions is highly dependent on this choice.

Temperature and displacement (for models with a mechanical component) are chosen by all described models. For the hygrometric variable, several possibilities exist: volumetric or mass moisture content, vapour pressure, relative humidity or capillary pressure.

The Tenchev model uses gas pressure and mass vapour content as the additional independent variables, for a complete set of $\{T, p_g, m_v\}$. The authors claim to have repeated the analysis for $\{T, p_a, p_v\}$ and $\{T, m_a, m_v\}$ with almost identical results [TLP01].

For GPS model, gas and capillary pressure were chosen as the additional independent variables. It has to be noted that the capillary pressure has no physical meaning beyond the critical point and below the solid saturation point, since no liquid water exists there. In such situations, the authors reinterpret the meaning of the capillary pressure [GPS02].

The basis for this reinterpretation is the water potential,

$$\Psi_c = \frac{RT}{M_w} \ln\left(\frac{p_v}{f_{\text{vs}}}\right), \tag{4.92}$$

where f_{vs} is the fugacity of water vapour in thermodynamic equilibrium with a saturated film with adsorbed water. Below the critical point, this should be substituted by the saturation vapour pressure p_{vs}. In combination with the Kelvin equation,

$$\ln\left(\frac{p_v}{p_{vs}}\right) = -\frac{p_c}{\rho_w}\frac{M_w}{RT}, \tag{4.93}$$

it becomes possible to treat the capillary pressure as a substitute for the water potential, according to [GPS03],

$$p_c = -\Psi_c \rho_w. \tag{4.94}$$

This means that capillary pressure can be used in the low moisture range, where capillary water is not present. Yet in such a state, the values cannot be interpreted as pressures in their conventional sense, nor should they be used in the equivalent stress principle. In support of this elaborate approach, the authors claim good numerical performance. They presume that the avoidance of capillary pressure as the state variable was due to theoretical inconsistencies of its definition at the macro-scale. These problems have been resolved [GPS03].

Each choice is subject to criticism. According to [GPS03], the choice of mass or volumetric moisture content, while "the most natural choice", is not well suited for numerical use in low and high saturation conditions. Additionally, it is discontinuous at material interfaces and does not link directly to the resulting stresses.

Davie *et al.* argue that vapour content is valid at all temperatures and in dry conditions without requiring such manipulation [DPB10]. Only under full saturation with liquid water is the vapour content no longer physically meaningful. The authors note, however, that this argument applies equally to the other variable, gas pressure, used in the GPS model.

Baydoun *et al.* use dry air and vapour pressure as additional degrees of freedom, essentially one of the alternatives tried in [TLP01]. According to the authors, capillary pressure (which was used by Gawin *et al.*) is a poor choice, particularly "when a filling phase partially disappears in a subdomain", as is the case with the gas phase inside the so-called moisture clog. The choice of dry air pressure and vapour pressure allows them to control the finite element solution to be non-negative at all times, even when the gas phase disappears due to full saturation.

4.7. Numerical approximation

The set of balance eqs. (4.10), (4.12), (4.18) and (4.26) is solved via the finite element method. When solving only the air mass balance, water mass balance and enthalpy balance, the set of independent variables can be chosen based on the discussion above. In the case where, additionally, the skeleton mass balance is solved for, the porosity n enters as an additional independent variable. For the rest of this section, the set of independent variables is assumed to be $\{p_v, p_a, T, n\}$.

The domain is discretized with mixed elements, with a Lagrange element for each component. The vector of degrees of freedom of the unknowns can be written as

$$\mathbf{u} = \begin{bmatrix} \mathbf{p_v} \\ \mathbf{p_a} \\ \mathbf{T} \\ \mathbf{n} \end{bmatrix}. \tag{4.95}$$

The polynomial order is the same for all subelements, and linear elements were found to suffice. Increasing the order or choosing different orders for the individual components is trivial due to the implementation in FEniCS [ABH+15] (see appendix A for details). Since the test function w is from the same function space, it can also be split into its components w_π.

To discretize eqs. (4.10), (4.12), (4.18) and (4.26), they are transformed into their weak forms. The residual for the dry air mass balance is

$$r_a = \int_\Omega w_a \frac{\partial m_a}{\partial t} \, \mathrm{d}x - \int_\Omega \nabla w_a \cdot J_a \, \mathrm{d}x, \tag{4.96}$$

where J_a is the dry air flux from eq. (4.15). The water mass balance reads

$$r_w = \int_\Omega w_w \frac{\partial (m_v + m_w)}{\partial t} \, \mathrm{d}x - \int_\Omega \nabla w_w \cdot (J_v + J_w) \, \mathrm{d}x + \int_\Omega w_w \dot{m}_{\mathrm{dehydr}} \, \mathrm{d}x, \tag{4.97}$$

with the vapour flux J_v and the liquid water flux givn in eqs. (4.21) and (4.22), respectively. The skeleton mass balance residual is

$$r_s = \int_\Omega w_s \frac{\partial m_s}{\partial t} \, \mathrm{d}x - \int_\Omega w_s \dot{m}_{\mathrm{dehydr}} \, \mathrm{d}x. \tag{4.98}$$

Lastly, the residual for the enthalpy balance,

$$\begin{aligned} r_T = &\int_\Omega w_T \, (\rho C_p)_{\mathrm{eff}} \frac{\partial T}{\partial t} \, \mathrm{d}x + \int_\Omega w_T \left(\rho_w C_{\mathrm{pw}} \mathbf{v}_w + \rho_g C_{\mathrm{pg}} \mathbf{v}_g \right) \cdot \nabla T \, \mathrm{d}x + \int_\Omega \nabla w_T \cdot (\lambda_{\mathrm{eff}} \nabla T) \, \mathrm{d}x \\ &+ \int_\Omega w_T \, \dot{m}_{\mathrm{vap}} \Delta H_{\mathrm{vap}} \, \mathrm{d}x + \int_\Omega w_T \, \dot{m}_{\mathrm{dehydr}} \Delta H_{\mathrm{dehydr}} \, \mathrm{d}x. \end{aligned} \tag{4.99}$$

Since the dehydration is assumed to be an irreversible process, the dehydration degree is an internal variable that only depends on the maximum temperature at each material point,

$$\Gamma(t) = \Gamma(T_{\max}(t)). \tag{4.100}$$

Discretization in time is done by applying the Rothe method, resulting in a nonlinear set of equations

$$\mathbf{r}(\mathbf{u}^{n+1}, \mathbf{u}^n) = \begin{pmatrix} r_w \left(\mathbf{u}^{n+1}, \mathbf{u}^n \right) \\ r_a \left(\mathbf{u}^{n+1}, \mathbf{u}^n \right) \\ r_T \left(\mathbf{u}^{n+1}, \mathbf{u}^n \right) \\ r_s \left(\mathbf{u}^{n+1}, \mathbf{u}^n \right) \end{pmatrix} = \mathbf{0}. \tag{4.101}$$

The time integration is performed using an Euler backward method with adaptive time stepping.

4.8. Discussion

Both approaches provide a coupled thermal-hygral-mechanical model for numeric evaluation of concrete behaviour at high temperatures. The balance laws employed, as well as their general form, are similar in both models. Advection, diffusion, dehydration, conductive and convective heat transport, and evaporation are considered in all discussed papers. In the GPS model and the modified Tenchev model, the effects of mechanical damage, capillary pressure and adsorbed water diffusion are additionally covered.

There are two areas of major differences between the models: the choice of independent variables and the formulations of constitutive relationships. The GPS model chooses an elaborate approach to avoid using vapour pressure, because vapour pressure is physically meaningless in conditions of pores fully saturated with liquid water. While this reservation is in general valid, the questions if such states are actually reached remains. The apparent advantages of using capillary pressure do not justify the additional implementation costs and needed care when interpreting results. Furthermore, capillary pressure is not easily measured, if at all. For the prescription of initial and boundary conditions, either option is workable. The choice of vapour mass content, employed in the Tenchev model, is much easier to handle and implement. Not being able to simulate states fully saturated with liquid water seems like the smaller cost compared to the complications of the GPS approach.

The constitutive equations employed by the two models often differ significantly. In general, the equations employed by the Tenchev model are simpler than the ones from the GPS model. This has both advantages and disadvantages.

The identification of parameters by experiment is much easier for simpler formulations, as is the interpretation of a given set of material parameters. Correspondingly, the model is kept manageable and no important information is easily forgotten. In contrast, the GPS model often has so many parameters and terms, that the authors themselves lose track. For example, in [GPSiia], they claim “for the first time all the constitutive relationships of the model are summarized and discussed in detail”, yet the diffusion description is not given in this paper. Numerous times numerical values for parameters are missing. This is not a problem for practical application, because those need to be calibrated for the concrete under consideration anyway. But it is a problem for reproducibility—unless all values are given, one cannot make a valid comparison of ones own implementation of the same model to the description in the papers. Verifying the authors claims, for example on numerical performance, becomes impossible.

At the same time, the approaches often need a certain complexity to resolve the numerous physical phenomena occurring in this problem. For example, the effective thermal conductivity in the Tenchev model is independent from the water content in the pores, contradicting intuition and experimental evidence.

When coding your own implementation, you are not restricted to follow either model to the letter. Individual constitutive equations can be chosen from either model and used in conjunction with those from the other.

In conclusion, the GPS model is too complicated for practical applications, not least because it is difficult to calibrate the material parameters needed. The Tenchev model is far clearer, and in the modified version incorporates all the major physical phenomena.

5. Results

5.1. Skeleton mass density

Porosity and dehydration evolution are dependent processes, see eq. (4.10). Their evolution influences air, water and heat transfer, and their interdependence should not be neglected as in the previous models under discussion, see section 4.2. As a result, the skeleton mass density is often treated inconsistently. It could be argued that the skeleton mass density changes in such a way as to fulfill the mass balance for two independently chosen descriptions of the porosity and dehydration. However, all models assume it to be constant when it enters into other equations, such as the formulation for the heat capacity.

Given the skeleton mass balance and a pair of dehydration and porosity models, one can solve the balance equation for a material point to obtain the skeleton mass density. To do so, the skeleton mass balance $\frac{\partial m_s}{\partial t} = \dot{m}_{\text{dehydr}}$ can be rearranged into an ODE for the skeleton mass density

$$\frac{\mathrm{d}\rho_s}{\mathrm{d}T} = \frac{1}{1-n}\left(\frac{\mathrm{d}m_{\text{dehydr}}}{\mathrm{d}T} + \rho_s \frac{\mathrm{d}n}{\mathrm{d}T}\right). \tag{5.1}$$

This gives the theoretical evolution of that density such that the skeleton mass balance is maintained and can be seen for all the models under discussion in fig. 5.1.

The resulting values are higher than one would expect. Dry cement mixed with dry aggregates would result in a density of about $2700\,\mathrm{kg\,m^{-3}}$. By hydration and curing, and then further dehydration by heating, no increase in skeleton density is possible. This demonstrates the problematic consequences of independently choosing porosity and dehydration descriptions.

Solving the skeleton mass balance directly links the dehydration and porosity evolution. The skeleton density is assumed to be constant. The additional balance equation allows for one fewer constitutive equation, thereby either saving on experimental effort or providing additional data for validation. If the dehydration description solely depends on temperature, the balance equation becomes an ODE that could be solved separately. Discretizing the skeleton mass balance along with the other balance equations allows for more complex dehydration descriptions, depending not only on temperature, but also on for example liquid water content or pore pressure.

5.2. Validation on a slowly heated cylinder

The data for validation have been obtained from an X-ray computer tomography (CT) scan of a concrete sample at various times during heating, published in [PSO+18]. The use of CT allows a spatially continuous measurement of the water content inside the specimen.

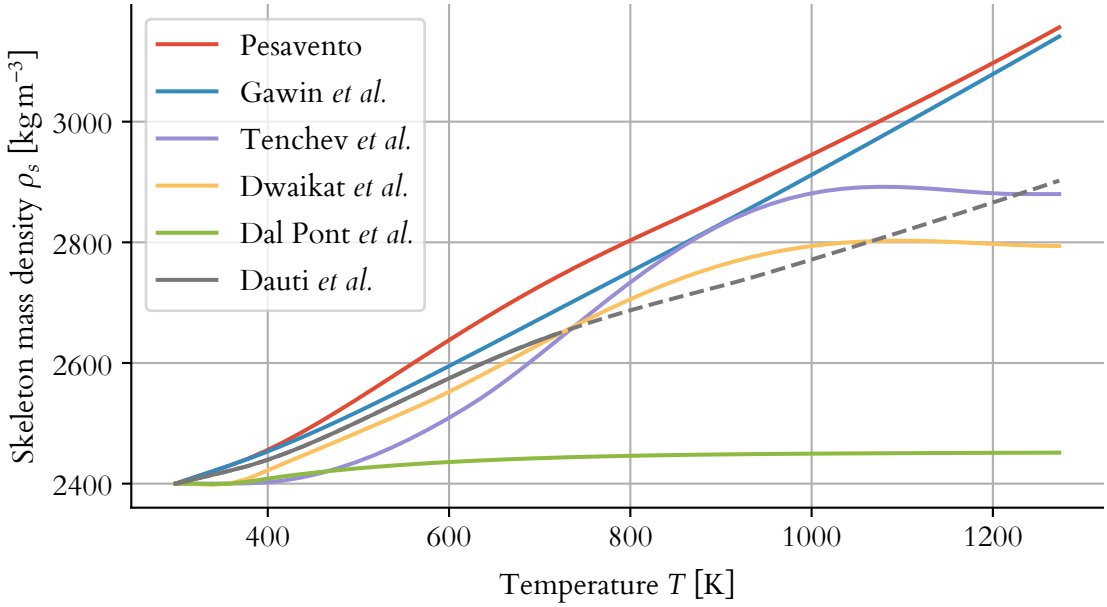

Figure 5.1.: Theoretical skeleton mass density for given combinations of dehydration and porosity models

Table 5.1.: Mixture of the high-strength concrete [PSO+18].

Component	Content [kg m^{-3}]
Cement CEM I 42.5 R	580
Water	173
Quarzitic aggregate	
0/2 mm	764
2/4 mm	229
4/8 mm	535
Silica fume	63.8
Superplasticizer	14.5

A cylindrical specimen (⌀40 mm × 100 mm) of high-strength concrete was surrounded by a glass-ceramic shell and then wrapped in aluminium-silicate wool to hinder exchange of moisture and heat along the lateral boundary. The mix of the concrete can be seen in table 5.1. The specimens were stored under water for 28 days after casting. At the time of measurement they were at least 90 days old, having been stored in a climate chamber of 20 °C and 65 % relative humidity between water storage and heating. Heating was applied using an electric heating element at the top surface, with a heating rate of 10 K min^{-1} for the first 28 min up to a maximum temperature of 300 °C. This temperature was then kept constant for another 130 min.

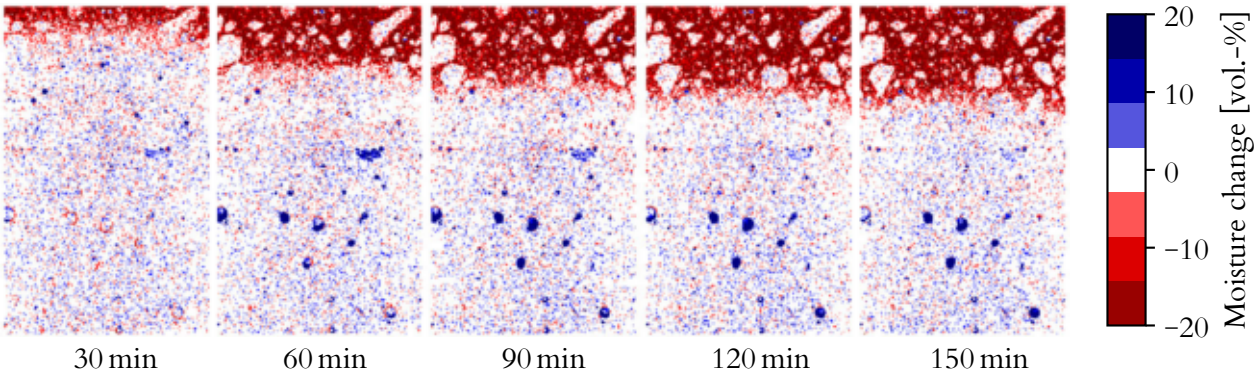

Figure 5.2.: Change is moisture during the heating process. An advancing drying front (in red), as well as the filling of macropores (in blue) in the lower part of the specimen, can be seen. Image from [PSO+18].

The specimen was placed on a spinning table to take multiple images from different angles, and then reconstruct a 3D volume representation from the projections. Taking a single image took roughly one second, and a full scan was comprised of 650 projections, resulting in about 10 minutes per scan. As a consequence, the values at the given times are averaged values of 10 minutes around this point in time. The CT scans result in grayscale images where the luminance corresponds to the density of the material. The difference in brightness between empty and fully saturated pores was taken to represent 100 % moisture change. The moisture change can thus be quantified by the change in brightness between the initial image before heating and subsequent images during heating. Deformation was corrected for using digital volume correlation. Since embedded temperature sensors would introduce artifacts into the X-ray images, separate experiments with embedded thermocouples were performed to find the temperature distribution. The top 5 mm of the images were removed, because they exhibit cone-beam artifacts rather than actual material behaviour. Further details of the experimental setup and image correction can be found in [PSO+18]. The images from the CT clearly show the change in moisture as the drying front advances into the material, see fig. 5.2. Averaging over the width of the diameter gives a one-dimensional moisture distribution, which will be used for comparison to the finite element model.

The initial conditions are given as a constant vapour pressure corresponding to a relative humidity of 65 %, a dry air pressure of ambient air pressure (101.325 kPa) minus the vapour pressure, a temperature of 295 K and an initial porosity of 7.2455 % as in [PSO+18]. Inhomogeneous initial moisture conditions due to drying during storage were initially considered, but found to be of little influence. The material parameters used in the simulation can be seen in table 5.2.

Additionally, the temperature has been measured with four temperature gauges along the axial direction. A comparison of these results with the simulation can be seen in fig. 5.3.

For comparison to the CT data, the change in moisture content is computed by

$$\Delta m_m = m_w - m_w^0 + m_v - m_v^0 + m_{\text{dehydr}}^{max}(\Gamma - 1), \tag{5.2}$$

Table 5.2.: Material parameters used in the simulation

Parameter	Value	Unit	Parameter	Value	Unit
k_0	2.884×10^{-21}	m^2	λ^0_{dry}	4.282	$W\,m^{-1}\,K^{-1}$
A_k	0.005	K^{-1}	A_λ	−0.002 108	K^{-1}
D	1.319×10^{-6}	$m^2\,s^{-1}$	ΔH_{dehydr}	2400	$kJ\,kg^{-1}$
a	52.691	kPa	h	238.1	$W\,m^{-2}\,K^{-1}$
b	1.778	—	ε	1	—
C^s_{p0}	1200	$J\,kg^{-1}\,K^{-1}$	β_c	0.2	$m\,s^{-1}$

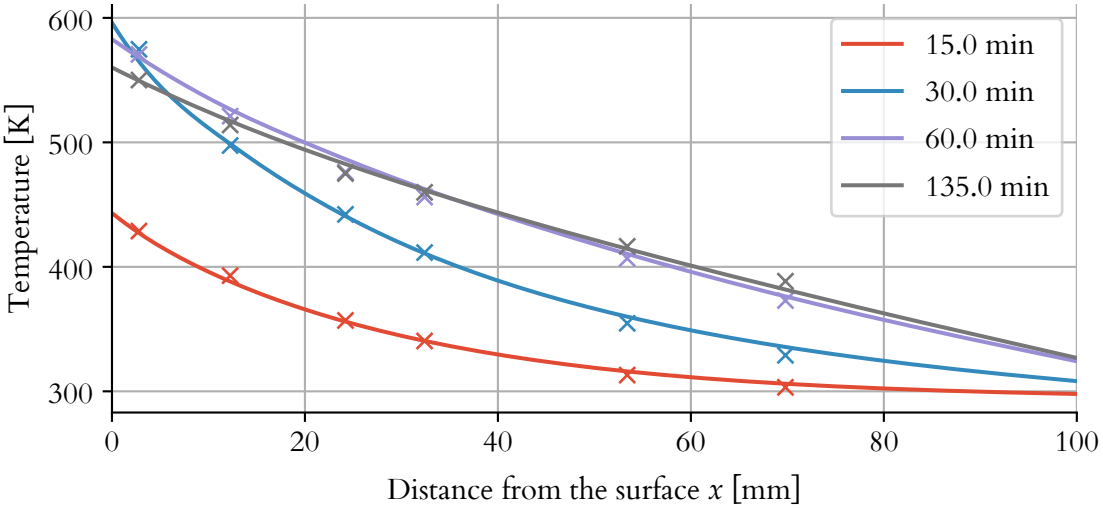

Figure 5.3.: Comparison of temperature evolution between experiment (crosses) and numerical model (lines).

where m^{max}_{dehydr} is the maximally dehydrated water mass when the dehydration degree Γ reaches one. The model shows good agreement as illustrated in fig. 5.4. Particularly for the early part (15 min and 30 min) and towards the end of the experiment (135 min), the location of the drying front of the simulation coincides with the experimental results. For the times in between (45 min, 60 min and 90 min) the model predicts a slightly more advanced front than can be observed in the experiments. The moisture accumulation behind the drying front, that is the moisture clog, is slightly overestimated at 30 min, and slightly underestimated for later times. The steep gradient of the moisture content is captured well. In the colder interior of the specimen, an increase in moisture content can be seen in the CT data. This broader accumulation of moisture is not present in the model results. There are two possible causes for this. Firstly, the dehydration description based on eq. (4.73) releases basically no water below 200 °C (the temperature range of this region), which leads to an underestimation of the available water. Secondly, the analysis and postprocessing to get from CT brightness changes to water mass loss may introduce a systematic error as the experiment goes on.

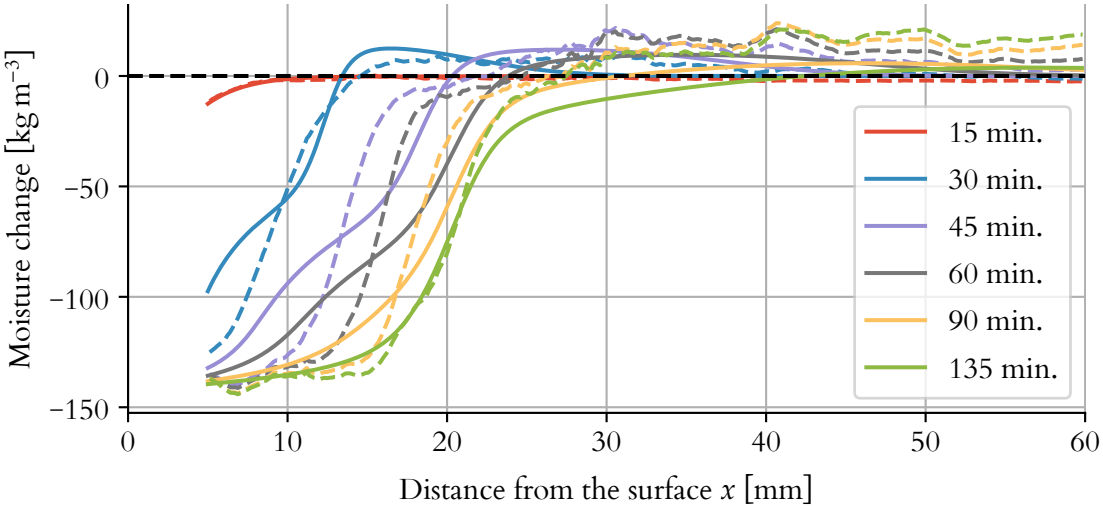

Figure 5.4.: Comparison of water loss between CT data (dashed lines) and numerical model (solid lines).

The simulation allows for further insight into the state of water inside the pores, as well as the evolution of the solid phase. In fig. 5.5, the saturation reaches almost zero on the exposed surface, with a steep gradient, especially for the first 45 min. The moisture clog shows up again here. The maxima in saturation and gas pressure occur at the same time, yet not at the same locations. The maxima of the gas pressure are in front of the highest water accumulation, with values exceeding 30 MPa. For mechanical loads on the skeleton, the pore pressure is the relevant quantity, which is a purely postprocessed quantity given by

$$p_{\text{pore}} = S_w p_w + (1 - S_w) p_g - p_{g,\infty}. \tag{5.3}$$

Due to the slow heating and comparatively low temperatures, the maximum pore pressure is about 5 MPa. The water pressure shows very large negative values in the dry regions of the specimen, but due to the low saturation there, the resulting influence on the pore pressure remains in the order of that of the gas pressure. As a result, the pore pressure remains mostly negative, since the capillary effect of the liquid water is larger than the increase in gas pressure. The porosity exhibits an almost step-like evolution due to the similarly steep dehydration formulation. After 60 min, it no longer changes since the temperature doesn't rise any further.

Of particular interest for this work is the choice of dehydration formulation. As mentioned in section 4.4.5, dehydration conditions for TGA will differ significantly from those in a specimen for spalling tests. The models have all been recalibrated to the TGA data for this particular concrete. This was done using a nonlinear least squares method. The result of the calibration can be seen in fig. 5.6, and the parameters are shown in appendix B.

The simulation was repeated for each of the dehydration models that have been presented. The change in moisture mass shows significant differences between the models, see fig. 5.7. In particular, none of the models based on TGA exhibit enough dehydration during the early heating phase to match the experimental results. The dehydration description from Tenchev

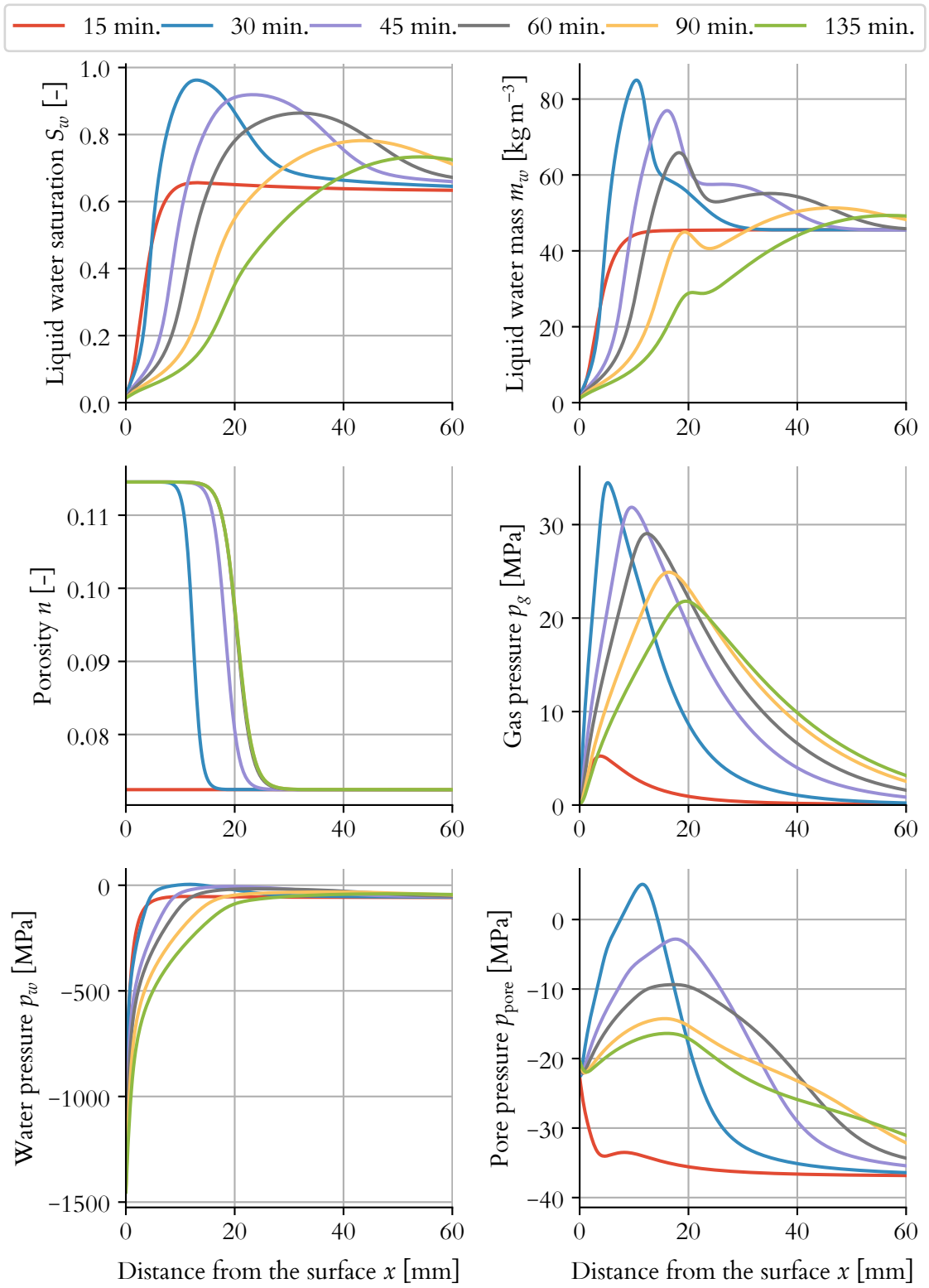

Figure 5.5.: Resulting saturation, gas pressure, liquid water mass, porosity, gas pressure, water pressure and pore pressure for each of the measurement times.

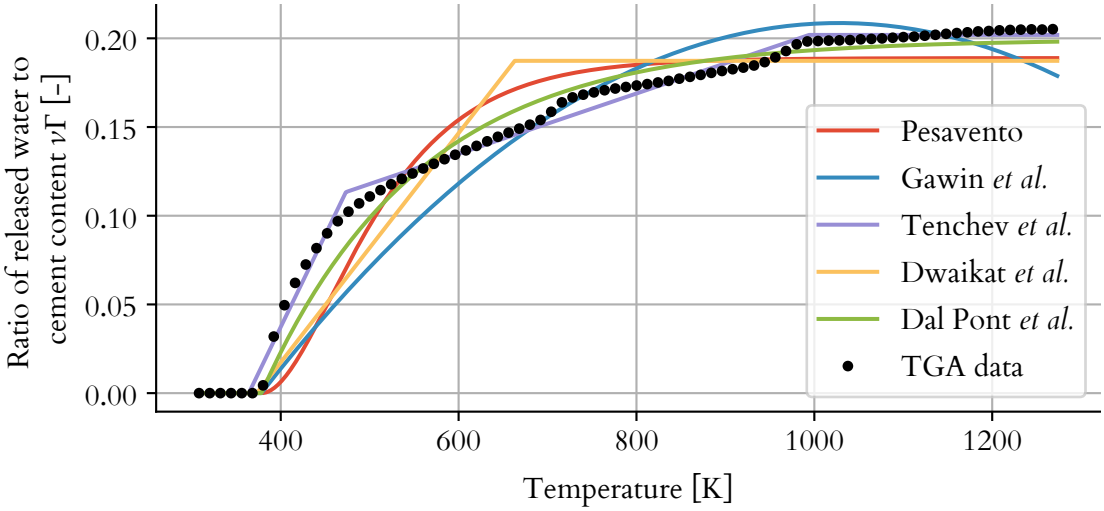

Figure 5.6.: Calibration of TGA-based models for the concrete of the specimen.

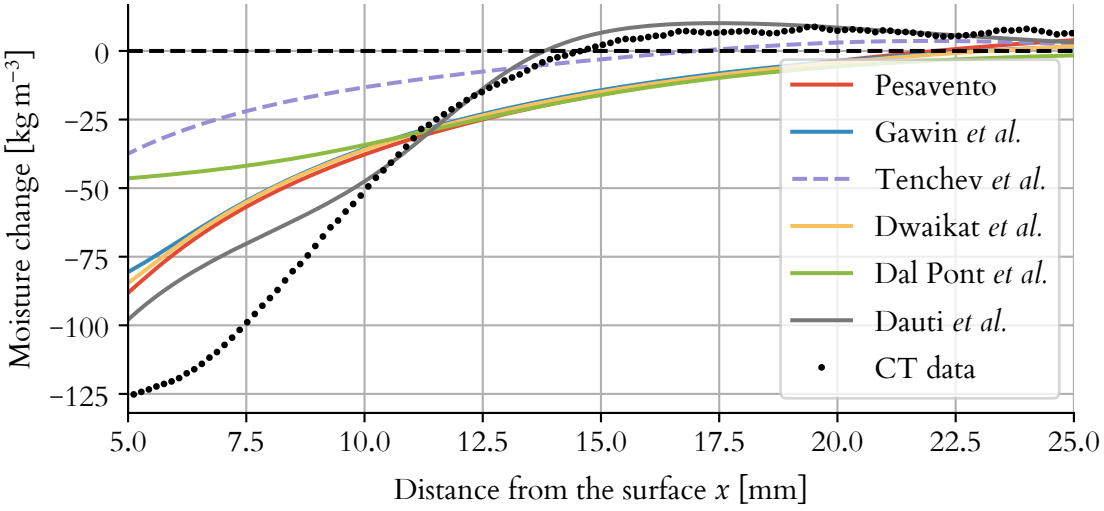

Figure 5.7.: Change in moisture mass after 30 minutes for each of the presented dehydration models. The black dots represent the CT data. The combination of the model with dehydration description by Tenchev did not converge to a solution beyond 21 minutes. The dashed line shows the results at that time.

et al. leads to a loss of convergence beyond 21 minutes. The values during the first 21 minutes of heating are shown for completeness.

Additional information can be extracted from the numerical solution that is not available via experiments. In particular, the composition of the moisture flux can be ascertained, the result of which can be seen in fig. 5.8 at one point in time. The liquid advection is the

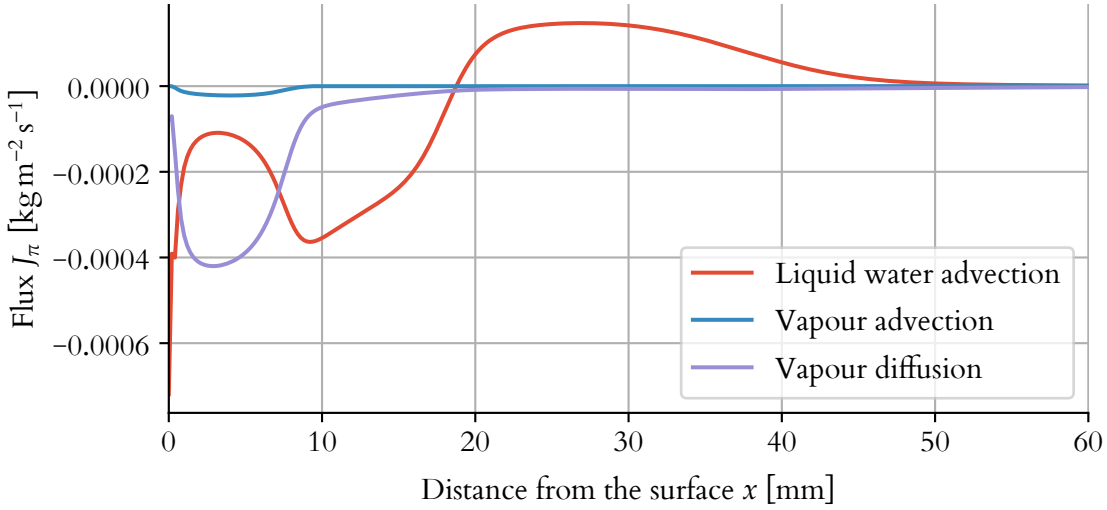

Figure 5.8.: Moisture flux components at $t = 45$ min.

predominant cause of moisture flow, with vapour advection being almost two orders of magnitude smaller at $x = 0$. The diffusive flux is visually indistinguishable from no flux at all.

To check the conservation of the moisture mass, the overall water mass in the specimen as well as the flux over the boundary have been computed. The values for constant timesteps can be seen in fig. 5.9. Differences between the two values indicate errors in the numerical method. They are particularly strong around the 20 min mark. For multiphase porous media flow, similar albeit smaller errors were reported in [TLP01; DPB06]. Tenchev *et al.* consider it to be a result of discrepancy between liquid water mass loss and water vapour mass gain during intense evaporation [TLP01]. Davie *et al.* additionally propose sudden gradients in the sorption isotherms to cause instantaneous imbalances of the water mass balance that rebalance over time, as well as difficulty reproducing the steep gradient of the drying front [DPB06]. Another possible cause is the lack of local mass conservation for continuous Galerkin methods [CD02], which could be resolved by switching to a discontinuous Galerkin approach.

5.3. High-temperature benchmark problem

While the CT data from the previous example enable direct validation of the moisture content inside the specimen, it is limited to temperatures of about 320 °C. To show that the proposed model also works beyond the critical point of water, and to allow comparison to other models, a common benchmark problem is presented here.

It was proposed by Tenchev *et al.* [TLP01], and also solved in [DPB06]. A cross-section of a concrete column exposed to fire is simulated. Symmetry in y-direction makes this a one-dimensional problem. The surface of the column is exposed to fire according to the ISO-834 fire curve

$$T = 293.15\,\mathrm{K} + 345\,\mathrm{K}\log\left(\frac{2t}{15\,\mathrm{s}} + 1\right) \tag{5.4}$$

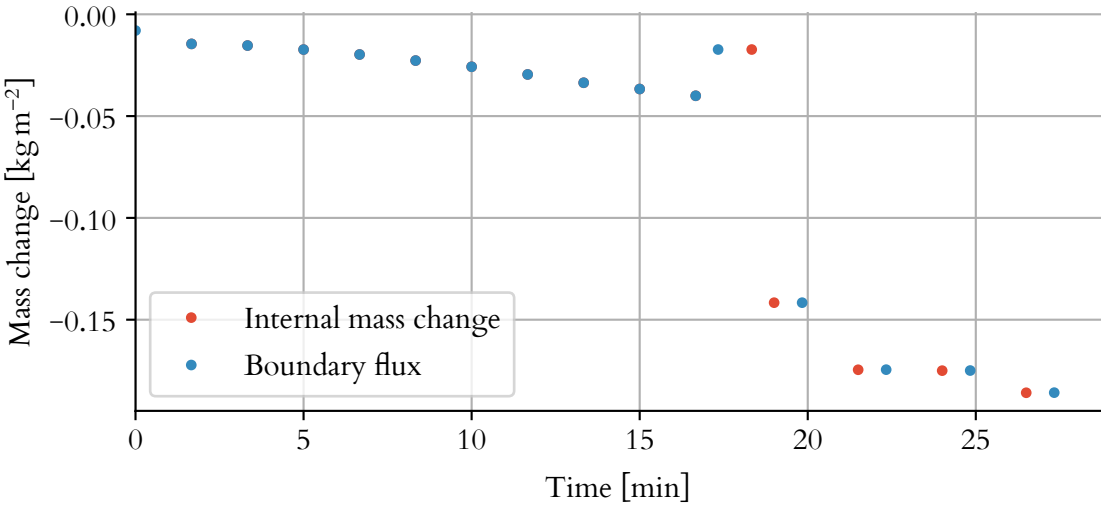

Figure 5.9.: Comparison of changes of water mass in the interior (red) and vapour flux along the boundary (blue).

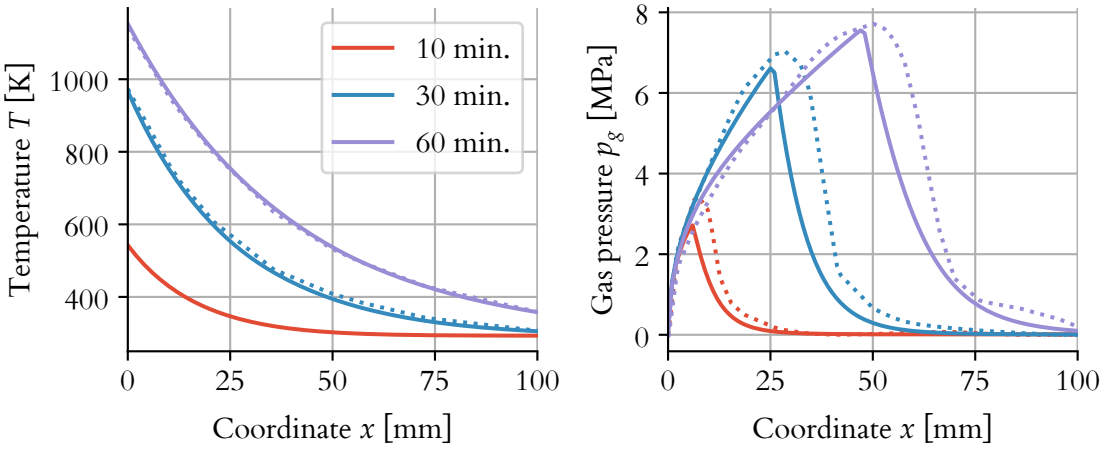

Figure 5.10.: Temperature and gas pressure distribution along the column section. The dotted lines show the results by Davie *et al.* [DPB06], whereas the solid lines are from the model under discussion.

for one hour. The outside atmosphere has a pressure of 0.1 MPa, and a relative humidity of 80 %. The initial conditions for the concrete are a temperature of 20 °C, a gas pressure of also 0.1 MPa and vapour pressure equal to the saturation pressure, i.e. a relative humidity of 100 %.

The resulting temperature and gas pressure distributions after 10 min, 30 min and 60 min can be seen in fig. 5.10. For the temperature distribution, a very close match is obtained. Temperature information at 10 min is not in the original paper. The gas pressure distribution appears to have a steeper decrease after the peak for the simulations presented here.

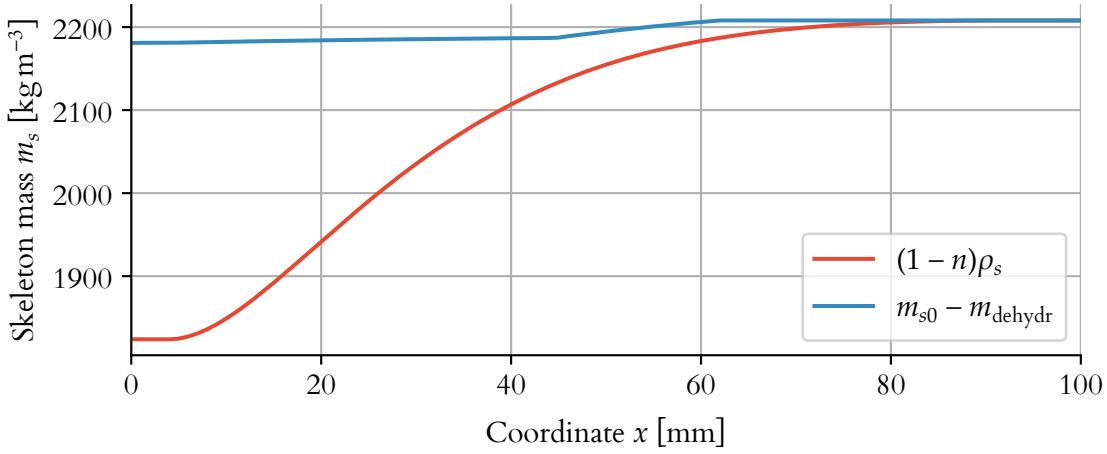

Figure 5.11.: Incompatible skeleton mass after 60 min of heating for model based on [DPB06].

In the paper that proposed this benchmark [TLP01], an equidistant timestepping scheme with a timestep size of 2 s was used. The subsequent paper by Davie *et al.* [DPB06] reduced it to 0.5 s. Both provided little justification for the specific choice of step size. Due to the highly nonlinear nature of the fire curve, an adaptive timestepping scheme can potentially save a significant amount of computing time. The criterion for increasing the time step is the number of Newton-Raphson iterations. If there are fewer than four iterations needed to solve the set of nonlinear equations, the new time step is set to 1.5 times the old time step. Consequently, much larger timesteps are used. Even with a conservative starting timestep of 5 s, the whole hour is integrated in just 87 timesteps, compared to 1800 or 7200 steps respectively. The mean timestep was 41.44 s, and the largest timestep was 85.43 s. To compute the error introduced by larger timesteps, a reference simulations with equidistant timesteps of 0.01 s was performed. Equidistant timestepping with a timestep of two seconds as in [TLP01] results in 0.0358, 0.0642 and 0.002 02 as the L_2 norm of the relative errors for p_v, p_a and T. In comparison, the adaptive scheme with the much larger timesteps also leads to larger errors, with 0.0506, 0.0927 and 0.003 06, again for p_v, p_a and T. For the largest error, that of p_a, using the adaptive scheme leads to an increase in the error of about three percentage points, while computational effort is reduced by a factor of about 20.

Solving the skeleton mass balance leads to a consistency between the porosity and dehydration evolutions. If they are chosen independently, as was the case with all the previous approaches, the results violate the skeleton mass balance. The change in skeleton mass consists of two terms, the change due to porosity change $\rho_s(n_0 - n)$, and the change due to dehydration m_{dehyd}. The incompatibility between the two terms can be seen in fig. 5.11.

The example shows that the model is able to cope with the transition beyond the critical point of water. Using an adaptive timestepping scheme can drastically reduce computation time. The introduction of the skeleton mass balance into the set of equations to be solved avoids incompatibility between dehydration and porosity descriptions.

6. Uncertainty quantification

6.1. Variability of concrete properties

There are two sources of uncertainty: variability of the material properties between specimen, and the accuracy and precision of the experimental measurements. Data on the variability of concrete is sparse. In most papers, only a single mean over the values from a few specimens is given. Without a coefficient of variation or a standard deviation, this is unusable for estimating the resulting uncertainty. Sometimes authors supply this basic statistical information, and most of this section will be based on such cases. Rarely are the actual values for all specimens given, mainly when there are only a handful of specimens. This is important information left out, since only giving mean and standard deviation can hide non-normal distributions. Furthermore, the precision of the measurement setup is often not disclosed. This makes it impossible to distinguish between measurement errors and specimen variability. In the following, the published data is used as a source for uncertainty without differentiating between the two. Publicly accessible raw data would be of great value, not only for uncertainty quantification, but is unfortunately very scarce.

As part of the French APPLET project, Aït-Mokhtar *et al.* published an extensive study on the variability of concrete in 2013 [ABB+13]. Specimens of three different concrete mixes were sent to seven different laboratories as part of larger project to quantify the variability of concrete properties. The concrete mixes for these tests came from two different construction sites, denoted with A1 and A2. At site A1, forty batches of the concrete were made, denoted by A1-1 through A1-40. At site A2, two different concrete mixes were used, with twenty batches each, denoted by A2-1-1 through A2-1-20, and A2-2-21 through A2-2-40, respectively. In this study, the variability of compressive and tensile strength, chloride migration coefficient, water sorption isotherms, carbonation depths, electrical resistivity, porosity, degradation tests in leaching tests and permeability was investigated. The results for the parameters that are relevant to the thermo-hygral model will be reviewed.

6.1.1. Porosity

Cylindrical specimens of ∅113 mm × 50 mm were used to determine the variability between batches. Additionally, smaller cylinders of ∅37 mm × 74 mm were cored from additional molded specimens of batches A1-13 and A2-1-1 to determine the variability within a given batch. There were 39 specimens from A1-13 and six specimens from A2-1-1.

Figure 6.1 shows the porosity distribution of the different batches. The porosity of A1 is lower than both A2 concretes. The mixes A1 and A2-1 have a higher variability than A2-2. Additionally, in both these cases a normal distribution is not a good fit for the data. Statistical information on these distributions is given in table 6.1

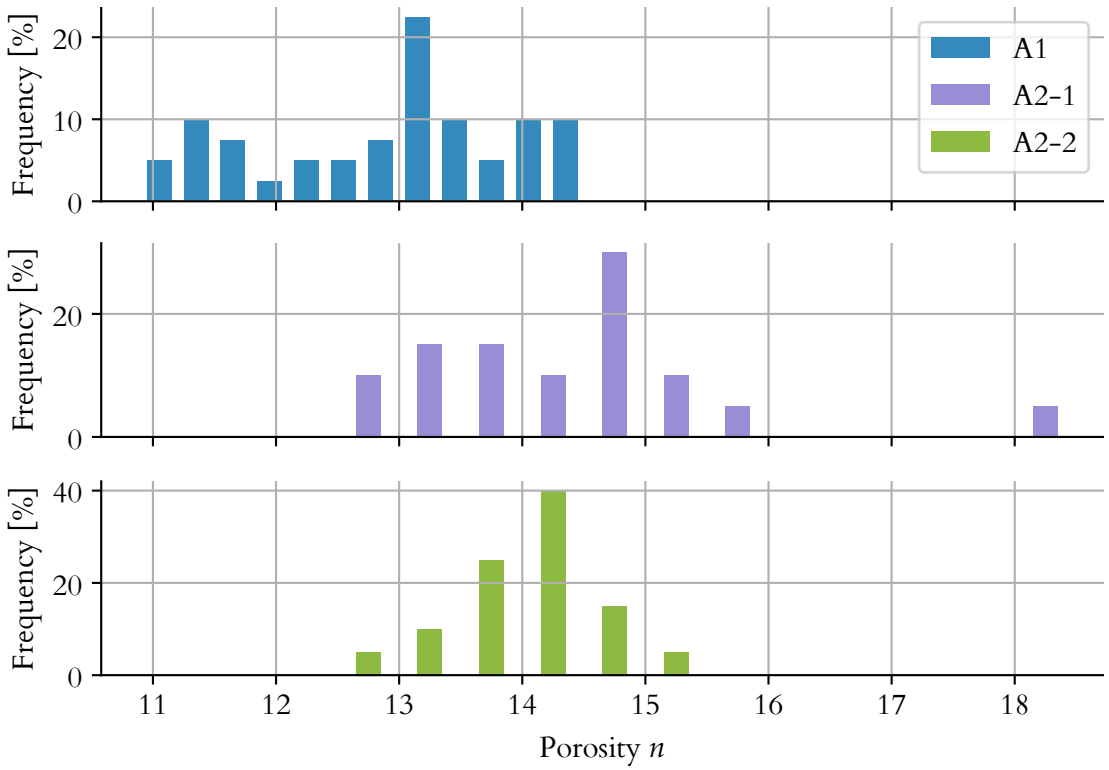

Figure 6.1.: Porosity distribution of the specimens of A1, A2-1 and A2-2, respectively. Data from [ABB+13].

The variation within one batch (A1-13), as well as the influence of drying temperature, can be seen in fig. 6.2. Higher drying temperatures lead to an increase in porosity, with the average increasing from 10.1 % at 60 °C to 11.5 % at 105 °C. The variability within the batch remains almost unaffected by temperature. Table 6.2 shows the statistical information of the porosity distributions of A1-13.

6.1.2. Permeability

For the permeability, only data from the first nine batches of construction site A1 is available. The larger specimens were cored, and nine cylindrical specimens of ∅40 mm × 60 mm were obtained from each larger specimen. Before coring, the larger specimens were stored under water for 11 months. After coring, the specimens are dried at 105 °C. The measurements were made using a Hassler cell, which is similar to the Cembureau device mentioned in section 2.2. Each specimen is placed under gas pressure, in this case nitrogen, and the resulting flow rate is measured. Three different pressures were used to estimate the permeability k, namely 0.15 MPa, 0.3 MPa and 0.6 MPa. The results can be seen in fig. 6.3. Overall, the permeabilities ranged from 2.4×10^{-17} m^2 to 9.8×10^{-17} m^2, with an average of 5.6×10^{-17} m^2. The standard deviation is 1.2×10^{-17} m^2, for a coefficient of variation of 22 %. Lastly, the variability

Table 6.1.: Statistical information of porosity data for different concrete mixes.

Concrete mix	A1	A2-1	A2-2
Average [%]	12.9	14.4	14.1
Standard deviation [%]	1.02	1.29	0.56
Coefficient of variation [%]	7.92	9.00	3.96
Minimum [%]	11.1	12.7	12.9
Maximum [%]	14.4	18.2	15

Table 6.2.: Statistical information of porosity data for different drying temperatures.

Drying temperature	60 °C	90 °C	105 °C
Average [%]	10.1	10.9	11.5
Standard deviation [%]	0.65	0.69	0.75
Coefficient of variation [%]	6.44	6.35	6.49
Minimum [%]	8.5	9.2	9.7
Maximum [%]	11.8	12.8	13.6

of the test method was also studied by measuring the same specimen ten times. This resulted in a standard deviation of 0.17×10^{-17} m^2, or a CoV of about 4 %.

6.1.3. Adsorption isotherms

Table 6.3.: Statistical information of the water content at different relative humidities. Data from [ABB+13].

Concrete	RH	12 %	33 %	53.5 %	75.5 %	90.4 %	100 %
A1	Mean [%]	0.2	0.8	1.9	2.8	3.2	4.3
	Std dev. [%]	0.09	0.13	0.27	0.27	0.26	0.33
	CoV [%]	45	16	14	10	8	8
A2-1	Mean [%]	0.2	1.0	2.6	3.6	3.9	4.9
	Std dev. [%]	0.08	0.17	0.18	0.31	0.35	0.39
	CoV [%]	40	17	7	9	9	8

The adsorption isotherms were measured by placing the specimens inside containers with a controlled relative humidity, and then weighing them to find the difference in adsorbed water, as described in section section 2.4. All specimens started out fully saturated, and were successively placed in relative humidities of 90.4 %, 75.5 %, 53.5 %, 33 %, 12 % and 3 %. That means only the desorption path was measured, and no information on the possible hysteresis is given. From site A1, three specimens were taken per batch, and from site A2, only mix A2-1 was examined, resulting in a total of 180 specimens. The cylindrical specimens

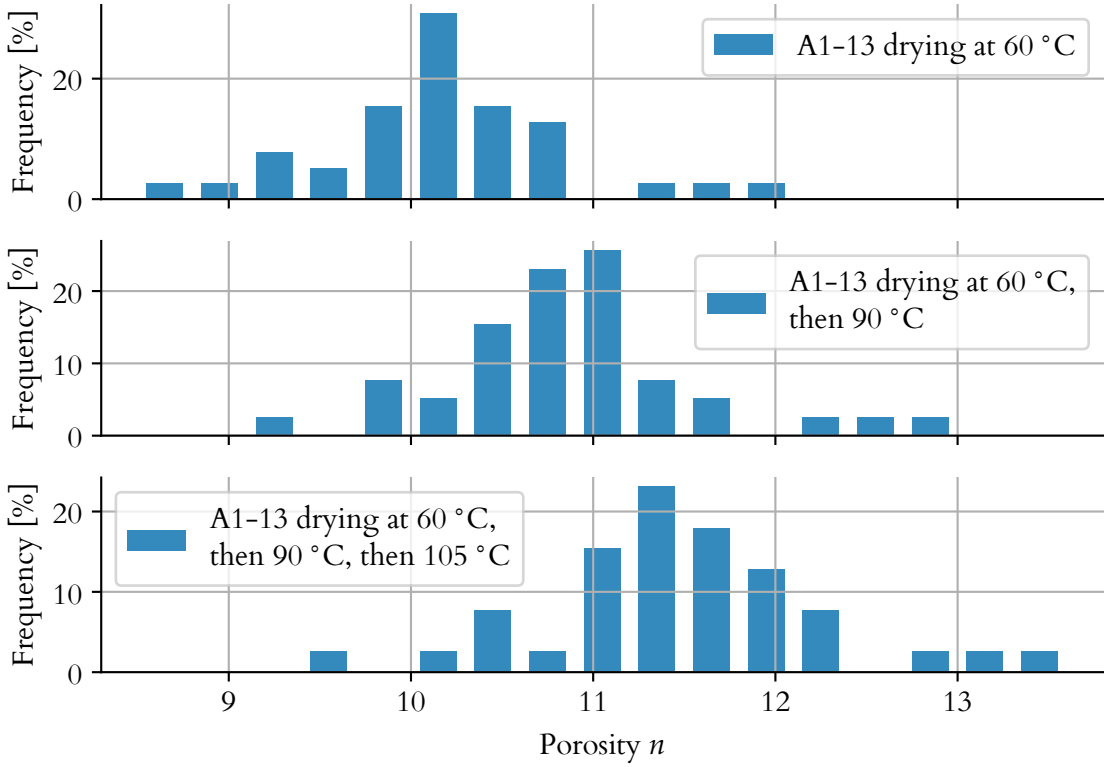

Figure 6.2.: Porosity distribution of the specimens from A1-13, dried at 60 °C, then 90 °C and ultimately 105 °C. Data from [ABB+13].

of ⌀40 mm × 60 mm were stored in under water for four months, starting one day after mixing. After three months, they were sawn into disks of (5.0 ± 0.5) mm. The weighing of the specimens was repeated daily until an equilibrium weight was reached. The criterion set for this is

$$\frac{m(t) - m(t + 24\,\mathrm{h})}{m(t + 24\,\mathrm{h})} \leqslant 0.005\,\%. \tag{6.1}$$

The results can be seen in fig. 6.4. According to the authors, the water content at each relative humidity value can be adequately modelled as normal distributions. The statistical information for these can be found in table 6.3.

The authors also noted that the large variability was due to changes in the material properties between different dates at the construction sites. Within one batch, the coefficient of variation is about 10 % for relative humidities at or above 33 %. At 12 % relative humidity, the coefficient of variation within a batch is about 12 %.

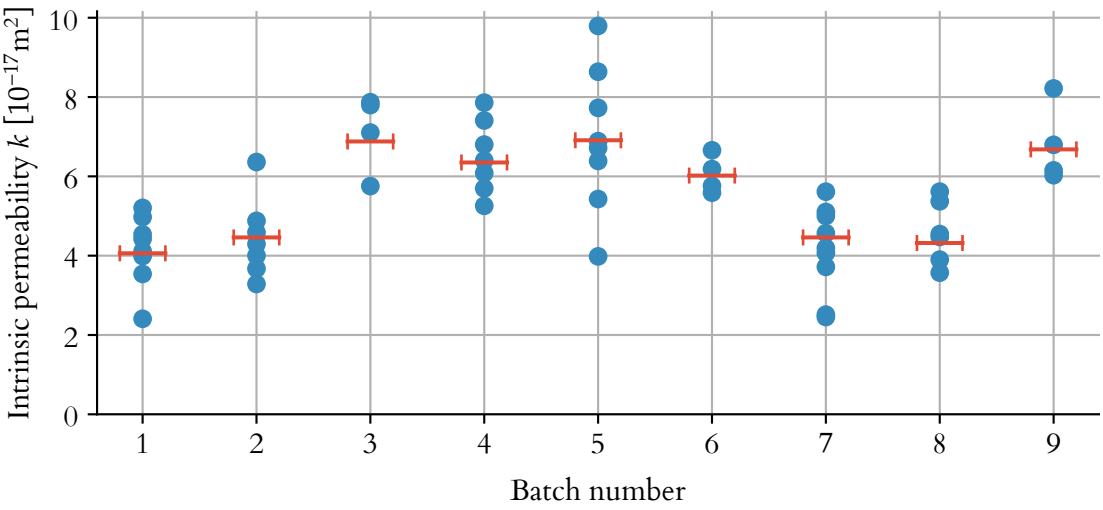

Figure 6.3.: Scatter of permeability values within a batch and between batches from construction site A1. The horizontal bars indicate the mean values. Data from [ABB+13].

6.2. Distribution selection

The model contains many different parameters that may vary, for example constitutive parameters or initial conditions. For a clearer presentation, the number of parameters is restricted to twelve, chosen to be of most interest here. They are:

- the dehydration parameters k and T_0 in eq. (4.73),
- the permeability parameters k_0 and A_T in eq. (4.36),
- the concrete density ρ,
- the initial dry thermal conductivity λ_{d0} eq. (4.82),
- the dry heat capacity C^s_{p0} in eqs. (4.79) and (4.80),
- the initial porosity n_0,
- the initial humidity $\frac{p_{v0}}{p_{\text{sat}}}$,
- the parameter a influencing the sorption isotherm in eq. (4.58),
- the dehydration enthalpy H_{dehydr},
- and the diffusivity of the concrete D.

For a uncertainty quantification, each parameter must be assigned a distribution. For the parameters k_0, A_T, n_0 and a, these will be based on the data in this section. Unfortunately,

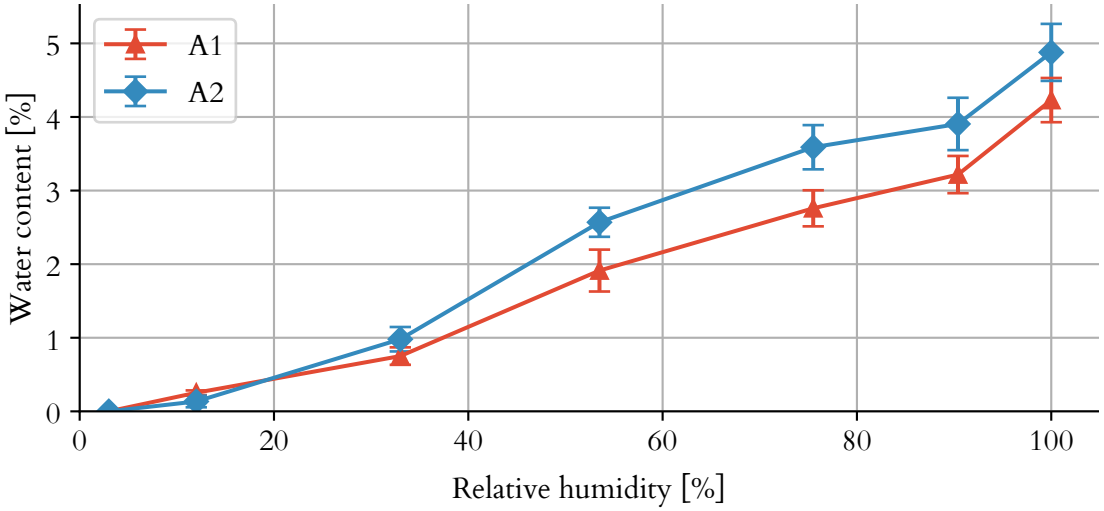

Figure 6.4.: Desorption isotherms for A1 and A2-1 concretes. Data from [ABB+13].

there is no information about the variability of the rest of the parameters available. A normal distribution with a coefficient of variation of 8 % is assumed in this case.

The variability of the parameters k_0, ρ, λ_{d0}, C^s_{p0}, n_0, H_{dehydr}, D and p_{v0}/p_{sat} directly corresponds to the variability of the experimental results. The parameters A_T and a, however, are only indirectly related to the measurements. In this case, a substitute variable that directly relates to the measurements is introduced and a distribution for the substitute is chosen. The samples from the substitute distribution will be converted to the actual model parameters via the following transformations.

For the temperature dependence of the permeability

$$A'_T = 10^{A_T(T-T_{\text{ref}})} \qquad \text{or} \qquad A_{\text{T}} = \frac{\log_{10} A'_{\text{T}}}{T - T_{\text{ref}}} \tag{6.2}$$

where T is chosen as 1200 K, the highest temperature that occurs in the example problems.

For the sorption isotherms, the parameter a is transformed as

$$a' = \left(\left(\frac{p_{\text{c}}}{a} \right)^{\frac{b}{b-1}} + 1 \right)^{-\frac{1}{b}} \qquad \text{or} \qquad a = p_{\text{c}} \left(a'^{-b} - 1 \right)^{\frac{1-b}{b}}, \tag{6.3}$$

where p_{c} is taken as the pressure where the pores are half saturated with liquid water for the given parameters a and b, that is $p_{\text{c}} = a \left(0.5^{-b} - 1\right)^{1-1/b}$.

The mean values for the distributions are the values from the forward model, that is the values for the cylindrical specimen from section 5.2 or the value for the column cross section from section 5.3, respectively. In the case of transformed variables, the value from the forward model is substituted into the transformation to obtain the mean of the transformed variable. An overview of all parameter distributions can be seen in table 6.4.

Table 6.4.: Distributions used in the uncertainty quantification. Parameters above the dividing line are based on data in this section, parameters below are assumptions.

Parameter	Distribution	CoV [%]
k_0	normal	22
A'_T (see eq. (6.2))	normal	22
n_0	normal	8
a (see eq. (6.3))	normal	14
k	normal	8
T_0	normal	8
ρ	normal	8
λ_{d0}	normal	8
H_{dehydr}	normal	8
C^s_{p0}	normal	8
p_{v0}/p_{sat}	normal	8
D	normal	8

6.3. Sensitivity analysis

The sensitivity of the parameters is of interest for two reasons. Knowing the sensitivity of each parameter will show where improvements in experimental accuracy will have the most impact on the accuracy of the simulation. This is useful information for deciding where to invest more time and money into the characterization of the concrete in question. The second use would be in the modification of concrete mixes for different applications. Knowing which phenomena have the greatest influence on the desired outcomes provides the opportunity for making better informed decisions in mix design.

The sensitivity of each parameter has been determined by running the simulation from section 5.2 with 50 random samples from the parameters distribution. The resulting variation in the moisture change along the specimen after 30 min can be seen in fig. 6.5.

The initial intrinsic permeability k_0 shows a medium influence on the shape of the drying front, as well as a small effect on the saturation inside the moisture clog. The initial porosity n_0 has a small influence overall, similar to the initial permeability it influences the shape of the drying front and the moisture clog saturation, but also the moisture content close to the heated surface. The influence of the initial humidity is somewhat stronger, particularly on the remaining moisture close to the heated surface and the saturation in the moisture clog. It also has a small effect on the shape of the drying front. The thermal parameters λ_{d0} and C^s_{p0} exhibit a behaviour where the influence on the dry part of the specimen is negligible, but they have a medium influence on the location of the moisture clog. The saturation seems unaffected, however. For this problem, the diffusion coefficient D seems to have almost no influence on the results. This may be an artifact of the calibration of the model on the CT data in section 5.2, which resulted in a very low diffusion coefficient. The CT scans provide an overall moisture content, making distinction between diffusion and advection difficult.

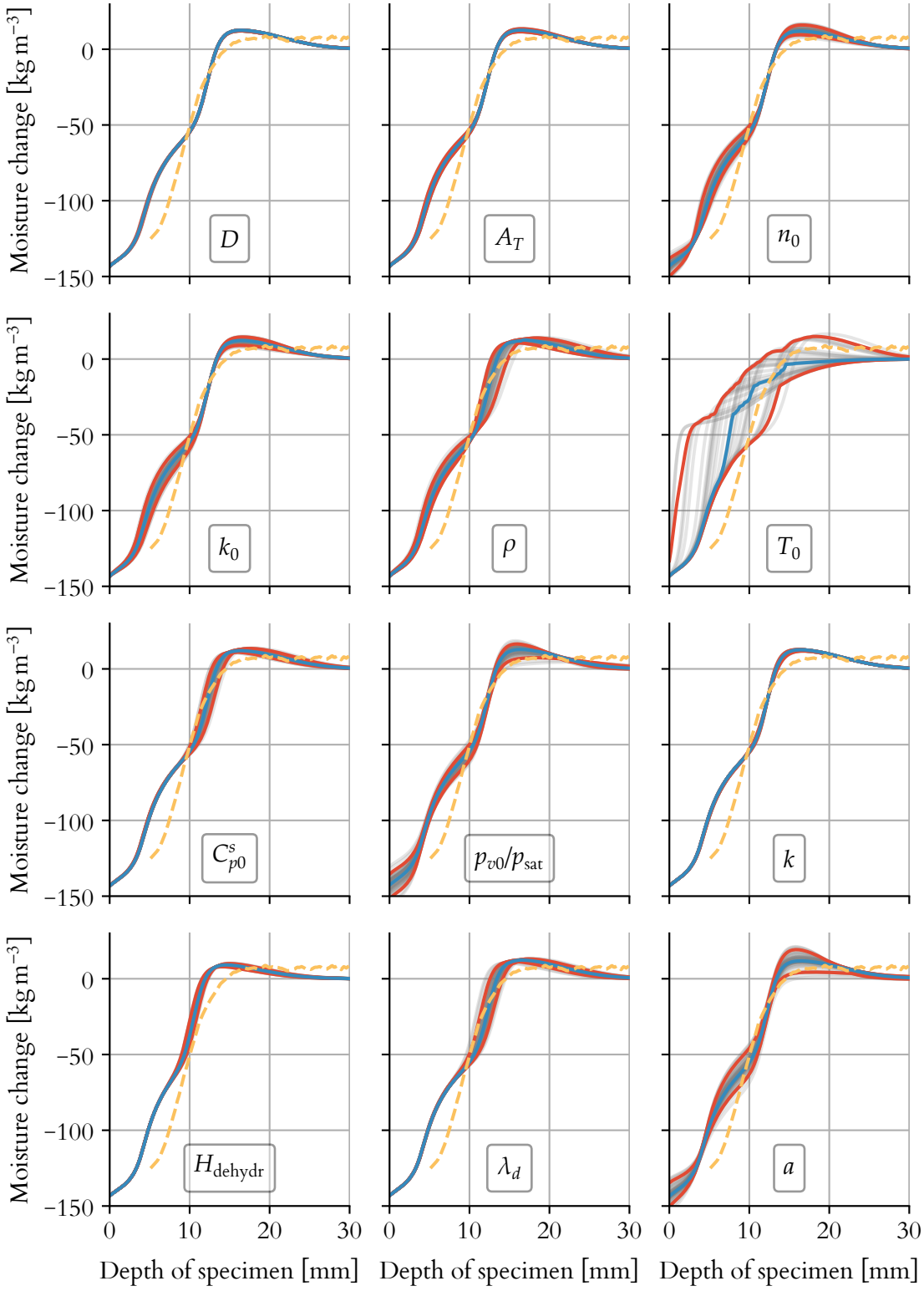

Figure 6.5.: Overview of sensitivity of different parameters for the validation problem from section 5.2. The orange line shows the CT results, the grey lines indicate each individual result, the blue line shows the median of all the simulations, and the two red lines show the fifth and 95$^{\text{th}}$ percentile.

6.4. Multidimensional sampling

Finite element models are often computationally expensive, and potentially have many input variables that follow a certain probability distribution. The number of realizations of this multivariate distribution that the model can be solved for is thus limited by time and energy. It is therefore of great interest to sample the multidimensional space as well as possible with the least number of samples.

The traditional technique for creating samples is the Monte Carlo simulation which randomly samples the distribution. When generating L samples for each of the N variables, the resulting values can be written as an $N \times L$ matrix,

$$S = \begin{bmatrix} F(x)_{11} & F(x)_{12} & \dots & F(x)_{1N} \\ F(x)_{21} & F(x)_{22} & \dots & F(x)_{2N} \\ \vdots & \vdots & \ddots & \vdots \\ F(x)_{L1} & F(x)_{L2} & \dots & F(x)_{LN} \end{bmatrix}. \tag{6.4}$$

For multidimensional problems, the resulting set of samples may not accurately reflect the variability of the distribution. An alternative is the Latin hypercube sampling [MBC79], which results in uniform sampling of multiple univariate distributions, ensuring that the resulting samples are representative of the variability. This is done by splitting the cumulative distribution function into L even segments called *strata*

$$F(x) \in \left[\frac{l-1}{L}, \frac{l}{L}\right], \quad l = 1, 2, ..., L \tag{6.5}$$

and sampling within each stratum. However, neither LHS nor Monte Carlo simulation constrain the multidimensional uniformity of the matrix of samples S.

A modified version of the LHS that aims to rectify this is used here. It is called LHSMDU and was proposed by Deutsch and Deutsch [DD12]. The main idea is to generate M times as many samples as are needed in the end, and eliminate samples that are close to each other. This is done by computing the Euclidean distance

$$D_{i,j} = \sqrt{\sum_{n=1}^{N} \left(F(x)_{in} - F(x)_{jn}\right)^2}, \tag{6.6}$$

between all the samples and removing the sample that has the lowest average of its two smallest neighboring distances. Two neighbors are considered as a tie breaker; if only one distance would be used, a pair of samples to eliminate would result. The whole algorithm can be seen in algorithm 6.1. LHSMDU is an unbiased estimator [DD12], as is the LHS on which it is based [MBC79]. In the original paper, correlation between variables can be considered by transforming the samples into Gaussian units, and then multiplying each sample by the **L** matrix from the Cholesky **LU** decomposition of the correlation matrix.

Algorithm 6.1 Multidimensional Uniformity Latin Hypercube Sampling LHSMDU

generate $N \times ML$ uniform random numbers
$I \leftarrow ML$
repeat
  for all samples i in I **do**
    calculate Euclidean distance $D_{i,j}$ to all other samples j in I with $j \neq i$
    $d_i \leftarrow$ average of the two smallest distances
  eliminate the sample with smallest average distance d; $I \leftarrow I - 1$
until only $I = L$ samples remain
for all variables n in N **do**
  rank the L inputs and use these rankings as the strata l
  generate uniform random numbers for the L strata for n according to eq. (6.5)
  sample the cumulative distribution function of n with the generated numbers

6.5. Uncertainty

The overall variability of the results gives insights into how precise our models are and how much trust we should place in the results. For this first part, the simulation from section 5.2 was performed for 500 samples of the parameter space, sampled by the Latin Hypercube sampling described in section 6.4. The variation in moisture change that results after 30 min. of heating can be seen in fig. 6.6.

The variation in moisture content is quite large. The remaining moisture close to the heated surface varies by about $30\,\mathrm{kg\,m^{-3}}$ between the fifth and 95$^{\text{th}}$ percentile. The position of the drying front, arbitrarily chosen as moisture change of $-60\,\mathrm{kg\,m^{-3}}$, ranges between about 3 mm and 10 mm for the same percentiles. Most surprisingly, the moisture gain inside the moisture clog ranges from accumulating an additional $25\,\mathrm{kg\,m^{-3}}$ to no increase over the initial condition at all.

When all parameters are allowed to vary, there are about 36 % of the cases where the model does not converge. Note that this is dependent on the type of concrete; the concrete under examination is a HPC with a low permeability. For the concrete from section 5.3 with less restricted water advection, only 2 out of the 500 samples (0.4 %) fail to converge. The cause for the loss of convergence is the saturation S_w reaching unity, which is physically impermissible. Since the input parameters are assumed to be uncorrelated for simplicity, unrealistic combinations of parameter values can be the result.

The three parameters with the strongest influence on whether the model converges are the initial humidity, the intrinsic permeability and the dehydration parameter T_0. Their kernel density estimation for converged and unconverged values, along with the combinations between the parameters, are shown in fig. 6.7. The kernel density estimation uses a Gaussian kernel with a bandwidth selected by *Scott's rule* [Sco15], that is

$$h = \sigma n^{-\frac{1}{d+4}}, \tag{6.7}$$

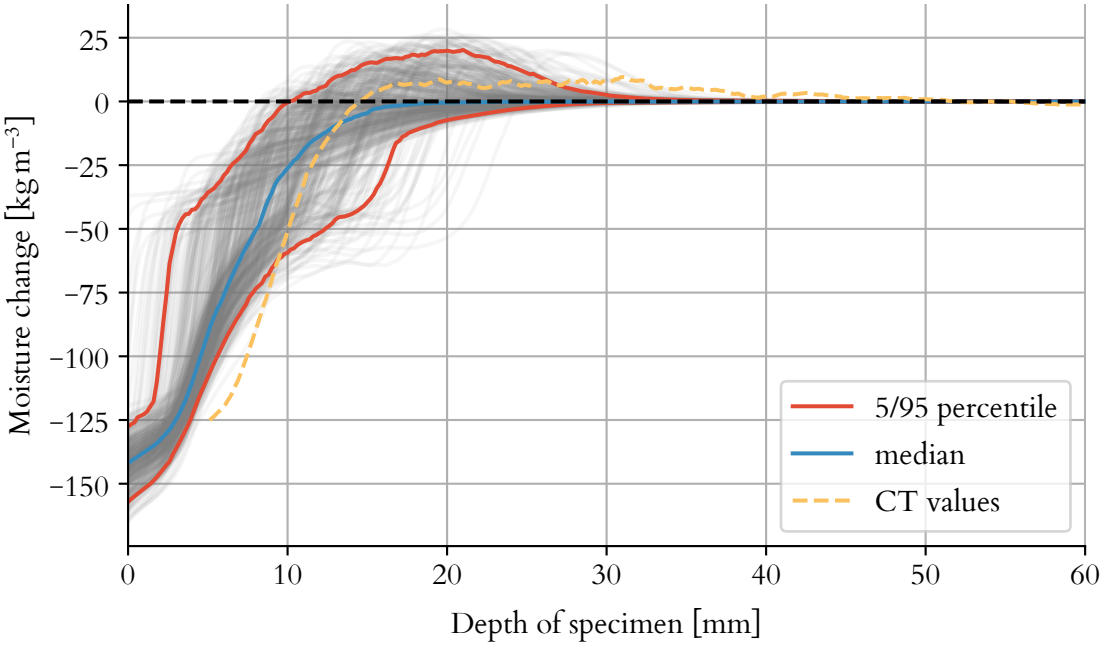

Figure 6.6.: Variation of the resulting moisture content of the simulation from section 5.2. The orange line shows the CT results, the grey lines indicate each individual result, the blue line shows the median of all the simulations, and the two red lines show the fifth and 95$^{\text{th}}$ percentile.

where h is the bandwidth, σ is the standard deviation, n is the number of data points and d is the dimension (here, $d = 1$).

The initial humidity inside the specimen controls the amount of water in the specimen, and therefore a higher value increases the chance of reaching high saturation levels. This is reflected in the bias towards higher values in the kernel density estimation of the unconverged values. The intrinsic permeability influences how fast vapour and liquid water can move along their respective gradients. If its value is low, the transport is inhibited, leading to a more pronounced moisture clog where higher levels of saturation occur. Again, this can be seen in the bias of the unconverged values, this time towards lower values. Lastly, the dehydration parameter T_0 determines the temperature with the highest water release rate. For values above zero, the conductivity increases with temperature, for values below zero it decreases. When the dehydration starts at lower temperatures, the released water is more likely to cause problems for the model.

Lastly, the parameter space sampling was applied to the problem from section 5.3. This extends the application to high temperatures, and shows the variability on a well-known problem that is often used to compare models. The maximum gas pressure as an indicator to the chance of spalling, and the location of that maximum as an indicator of the spalling depth, are investigated here. Figure 6.8 shows the histograms for the maximum gas pressure and its location, as well as the correlation between the two.

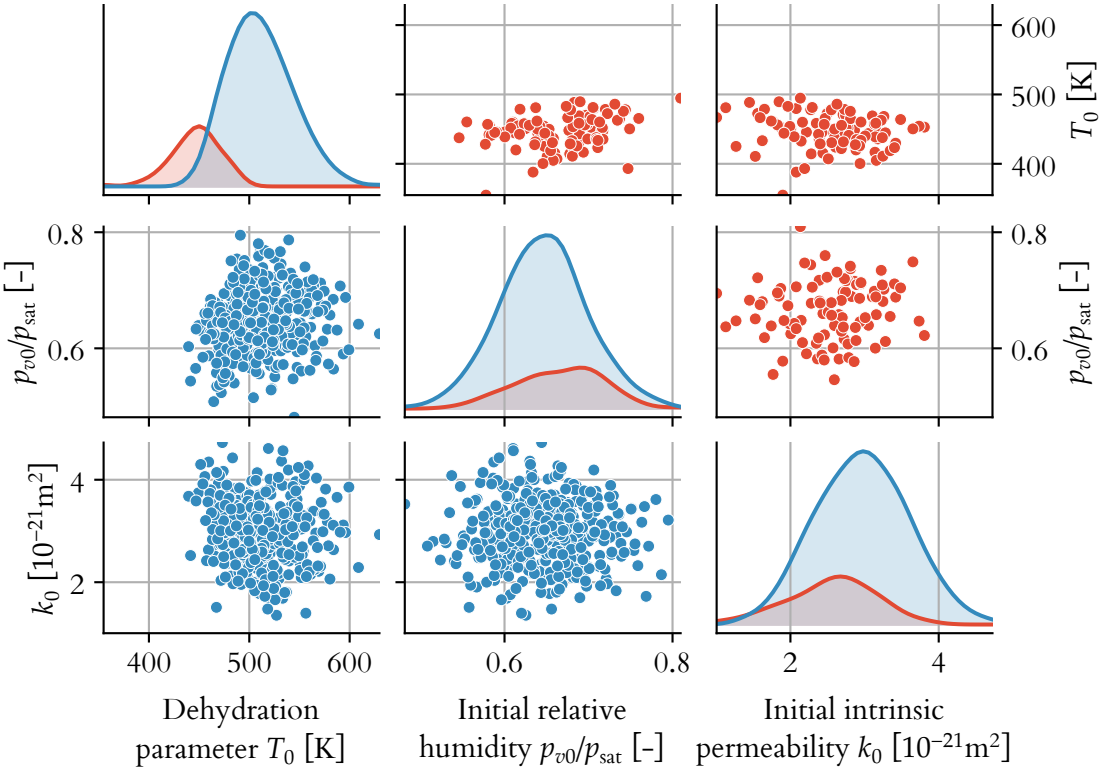

Figure 6.7.: Kernel density estimations for the converged (blue) and unconverged (red) values on the diagonal, and the combinations between the parameters on the offdiagonals.

The maximum gas pressure has a mean value of 7.5 MPa, and a standard deviation of 0.88 MPa. The mean location of the maximum is at 75.2 mm, with a standard deviation of 12.2 mm. The coefficients of variation are therefore 11.7 % for the maximum pressure and 16.2 % for its location.

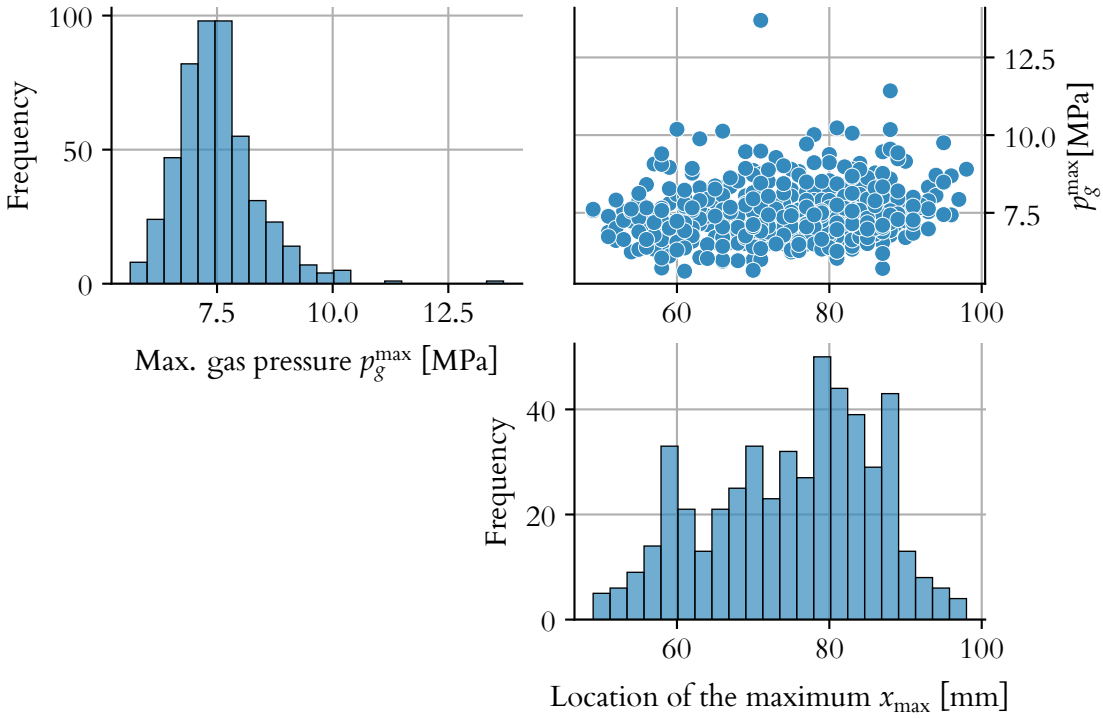

Figure 6.8.: Variation of the maximum in gas pressure and the location of this maximum.

7. Replication

This work, including all the tables and figures, is intended to be easily and fully repeatable. Reproducibility and repeatability are important parts of cumulative science. For a general introduction to reproducible computational research, see [SNTH13]. To allow repetition, finding mistakes or discrepancies between text and source code, as well as extend the analysis to new models or new data, an approach that is straightforward to use has been implemented in this work. The following section will explain its ingredients.

Firstly, all of the input data, source code, parameters and scripts should be publicly available. In our case, all of the data are available at Zenodo, via the DOI 10.5281/zenodo.6411103. This includes all the simulation code, TGA data, plotting instructions and LaTeX files.

Secondly, in order to reproduce the results, not only is it necessary to have the source code and inputs, but also the environment under which the code was executed, that is the exact versions of all the programs and libraries used. A reproducible environment (or at least a reasonable approximation) in form of a Docker container with all the required dependencies installed is available on Dockerhub at `christophpohl/thesis`. Not only does this allow anyone to rerun the code in the same computational environment, but also makes it very convenient. There is no need to manually install all the software that was used, which can be cumbersome and difficult. In addition, the Dockerfile serves as a readable description of all dependencies and the environmental setup.

Lastly, and most importantly, all the data processing should be fully automated. This way, inefficient and error-prone manual steps are avoided, and a clear chain of reproducible steps is obtained. From running the simulation, via creating the graphs, to compiling the final PDF, all programs are invoked using a build automation tool. If reproducibility is the only criterion, this is not strictly necessary. A slightly simpler shell script that runs all required steps in sequence would suffice. However, changes in any of the files would require that everything is run again from scratch, even if only changes in the graphs or wording of a small sections were made.

The use of a build automation tool avoids this by encoding the connections between the build steps, their dependencies and their outputs as a directed acyclic graph (DAG). A visual representation of such a graph can be seen in fig. 7.1. The build tool will then assemble the

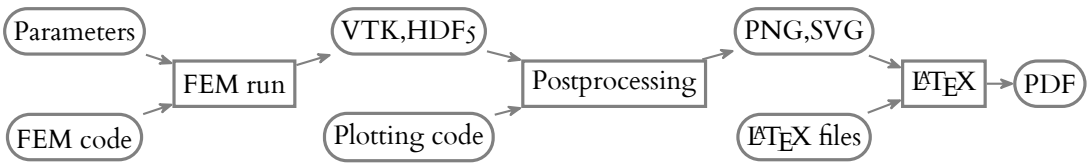

Figure 7.1.: Dependency graph of prototypical numerical methods paper.

DAG, and when asked to build the final PDF, traverse it to find the tasks that are not up to date and run them. A task is not up to date when either its output is missing, or one of its dependencies has changed since the last time it was run. That way, changes in any of the predecessors will always trigger a reevaluation of all necessary tasks, and no running of unnecessary steps is taking place.

8. Conclusion

Spalling is a complex phenomenon that combines air and water transport in porous media, heat conduction and chemical changes. With many practical implications for the safety and reliability of concrete structures, a lot of experimental and numerical work has been published on the subject. However, no reliable, widely accepted model to predict the onset of spalling in engineering circumstances has emerged. Moisture distribution and transport within the concrete is a key factor for spalling risk. An assessment of the different approaches that have been proposed can be found in chapter 4.

One of the major difficulties is the quantitative description of the dehydration. Constitutive equations based on thermogravimetric analysis have been found to be inadequate for the description of the process inside actual macroscale structures and specimens. An alternative based on CT measurements taken during heating has been proposed and implemented here. The validation in section 5.2 shows a drastic improvement over TGA based approaches.

Of the four balance equations describing the process, the skeleton mass balance is most often neglected. In contrast, the skeleton mass balance has been solved here. While the impact on temperature and pore pressure distributions is comparatively low, this choice is thermodynamically correct and couples dehydration and porosity evolution. As a result, one fewer constitutive equation is needed, and additional experiments can either be skipped to reduce costs, or used for validation.

The complexity of the problem is reflected in the complexity of the models. There are numerous parameters with values based on numerous experiments with varying accuracy. In spite of that, the results are often presented with a high precision, leading to a false confidence in the model. The variability in the input parameters was investigated in chapter 6. Based on these findings, the parameter space was sampled to quantify the uncertainty in the results of the model. A sensitivity analysis shows the relative influence of each input parameter on the uncertainty, pointing toward the experiments where work on improving their accuracy is likely to have the most impact. The overall uncertainty for a popular benchmark problem was found to be between 12 and 17 %. This provides a quantitative basis for judging the confidence we place in the models, as well as give a range of expected values for practical engineering applications.

Many avenues of exploration within the context of spalling simulation are still open.For example, while some models propose an influence of damage on the water transport parameters, no experimental work for obtaining the desired parameters has been done. In general, openly available data on the properties of concrete would greatly aid model development, validation and uncertainty quantification.

Experimental techniques such as nuclear magnetic resonance spectroscopy allow to distinguish between free and boundary water. In combination with appropriate postprocessing of numerical results, NMR could be used for further validation and insight into the state of

water inside the pores. Multi-scale modeling, where a molecular dynamics study on the scale of individual pores is coupled to a macroscopic models as presented here, would likely lead to a more fundamental understanding of the processes involved.

Most models, including the one presented here, use only the basic tools of numerics—Lagrange elements, Euler backward time integration and Newton-Raphson as a nonlinear solver. The model may fail to converge if the saturation reaches unity, as values beyond one are not physically feasible. This is most likely for concretes with low permeability, a high release of dehydrated water and high initial moisture content. And while the performance and stability of these methods is adequate, a numerical study of the components of the solver may lead to faster and more robust computation.

Bibliography

[ABB+13] Aït-Mokhtar, A. *et al.*, 'Experimental investigation of the variability of concrete durability properties,' *Cement and Concrete Research*, vol. 45, pp. 21–36, Mar. 2013. DOI: 10.1016/j.cemconres.2012.11.002.

[ABH+15] Alnæs, M. S. *et al.*, 'The FEniCS project version 1.5,' *Archive of Numerical Software*, vol. 3, no. 100, 2015. DOI: 10.11588/ans.2015.100.20553.

[Bam87] Bamforth, P. B., 'The relationship between permeability coefficients for concrete obtained using liquid and gas,' *Magazine of Concrete Research*, vol. 39, no. 138, pp. 3–11, Mar. 1987. DOI: 10.1680/macr.1987.39.138.3.

[BB86] Bachmat, Y. and Bear, J., 'Macroscopic modelling of transport phenomena in porous media. 1: The continuum approach,' *Transp Porous Med*, vol. 1, no. 3, pp. 213–240, Sep. 1986. DOI: 10.1007/bf00238181.

[BK96] Bažant, Z. P. and Kaplan, M. F., *Concrete at high temperatures, Material properties and mathematical models*, ser. Concrete design and Construction Series. Longman, 1996, ISBN: 0-582-08626-4.

[BMG+18] Baydoun, R. *et al.*, 'Finite element modeling of thermo-hygral behaviour of concrete exposed to fire,' *Symposium on Concrete Modelling (CONMOD2018)*, 2018.

[BMLC99] Baroghel-Bouny, V. *et al.*, 'Characterization and identification of equilibrium and transfer moisture properties for ordinary and high-performance cementitious materials,' *Cement and Concrete Research*, vol. 29, no. 8, pp. 1225–1238, Aug. 1999. DOI: 10.1016/s0008-8846(99)00102-7.

[BMS95] Baggio, P., Majorana, C. E. and Schrefler, B. A., 'Thermo-hygro-mechanical analysis of concrete,' *Int. J. Numer. Meth. Fluids*, vol. 20, no. 6, pp. 573–595, Mar. 1995. DOI: 10.1002/fld.1650200611.

[BN72] Bažant, Z. P. and Najjar, L. J., 'Nonlinear water diffusion in nonsaturated concrete,' *Matériaux et Construction*, vol. 5, no. 1, pp. 3–20, Jan. 1972. DOI: 10.1007/BF02479073.

[BT78] Bažant, Z. and Thonguthai, W., 'Pore pressure and drying of concrete at high temperature,' English (US), *Journal of Engineering Mechanics - ASCE*, vol. 104, no. 5, pp. 1059–1079, Jan. 1978.

[CC05] Chung, J. H. and Consolazio, G. R., 'Numerical modeling of transport phenomena in reinforced concrete exposed to elevated temperatures,' *Cement and*

Concrete Research, vol. 35, no. 3, pp. 597–608, Mar. 2005. DOI: 10.1016/j.cemconres.2004.05.037.

[CD02] Cockburn, B. and Dawson, C., 'Approximation of the velocity by coupling discontinuous galerkin and mixed finite element methods for flow problems,' *Computational Geosciences*, vol. 6, no. 3, pp. 505–522, Sep. 2002. DOI: 10.1023/A:1021203618109.

[CEN04] CEN, 'Eurocode 2: Design of concrete structures - Part 1-2: General rules - Structural fire design,' European Committee for Standardization, European Standard EN-1992-1-2, 2004.

[Cen06] Cengel, Y. A., *Heat and Mass Transfer: A Practical Approach*, 3rd. McGraw-Hill, 2006, ISBN: 978-007-125739-8.

[CSM93] Chaube, R., Shimomura, T. and Maekawa, K., 'Multi-phase water movement in concrete as a multi-component system,' in *Creep and shrinkage of concrete: proceedings of the fifth international RILEM symposium*, Bažant, Z. and Carol, I., Eds., 1993.

[Dai88] Daian, J.-F., 'Condensation and isothermal water transfer in cement mortar. Part I - pore size distribution, equilibrium water condensation and imbibition,' *Transp Porous Med*, vol. 3, no. 6, pp. 563–589, Dec. 1988. DOI: 10.1007/bf00959103.

[DD12] Deutsch, J. L. and Deutsch, C. V., 'Latin hypercube sampling with multidimensional uniformity,' *Journal of Statistical Planning and Inference*, vol. 142, no. 3, pp. 763–772, Mar. 2012. DOI: 10.1016/j.jspi.2011.09.016.

[DDW+18] Dauti, D. *et al.*, 'Modeling concrete exposed to high temperature: Impact of dehydration and retention curves on moisture migration,' *Int J Numer Anal Methods Geomech*, vol. 42, no. 13, pp. 1516–1530, Jun. 2018. DOI: 10.1002/nag.2802.

[DK09] Dwaikat, M. and Kodur, V., 'Hydrothermal model for predicting fire-induced spalling in concrete structural systems,' *Fire Safety Journal*, vol. 44, no. 3, pp. 425–434, Apr. 2009. DOI: 10.1016/j.firesaf.2008.09.001.

[DPB06] Davie, C. T., Pearce, C. J. and Bićanić, N., 'Coupled heat and moisture transport in concrete at elevated temperatures—effects of capillary pressure and adsorbed water,' *Numerical Heat Transfer, Part A: Applications*, vol. 49, no. 8, pp. 733–763, Sep. 2006. DOI: 10.1080/10407780500503854.

[DPB10] ———, 'A fully generalised, coupled, multi-phase, hygro-thermo-mechanical model for concrete,' *Materials and Structures*, vol. 43, no. S1, pp. 13–33, Apr. 2010. DOI: 10.1617/s11527-010-9591-y.

[DPB14] Davie, C., Pearce, C. and Bićanić, N., 'Fully coupled, hygro-thermo-mechanical sensitivity analysis of a pre-stressed concrete pressure vessel,' *Engineering Struc-*

tures, vol. 59, pp. 536–551, Feb. 2014. DOI: 10.1016/j.engstruct.2013.10.033.

[DTD+18] Dauti, D. *et al.*, 'Analysis of moisture migration in concrete at high temperature through in-situ neutron tomography,' *Cement and Concrete Research*, vol. 111, pp. 41–55, Sep. 2018. DOI: 10.1016/j.cemconres.2018.06.010.

[Fur96] Furbish, D. J., *Fluid Physics in Geology: An Introduction to Fluid Motions on Earth's Surface and within Its Crust*. Oxford University Press, USA, 1996, ISBN: 978-0-19-507701-8.

[GBS96] Gawin, D., Baggio, P. and Schrefler, B., 'Modeling heat and moisture transfer in deformable building materials,' *Archives of Civil Engineering*, vol. XLII, pp. 325–349, Jan. 1996.

[GMS99] Gawin, D., Majorana, C. E. and Schrefler, B. A., 'Numerical analysis of hygro-thermal behaviour and damage of concrete at high temperature,' *Mechanics of Cohesive-frictional Materials*, vol. 4, no. 1, pp. 37–74, Jan. 1999. DOI: 10.1002/(sici)1099-1484(199901)4:1<37::aid-cfm58>3.0.co;2-s.

[GP11] Gawin, D. and Pesavento, F., 'An overview of modeling cement based materials at elevated temperatures with mechanics of multi-phase porous media,' *Fire Technol*, vol. 48, no. 3, pp. 753–793, Feb. 2011. DOI: 10.1007/s10694-011-0216-y.

[GPCG15] Gales, J. *et al.*, 'Fire performance of sustainable recycled concrete aggregates: Mechanical properties at elevated temperatures and current research needs,' *Fire Technol*, vol. 52, no. 3, pp. 817–845, Jun. 2015. DOI: 10.1007/s10694-015-0504-z.

[GPS02] Gawin, D., Pesavento, F. and Schrefler, B. A., 'Modelling of hygro-thermal behaviour and damage of concrete at temperature above the critical point of water,' *Int. J. Numer. Anal. Meth. Geomech.*, vol. 26, no. 6, pp. 537–562, 2002. DOI: 10.1002/nag.211.

[GPS03] ———, 'Modelling of hygro-thermal behaviour of concrete at high temperature with thermo-chemical and mechanical material degradation,' *Computer Methods in Applied Mechanics and Engineering*, vol. 192, no. 13-14, pp. 1731–1771, Mar. 2003. DOI: 10.1016/s0045-7825(03)00200-7.

[GPS04] ———, 'Modelling of deformations of high strength concrete at elevated temperatures,' *Mat. Struct.*, vol. 37, no. 4, pp. 218–236, May 2004. DOI: 10.1007/bf02480631.

[GPS06] ———, 'Hygro-thermo-chemo-mechanical modelling of concrete at early ages and beyond. Part I: Hydration and hygro-thermal phenomena,' *Int. J. Numer. Meth. Engng*, vol. 67, no. 3, pp. 299–331, 2006. DOI: 10.1002/nme.1615.

[GPS11a] ———, 'What physical phenomena can be neglected when modelling concrete at high temperature? A comparative study. Part 1: Physical phenomena and mathematical model,' *International Journal of Solids and Structures*, vol. 48, no. 13, pp. 1927–1944, Jun. 2011. DOI: 10.1016/j.ijsolstr.2011.03.004.

[GPS11b] ———, 'What physical phenomena can be neglected when modelling concrete at high temperature? A comparative study. Part 2: Comparison between models,' *International Journal of Solids and Structures*, vol. 48, no. 13, pp. 1945–1961, Jun. 2011. DOI: 10.1016/j.ijsolstr.2011.03.003.

[GS82] Gregg, S. J. and Sing, K. S., *Adsorption, Surface Area and Porosity*, Second Edition. Academic Press, 1982, ISBN: 0-12-300956-1.

[HG79] Hassanizadeh, M. and Gray, W. G., 'General conservation equations for multi-phase systems: 1. Averaging procedure,' *Advances in Water Resources*, vol. 2, pp. 131–144, Mar. 1979. DOI: 10.1016/0309-1708(79)90025-3.

[HP86] Halle, B. and Piculell, L., 'Water spin relaxation in colloidal systems. Part 3: Interpretation of the low-frequency dispersion,' *Journal of the Chemical Society, Faraday Transactions 1: Physical Chemistry in Condensed Phases*, vol. 82, no. 2, p. 415, 1986. DOI: 10.1039/f19868200415.

[HWS+00] Hartnig, C. *et al.*, 'Modifications of the hydrogen bond network of liquid water in a cylindrical SiO2 pore,' *Journal of Molecular Liquids*, vol. 85, no. 1-2, pp. 127–137, Apr. 2000. DOI: 10.1016/s0167-7322(99)00169-5.

[IE04] Ichikawa, Y. and England, G., 'Prediction of moisture migration and pore pressure build-up in concrete at high temperatures,' *Nuclear Engineering and Design*, vol. 228, no. 1-3, pp. 245–259, Mar. 2004, SMiRT 16. Selected and Updated Papers from the 16th International Conference on Structural Mechanics in Reactor Technology, Washington DC. DOI: 10.1016/j.nucengdes.2003.06.011.

[Jen08] Jennings, H. M., 'Refinements to colloid model of C-S-H in cement: Cm-ii,' *Cement and Concrete Research*, vol. 38, no. 3, pp. 275–289, Mar. 2008. DOI: 10.1016/j.cemconres.2007.10.006.

[JN10] Johannesson, B. and Nyman, U., 'A numerical approach for non-linear moisture flow in porous materials with account to sorption hysteresis,' *Transport in Porous Media*, vol. 84, no. 3, pp. 735–754, Feb. 2010. DOI: 10.1007/s11242-010-9538-3.

[KGW12] Kolditz, O., Görke, U.-J. and Wang, W., Eds., *Thermo-Hydro-Mechanical-Chemical Processes in Fractured Porous Media, Benchmarks and Examples*. Springer-Verlag Berlin Heidelberg, 2012, ISBN: 978-3-642-27176-2.

[Kli41] Klinkenberg, L. J., 'The permeability of porous media to liquids and gases,' *Drilling and Production Practice*, pp. 200–213, 1941.

[KNK21] Kirytopoulos, K., Ntzeremes, P. and Kazaras, K., 'Tunnels, safety, and security issues—risk assessment for road tunnels: State-of-the-art practices and challenges,' in *International Encyclopedia of Transportation*, Vickerman, R., Ed., Oxford: Elsevier, 2021, pp. 713–718, ISBN: 978-0-08-102672-4. DOI: 10.1016/B978-0-08-102671-7.10203-9.

[Kol89] Kollek, J. J., 'The determination of the permeability of concrete to oxygen by the cembureau method—a recommendation,' *Materials and Structures*, vol. 22, no. 3, pp. 225–230, May 1989. DOI: 10.1007/bf02472192.

[Kuk10] Kukla, K., 'Concrete at high temperatures: Hygro-thermo-mechanical degredation of concrete,' PhD thesis, University of Glasgow, 2010.

[Kün95] Künzel, H. M., 'Simultaneous heat and moisture transport in building components. one- and two-dimensional calculation using simple parameters,' Fraunhofer Institute of Building Physics, 1995.

[LLS06] Li, X., Li, R. and Schrefler, B. A., 'A coupled chemo-thermo-hygro-mechanical model of concrete at high temperature and failure analysis,' *Int. J. Numer. Anal. Meth. Geomech.*, vol. 30, no. 7, pp. 635–681, Jun. 2006. DOI: 10.1002/nag.495.

[LR94] Lee, S. H. and Rossky, P. J., 'A comparison of the structure and dynamics of liquid water at hydrophobic and hydrophilic surfaces—a molecular dynamics simulation study,' *The Journal of Chemical Physics*, vol. 100, no. 4, pp. 3334–3345, Feb. 1994. DOI: 10.1063/1.466425.

[LS98] Lewis, R. W. and Schrefler, B. A., *The Finite Element Method in the Static and Dynamic Deformation and Consolidation of Porous Media*, 2nd ed. John Wiles & Sons, Ltd., 1998, ISBN: 978-0-471-92809-6.

[LSS16] Lothenbach, B., Scrivener, K. and Snellings, R., Eds., *A Practical Guide to Microstructural Analysis of Cementitious Materials*. CRC Press, 2016, ISBN: 978-1-4987-3867-5.

[Lui66] Luikov, A. V., *Heat and Mass Transfer in Capillary-Porous Bodies*. Elsevier, 1966, ISBN: 978-1-4832-0065-1. DOI: 10.1016/c2013-0-08150-9.

[Mal84] Malhotra, H. L., 'Spalling of concrete in fires,' CIRIA, Technical note 118, 1984.

[MBC79] McKay, M. D., Beckman, R. J. and Conover, W. J., 'A comparison of three methods for selecting values of input variables in the analysis of output from a computer code,' *Technometrics*, vol. 21, no. 2, p. 239, May 1979. DOI: 10.2307/1268522.

[MPCB13] Mindeguia, J.-C. *et al.*, 'Experimental analysis of concrete spalling due to fire exposure,' *European Journal of Environmental and Civil Engineering*, vol. 17, no. 6, pp. 453–466, Jun. 2013. DOI: 10.1080/19648189.2013.786245.

[Ort85] Ortiz, M., 'A constitutive theory for the inelastic behavior of concrete,' *Mechanics of Materials*, vol. 4, no. 1, pp. 67–93, Mar. 1985. DOI: 10.1016/0167-6636(85)90007-9.

[PE04] Pont, S. and Ehrlacher, A., 'Numerical and experimental analysis of chemical dehydration, heat and mass transfers in a concrete hollow cylinder submitted to high temperatures,' *International Journal of Heat and Mass Transfer*, vol. 47, no. 1, pp. 135–147, Jan. 2004. DOI: 10.1016/s0017-9310(03)00381-8.

[Pes00] Pesavento, F., 'Non-linear modelling of concrete as multiphase porous material in high temperature conditions,' Ph.D. dissertation, University of Padova, 2000.

[PSO+18] Powierza, B. *et al.*, 'Water migration in one-side heated concrete: 4d in-situ CT monitoring of the moisture-clog-effect,' *Journal of Nondestructive Evaluation*, vol. 38, no. 1, Dec. 2018. DOI: 10.1007/s10921-018-0552-7.

[PSS16] Pesavento, F., Schrefler, B. A. and Sciumè, G., 'Multiphase flow in deforming porous media: A review,' *Arch Computat Methods Eng*, vol. 24, no. 2, pp. 423–448, Mar. 2016. DOI: 10.1007/s11831-016-9171-6.

[PŠU21] Pohl, C., Šmilauer, V. and Unger, J. F., 'A three-phase transport model for high-temperature concrete simulations validated with X-ray CT data,' *Materials*, vol. 14, no. 17, 2021. DOI: 10.3390/ma14175047.

[SCL+15] Shen, W. *et al.*, 'Quantifying CO2 emissions from China's cement industry,' *Renewable and Sustainable Energy Reviews*, vol. 50, pp. 1004–1012, 2015. DOI: 10.1016/j.rser.2015.05.031.

[Sco15] Scott, D. W., *Multivariate Density Estimation: Theory, Practice, and Visualization*, 2nd ed., ser. Wiley Series in Probability and Statistics. John Wiley & Sons, Inc., 2015, ISBN: 978-0-471-69755-8.

[Ser80] Sermon, P. A., 'Interaction of water with some silicas,' *Journal of the Chemical Society, Faraday Transactions 1: Physical Chemistry in Condensed Phases*, vol. 76, no. 0, p. 885, 1980. DOI: 10.1039/f19807600885.

[SH89] Schneider, U. and Herbst, H. J., 'Permeabilität und Porosität von Beton bei hohen Temperaturen,' *Deutscher Ausschuss für Stahlbeton*, vol. 403, pp. 23–52, 1989.

[SNTH13] Sandve, G. K. *et al.*, 'Ten simple rules for reproducible computational research,' *PLoS Computational Biology*, vol. 9, no. 10, Bourne, P. E., Ed., e1003285, Oct. 2013. DOI: 10.1371/journal.pcbi.1003285.

[SW86] Sengers, J. V. and Watson, J. T. R., 'Improved international formulations for the viscosity and thermal conductivity of water substance,' *Journal of Physical and Chemical Reference Data*, vol. 15, no. 4, pp. 1291–1314, Oct. 1986. DOI: 10.1063/1.555763.

[TJ08] Thomas, J. and Jennings, H. 'Science of concrete.' (2008), [Online]. Available: http://iti.northwestern.edu/cement/index.html.

[TLP01] Tenchev, R. T., Li, L. Y. and Purkiss, J. A., 'Finite element analysis of coupled heat and moisture transfer in concrete subjected to fire,' *Numerical Heat Transfer, Part A: Applications*, vol. 39, no. 7, pp. 685–710, May 2001. DOI: 10.1080/10407780119853.

[TLPK01] Tenchev, R. T. *et al.*, 'Finite element analysis of coupled heat and mass transfer in concrete when it is in a fire,' *Magazine of Concrete Research*, vol. 53, no. 2, pp. 117–125, Apr. 2001. DOI: 10.1680/macr.2001.53.2.117.

[TP05] Tenchev, R. and Purnell, P., 'An application of a damage constitutive model to concrete at high temperature and prediction of spalling,' *International Journal of Solids and Structures*, vol. 42, no. 26, pp. 6550–6565, Dec. 2005. DOI: 10.1016/j.ijsolstr.2005.06.016.

[TS95] Thomas, H. R. and Sansom, M. R., 'Fully coupled analysis of heat, moisture, and air transfer in unsaturated soil,' *Journal of Engineering Mechanics*, vol. 121, no. 3, pp. 392–405, Mar. 1995. DOI: 10.1061/(asce)0733-9399(1995)121:3(392).

[VČD+97] Vodák, F. *et al.*, 'Thermophysical properties of concrete for nuclear-safety related structures,' *Cement and Concrete Research*, vol. 27, no. 3, pp. 415–426, Mar. 1997. DOI: 10.1016/s0008-8846(97)00033-1.

[Wat43] Watson, K., 'Thermodynamics of the liquid state,' *Industrial & Engineering Chemistry*, vol. 35, no. 4, pp. 398–406, 1943.

[Whi77] Whitaker, S., 'Simultaneous heat, mass, and momentum transfer in porous media: A theory of drying,' Advances in Heat Transfer, vol. 13, Hartnett, J. P. and Irvine, T. F., Eds., pp. 119–203, 1977. DOI: 10.1016/S0065-2717(08)70223-5.

[Whi88] Whiting, D., 'Permeability of selected concretes,' *ACI Symposium Publication*, vol. 108, 1988.

[WP93] Wagner, W. and Pruss, A., 'International equations for the saturation properties of ordinary water substance. Revised according to the international temperature scale of 1990. Addendum to J. Phys. Chem. Ref. Data 16, 893 (1987),' *Journal of Physical and Chemical Reference Data*, vol. 22, no. 3, pp. 783–787, May 1993. DOI: 10.1063/1.555926.

[YJA17] Yuan, Y., Jiang, X. and Ai, Q., 'Probabilistic assessment for concrete spalling in tunnel structures,' *ASCE-ASME Journal of Risk and Uncertainty in Engineering Systems, Part A: Civil Engineering*, vol. 3, p. 04 017 011, Dec. 2017. DOI: 10.1061/AJRUA6.0000912.

[ZD13] Zhang, H. and Davie, C., 'A numerical investigation of the influence of pore pressures and thermally induced stresses for spalling of concrete exposed to

elevated temperatures,' *Fire Safety Journal*, vol. 59, pp. 102–110, Jul. 2013. DOI: 10.1016/j.firesaf.2013.03.019.

[ZW73] Z. Harmathy, T. and W. Allen, L., 'Thermal properties of selected masonry unit concretes,' *JP*, vol. 70, no. 2, Feb. 1973. DOI: 10.14359/11193.

A. Selected excerpts from the source code

A.1. The `DofWrapper` class

As discussed in section 4.6, the choice of independent variables has an influence on the description of the boundary conditions, the numerical performance and the interpretation of the results. Several different variants have been proposed; a discussion can be found in the aforementioned section. The implementation of the finite element code is based on FEniCS [ABH+15], whose UFL language for expressing the weak form enables a degree of symbolic computation. Together with an appropriate abstraction, this allows easily replacing the choice of independent variables. The `DofWrapper` base class and its derived classes provide an easy mechanism for these replacements.

The base class stores the actual DoFs, `self.dofs = Function(self.V)`, which represents eq. (4.95) with no distinction for the choice of variables. The derived classes then determine which subspace gets mapped to p_g, p_a, p_v, ρ_v or p_c. Each derived class has to provide an `extract_components` function for this mapping, to be called in line 59. The `fluids.PoreState` is an abstraction for the implementation of the weak forms, collecting the constitutive equations for water and air. In addition, the `DofWrapper` class provides an easy mechanism for switching between the two ways of handling porosity, either as an additional DoF (`porosity_as_dof=True`) or as a constitutive equation (`porosity_as_dof=False`) that needs to supplied as python function to `porosity_fn`. While the computations have mostly been done with linear elements, the order of the finite elements can easily be changed by passing the desired order to the `order` parameter of this class.

```
26 class _DofWrapper:
27     def __init__(self, mesh, order, porosity_as_dof=True,
        ↪ porosity_fn=None):
28         P = FiniteElement("P", interval, order)
29         self.porosity_as_dof = porosity_as_dof
30         if self.porosity_as_dof:
31             element = MixedElement([P, P, P, P])
32         else:
33             element = MixedElement([P, P, P])
34 
35         self.V = FunctionSpace(mesh, element)
36 
37         self.dofs = Function(self.V)
38         self._dofs_prev = Function(self.V)
39         self._dofs_prev_old = Function(self.V) # for postprocessing
```

```
40
41          self._unknowns = _make_variables(self.dofs)
42          self._unknowns_prev = _make_variables(self._dofs_prev)
43          self._unknowns_prev_old = _make_variables(self._dofs_prev_old)
44
45          self._test_function = TestFunction(self.V)
46
47          if self.porosity_as_dof:
48              self.porosity = self._unknowns[-1]
49              self.porosity_prev = self._unknowns_prev[-1]
50              self.porosity_prev_old = self._unknowns_prev_old[-1]
51          else:
52              # note: above, -1 corresponds to porosity, here, -1
                ↪  corresponds to temperature
53              self.porosity = porosity_fn(self._unknowns[-1])
54              self.porosity_prev = porosity_fn(self._unknowns_prev[-1])
55              self.porosity_prev_old =
                ↪  porosity_fn(self._unknowns_prev_old[-1])
56
57      @property
58      def porestate(self):
59          return
            ↪  fluids.PoreState(*self.extract_components(self._unknowns))
```

The `Baydoun` class is one such class derived from `DofWrapper`, and will be used as an example. Everything applies to the other classes, namely `Tenchev` and `Gawin`, as well. Each derived class has to provide an `extract_components` function that takes the DoFs and return the full set of $\{p_a, p_v, p_g, p_c, \rho_v, T\}$, defined on line 126. In addition, it provides functions for the boundary conditions (`gas_dirichlet_bc` and `temperature_dirichlet_bc`), as well as initial conditions (`set_initial_condition`), since they also depend on the choice of the independent variables.

```
116 class Baydoun(_DofWrapper):
117     """p_v, p_a, T"""
118
119     def __init__(self, *args):
120         super().__init__(*args)
121         if self.porosity_as_dof:
122             self.v_m, self.v_a, self.v_T, self.v_n =
                ↪  split(self._test_function)
123         else:
124             self.v_m, self.v_a, self.v_T = split(self._test_function)
125
126     def extract_components(self, unknowns):
```

```
127             if self.porosity_as_dof:
128                 p_v, p_a, T, _ = unknowns
129             else:
130                 p_v, p_a, T = unknowns
131             p_g = p_v + p_a
132             p_c = fluids.capillary_pressure(p_v, T)
133             rho_v = fluids.vapour_density(p_v, T)
134 
135             return (p_a, p_v, p_g, p_c, rho_v, T)
136 
137         def gas_dirichlet_bc(self, value, boundary, environment):
138             p_a = float(value - environment.vapour_pressure)
139             return DirichletBC(self.V.sub(1), p_a, boundary)
140 
141         def temperature_dirichlet_bc(self, value, boundary):
142             return DirichletBC(self.V.sub(2), value, boundary)
143 
144         def set_initial_condition(
145             self, gas_pressure, rel_humidity, temperature,
                ↪ initial_porosity=None
146         ):
147             vapour_pressure = _rh_to_pv(rel_humidity, temperature)
148             dry_air_pressure = gas_pressure - vapour_pressure
149             if self.porosity_as_dof:
150                 ic_values = Constant(
151                     [vapour_pressure, dry_air_pressure, temperature,
                        ↪ initial_porosity]
152                 )
153             else:
154                 ic_values = Constant([vapour_pressure, dry_air_pressure,
                    ↪ temperature])
155             self.dofs.assign(ic_values)
156             self._dofs_prev.assign(ic_values)
```

For convenience and brevity in the balance equations, all the water, air and temperature properties are collected in a `PoreState` object. It takes the full set of $\{p_a, p_v, p_g, p_c, \rho_v, T\}$ from the `DofWrapper` and gives access to viscosities, heat capacities, vaporization enthalpies and more:

```
270 class PoreState:
271     """The PoreState is a wrapper for all the constitutive relations of air
272     and water. You plug in the independent variables and can access all other
273     pressures, densities and viscosities."""
274 
```

```
275     def __init__(self, p_a, p_v, p_g, p_c, rho_v, T):
276         self.capillary_pressure = p_c
277         self.gas_pressure = p_g
278         self.vapour_pressure = p_v
279         self.air_pressure = p_a
280         self.vapour_density = rho_v
281         self.T = T
282 
283         self.saturation_pressure = saturation_pressure(T)
284         self.subcritical = dolfin.le(T, T_CRIT)
285         self.vaporization_enthalpy = vaporization_enthalpy(T)
286 
287         self.air_density = air_density(self.air_pressure, T)
288         self.gas_density = self.air_density + self.vapour_density
289 
290         self.gas_molar_mass = gas_molar_mass(
291             self.air_density, self.vapour_density, self.gas_density
292         )
293         self.air_molar_mass = AIR_MOLAR_MASS
294         self.water_molar_mass = WATER_MOLAR_MASS
295         self.gas_dynamic_viscosity = gas_dynamic_viscosity(
296             self.air_pressure, self.gas_pressure, T
297         )
298         self.gas_heat_capacity = gas_heat_capacity(
299             self.air_density, self.vapour_density, T
300         )
301 
302         self.water_density = water_density(T)
303         self.water_dynamic_viscosity = water_dynamic_viscosity(T)
304         self.water_pressure = self.gas_pressure - self.capillary_pressure
305         self.water_heat_capacity = water_heat_capacity(T)
306         self.water_expansion_coefficient = water_expansion_coefficient(
307             self.water_density, T
308         )
```

A.2. Dehydration formulations

Several different dehydration formulations have been compared in section 5.2 (see also appendix B). To treat the different formulations the same way in client code, here the balance equations and postprocessing stages, polymorphism is used. The `Dehydration` base class provides `mass` and `maximally_hydrated_water` methods for the user, and the derived classes only need to implement a `degree` method. While `_mass` method (note the leading

underscore) computes the actual value for the dehydrated water mass, the `mass` method ensures that the irreversibility of the dehydration is maintained.

The base class is an abstract base class as indicated by its `ABC` parent class, and `degree` an abstract method. This is not strictly necessary, but will aid future programmers who want to add their own dehydration class. The abstract base class will ensure that the `degree` method is present, or give a helpful error message otherwise.

```
25 class Dehydration(ABC):
26     @abstractmethod
27     def degree(self, T, gamma_old, dt):
28         pass
29 
30     def __init__(self, rho_c, nu):
31         self.rho_c = rho_c
32         self.nu = nu
33 
34     def mass(self, T, gamma, dt):
35         degree_new = self.degree(T, gamma, dt)
36         gamma_new = ufl.Max(gamma, degree_new)
37         return self._mass(gamma_new)
38 
39     def _mass(self, gamma):
40         return - self.rho_c * self.nu * gamma
41 
42     def maximally_hydrated_water(self):
43         return - self.rho_c * self.nu
```

The `Gawin` class is one of the dehydration descriptions that was compared, and is shown here as an example for a derived dehydration class implementation.

```
46 class Gawin(Dehydration):
47     """See Gawin+11a"""
48 
49     def __init__(self, dehydration_prm, rho_c):
50         self._a1 = dehydration_prm["a1"]
51         self._a2 = dehydration_prm["a2"]
52         self._a3 = dehydration_prm["a3"]
53         nu = dehydration_prm["nu"]
54         super().__init__(rho_c, nu)
55 
56     def degree(self, T, gamma_old, dt):
57         a1 = self._a1
58         a2 = self._a2
59         a3 = self._a3
60         Td = 378.15
```

```
61          f = conditional(
62              le(T, Td), 0.0, a3 * (T - Td) ** 3.0 + a2 * (T - Td) ** 2.0
                ↪  + a1 * (T - Td)
63          )
64          return f
```

A.3. Postprocessing

While FEniCS provides multiple options for writing files for further processing, such as VTK and HDF5, the examples here were one dimensional. In this case, it is convenient to export the values of interest as Numpy arrays, for example to plot them using Matplotlib. This is done by projecting the function onto the underlying mesh using `dolfin.project`. By default, this uses first order Lagrange elements, which is what we want. The resulting FEniCS function `vec` returns its DoFs by calling `vector()` on it. To avoid repetition and clutter, this is wrapped as a Python decorator `array` that can be added to any method so that it returns a Numpy array instead of a FEniCS function.

```
21  def array(form_function):
22      def get_array(self):
23          vec = dolfin.project(form_function(self))
24          return vec.vector()[:]
25
26      return get_array
```

Here, the `water_mass` method is used to illustrate the use of `@array`. The decorator `@property` is a standard Python decorator that makes methods without arguments appear as normal attribute. That means `pp.water_mass()` becomes just `pp.water_mass`.

```
241 @property
242 @array
243 def water_mass(self):
244     porestate = self.problem.indep_vars.porestate
245     porosity = self.problem.indep_vars.porosity
246     return porosity * self._saturation * porestate.water_density
```

B. Dehydration calibration

As mentioned in section 4.4.5, all models have been brought to the same form for better comparison,

$$m_{\text{dehyd}}(T) = cv\Gamma(T), \tag{B.1}$$

where c is the cement content ($\mathrm{kg\,m^{-3}}$), v is the ratio of maximally released water to cement content, and Γ is the dehydration degree ($\Gamma \in [0,1]$). A common assumption is that the dehydration below 105 °C remains zero; the constant $T_d = 378.15\,\mathrm{K}$ will be used in these cases.

Adapting the formulation of Tenchev *et al.* [TLP01] to the form in eq. (B.1) and parametrizing it, the dehydration degree reads

$$\Gamma = \begin{cases} 0 & \text{for } T \leqslant T_1, \\ r_1(T - T_1) & \text{for } T_1 < T \leqslant T_2, \\ r_2(T - T_2) + r_1(T_2 - T_1) & \text{for } T_2 < T \leqslant T_3, \\ 1 & \text{for } T > T_3. \end{cases} \tag{B.2}$$

Here, T_3 is not an independent parameter, but rather $T_3 = T_2 + \frac{1}{r_2}(1 - r_1(T_2 - T_1))$, since $\Gamma = 1$ for $T = T_3$. The parametrization of the step-wise linear function in [DK09] reads

$$\Gamma = \begin{cases} 0 & \text{for } T \leqslant T_d, \\ r(T - T_d) & \text{for } T_d < T \leqslant T_1, \\ 1 & \text{for } T > T_1. \end{cases} \tag{B.3}$$

Again, T_1 is not independent, with $T_1 = T_d + \frac{1}{r}$. As mentioned in section 4.4.5, the approach of Pont and Ehrlacher uses a differential equation [PE04]. With the substitution of the fixed value of 200 K by the parameter T_{denom}, the dehydration degree reads

$$\Gamma = \begin{cases} 0 & \text{for } T \leqslant T_d, \\ 1 - \exp\left(-\frac{T - T_d}{T_{denom}}\right) & \text{for } T > T_d. \end{cases} \tag{B.4}$$

The equations given in section 4.4.5 for the descriptions by Pesavento [Pes00] and Gawin *et al.* [GPS11a] were already fully parametrized.

All models were fitted to TGA data for the concrete used in section 5.2, and the results can be found in table B.1.

Table B.1.: Start values and resulting parameter values for different dehydration models

Tenchev *et al.* [TLP01]	Name	ν	T_1	T_2	r_1	r_2
	Start values	0.2	500.0	600.0	0.003	0.0002
	Fitted values	0.202	364.1	473.3	0.005 14	0.000 843
Gawin *et al.* [GPS11a]	Name	ν	a_1	a_2	a_3	
	Start values	—	0.0003	-8×10^{-8}	-6×10^{-11}	
	Fitted values	0.209	0.003 08	-2.37×10^{-6}	-8.38×10^{-25}	
Pesavento [Pes00]	Name	ν	k			
	Start values	0.2	−0.004			
	Fitted values	0.189	−0.0057			
Dwaikat and Kodur [DK09]	Name	ν	r			
	Start values	0.2	0.005			
	Fitted values	0.187	0.003 45			
Pont and Ehrlacher [PE04]	Name	ν	T_{denom}			
	Start values	0.2	200.0			
	Fitted values	0.199	178.02			